k-Space Image Correlation Spectroscopy (kICS): Accuracy and Precision, Capabilities and Limitations

Jeremy A. Schwartzentruber

Department of Chemistry
McGill University
Montreal, Quebec, Canada

August 2010

A Thesis submitted to McGill University
in partial fulfillment of the requirements for the degree of
Master of Science

Contents

Abstract 5

Résumé 7

Statement of Originality 9

Acknowledgements 11

List of Abbreviations 13

List of Symbols 14

1. Introduction 15
  1.1 The Cell Membrane 16
  1.2 Fundamentals of Fluorescence 18
  1.3 Fluorophores 21
    1.3.1 Organic Dyes 21
    1.3.2 Fluorescent Proteins 22
    1.3.3 Quantum Dots 24
  1.4 Fluorescence Microscopy 26
    1.4.1 Wide-field Microscopy 27
    1.4.2 Confocal Laser Scanning Microscopy (CLSM) 28
    1.4.3 Super-Resolution Microscopy Methods 29
  1.5 Measuring Protein Diffusion and Transport 31
    1.5.1 Fluorescence Correlation Spectroscopy (FCS) 32
    1.5.2 Fluorescence Recovery After Photobleaching (FRAP) 34
    1.5.3 Single Particle Tracking (SPT) 34
    1.5.4 Temporal Image Correlation Spectroscopy (TICS) 36
    1.5.5 k-Space Image Correlation Spectroscopy (kICS) 37
    1.5.6 Fourier Image Correlation Spectroscopy (FICS) 37
    1.5.7 Other Techniques and Variants 38

2. k-Space Image Correlation Spectroscopy: Theory and Data Analysis 41
  2.1 kICS Theory 42
  2.2 kICS Data Analysis for Single Population Diffusion 45

3. k-Space Image Correlation Spectroscopy: Accuracy and Precision Explored Via Simulations 51
  3.1 Computer Simulations 51
    3.1.1 Particle Diffusion and Flow 51
    3.1.2 Background and Photon Counting Noise 53
    3.1.3 Photobleaching 56

3.1.4 Default Simulation Parameters 56
3.2 Bias in kICS Measurements with Low Spatial or Temporal Sampling 57
3.3 Recovery of Fast Diffusion Dynamics via kICS 65
3.4 Accuracy and Precision of kICS Measurements 68
3.5 Nonuniform Particle Distributions 70
3.6 Estimating kICS Measurement Uncertainty 72

4. k-Space Image Correlation Spectroscopy Applied to Microspheres and Live Cells 79
4.1 Measuring Diffusing Microspheres 79
4.1.1 Microsphere Sample Preparation and Confocal Imaging 79
4.1.2 kICS Analysis 81
4.2 Measuring Diffusion in Live Cells with Quantum Dot Labels 84
4.2.1 Methods 85
4.2.2 Data Analysis 86
4.2.3 Results 92

5. Conclusion 95

6. References 97

Abstract

k-space image correlation spectroscopy (kICS) is a recently developed technique that can be used to measure the transport dynamics and number density of fluorescently labeled molecules in living cells, while being completely unbiased for transport measurements by fluorophore photobleaching or blinking. Whereas the precision of fluorescence correlation spectroscopy (FCS) and temporal image correlation spectroscopy (TICS) have been investigated in detail, no such study exists for kICS. In this thesis, we present a thorough characterization of the accuracy and precision of kICS for measurements of 2D diffusion over a range of imaging frame rates, spatial dimensions, and particle distributions. We use computer simulations as a primary tool to vary simulated imaging conditions and data analysis parameters, and thereby obtain a statistical description of kICS error.

We find that kICS measurements of diffusion are consistently biased low for image regions smaller than ~100 μm^2 and we examine two alternative methods for correcting the bias. We also report the surprising discovery that kICS can measure 2D particle diffusion that is at least ten times faster than can be measured with other methods that compute correlations between successive image frames; this is possible because kICS measures long-range correlations that persist after particles have exited the specific volume of the laser focus where they were found in a previous frame. In addition, we show that unlike FCS or TICS, kICS measurements are accurate even when analyzing highly nonuniform particle distributions, as would be found after local release or photoactivation of fluorescently-tagged biological molecules. Finally, we describe a method of estimating the uncertainty from a single kICS measurement of diffusion, which is useful when measurements cannot easily be repeated.

We use experimental fluorescence microscopy image series of diffusing microspheres to confirm that bias in kICS depends on the size of the image region analyzed, and we test the two methods of correcting the bias. We also apply kICS to measure the diffusion of membrane biomolecules tagged with blinking quantum dots in living cells, and compare the results with single particle tracking analyses of the same data.

Résumé

La spectroscopie par corrélation d'images dans l'espace vectoriel (kICS) est une nouvelle technique qui permet de mesurer la dynamique du transport moléculaire ainsi que le nombre de molécules fluorescentes à l'intérieur de cellules vivantes et de leurs membranes. Cette technique présente l'avantage de fournir des mesures de dynamique de transport non biaisées par le photo-blanchiment et le clignotement des fluorophores. Alors que la précision des techniques de spectroscopie de corrélation de fluorescence (FCS) et de spectroscopie par corrélation temporelle d'images (TICS) a déjà été étudiée en détail, aucune étude n'existe concernant la technique kICS. Dans cette thèse, je présente une caractérisation approfondie de l'exactitude et de la précision de kICS sur des mesures de diffusion 2D pour une large plage de fréquences d'acquisition d'image, de tailles d'image et de distributions spatiales du nombre de particules. J'ai principalement utilisé des simulations par ordinateur afin de pouvoir modifier les conditions d'acquisition et d'analyse d'image et ainsi d'obtenir une description statistique des erreurs de kICS.

Il ressort de mes analyses que les mesures de diffusions effectuées par kICS donnent des valeurs systématiquement trop faibles lorsque les régions imagées ont une surface de moins de ~100 μm^2, j'ai donc étudié deux méthodes alternatives afin de corriger ce biais. J'ai aussi pu constaté que kICS permet de mesurer des diffusions de particules en 2D pour des vitesses au moins dix fois supérieures à celles des diffusions mesurées par des méthodes corrélant des images successives. Ceci est rendu possible par le fait que kICS mesure des corrélations à longue distance qui persistent même lorsque la particule quitte le point focal d'illumination du laser qu'elle occupait lors de la prise de l'image précédente. En outre, je montre que, contrairement à FCS ou TICS, les mesures effectuées par kICS sont exactes y compris lorsque des régions ayant une distribution spatiale de particules fortement hétérogène sont analysées, cas rencontré notamment lors de la libération locale ou la photo-activation de molécules biologiques marquées par un fluorophore. Finalement, je décris une méthode permettant d'estimer l'incertitude de la

mesure à partir d'une seule donnée de diffusion obtenue par kICS. Ceci est particulièrement utile par exemple lorsqu'il est difficile de répéter une acquisition.

J'ai utilisé des mesures expérimentales de diffusion de microsphères pour confirmer que le biais de kICS dépend bien de la taille de la région analysée et j'ai testé l'efficacité des deux méthodes proposées pour corriger ce biais. J'ai également employé kICS afin de mesurer la diffusion dans des cellules vivantes de biomolécules membranaires marquées par point quantique et j'ai comparé ces résultats avec ceux effectués sur les mêmes images par suivi de particules isolées.

Statement of Originality

The author claims the following aspects of the thesis constitute original scholarship and an advancement of knowledge:

1. Bias in k-space image correlation spectroscopy (kICS) measurements of diffusion. The necessary use of finite Fourier transforms in kICS results in spectral leakage, a commonly known phenomenon in power spectrum estimation. This causes kICS measurements of diffusion to be biased low by an amount that depends on the size of the image relative to the point spread function. Chapter 3 is the first report that this bias exists, and Chapter 4 presents an experimental test of two methods of correcting the bias.

2. Accuracy and precision of kICS diffusion measurements. Chapter 3 describes a complete characterization of the dynamic range, accuracy and precision of kICS measurements of diffusion using computer simulations over a wide range of spatial and temporal sampling. It was found that kICS is accurate over a larger dynamic range than temporal image correlation spectroscopy (TICS), and that kICS is also more precise within this range.

3. kICS diffusion measurements with nonuniform particle distributions. It was discovered that that kICS can accurately measure diffusion in cases where the initial particle distribution is highly nonuniform, in contrast to most other known fluorescence correlation measurement techniques. Three different types of nonuniform distributions were investigated via kICS analysis of computer-simulated image series, and kICS provided accurate measurements in all cases.

4. Method to estimate the error in a single kICS diffusion measurement. Because one must select cut-offs for certain parameters when analyzing a fluorescence microscopy image series with kICS, a significant component of measurement uncertainty is associated with cut-off selection. Chapter 3 describes a method to determine this contribution to the measurement uncertainty in a single kICS analysis.

Acknowledgements

Throughout my work towards this thesis I have received guidance and support from many people, whom I would like to thank here.

First, I would like to thank my supervisor, Dr. Paul Wiseman. He allowed me the freedom to explore many paths, and provided encouragement and support both when these efforts succeeded and when they failed. He supported me to attend two Biophysical Society conferences, a workshop on fluorescence, and the Neurophysics retreat, which greatly enhanced my exposure to good science.

I would like to thank Dr. Jody McGuire, who was the best mentor one could wish for in learning cell culture and microscopy. Jody was generous with her time, clear-headed and knowledgeable, and was always fun to work with. The Wiseman lab was filled with entertaining and helpful people. I would especially like to thank Elvis Pandzic for his patient and thoughtful help in digesting the math behind kICS. Dr. Asmahan Abu-Arish generously helped me with cell culture and microscopy. I appreciated discussions, coffee, and parties with all the group members, including Antoine Godin, Mikhail Sergeev, Tim Toplak, Dr. Benjamin Rappaz, Dominique Guillet, Jean-François Desjardins, Umakanta Tripathy, and Laurent Potvin. David Kolin kindly provided advice on my project despite having already left the lab for medical school.

Dr. Eva Arnspang-Christensen was a wonderful collaborator during her exchange from Denmark and her optimistic attitude made the winter months in the lab enjoyable. She generously provided the microscopy and single particle tracking data, described in Sec. 4.2, for living cells tagged with quantum dots.

I thank Dr. David Ronis for his insightful discussions whenever I had questions about kICS. I am grateful to Drs. Gonzalo Cosa and Anthony Mittermaier for their excellent teaching and enthusiasm for science, and for the occasional use of their lab space.

Finally, I am deeply grateful to my partner, Neeltje Boogert. She is a person of constant love, encouragement, and enthusiasm. She has always believed in me, and is always willing to edit anything I need help with. Neeltje, words cannot describe what a unique and wonderful person you are.

List of Abbreviations

ACP	acyl carrier protein
BA	beam area
BLAP	biotin ligase acceptor peptide
CCD	charge-coupled device
ChTox	cholera toxin
CLSM	confocal laser scanning microscope
CoA	coenzyme A
EGFP	enhanced green fluorescent protein
EGFR	epidermal growth factor receptor
EMCCD	electron multiplying charge coupled device
FCS	fluorescence correlation spectroscopy
FICS	Fourier image correlation spectroscopy
FRAP	fluorescence recovery after photobleaching
FRET	fluorescence resonance energy transfer
GFP	green fluorescent protein
GPI	glucosylphosphatidylinositol
ICS	image correlation spectroscopy
ITIR-FCS	imaging total internal reflection fluorescence correlation spectroscopy
kICS	k-space image correlation spectroscopy
MEF	mouse embryonic fibroblast
MSD	mean-squared displacement
NA	numerical aperture
PBS	phosphate buffered saline
pCF	pair correlation function
PMT	photomultiplier tube
PSF	point spread function
QD	quantum dot
RICS	raster image correlation spectroscopy
S/B	signal-to-background ratio
SPT	single particle tracking
STED	stimulated emission depletion
STICS	spatiotemporal image correlation spectroscopy
TICS	temporal image correlation spectroscopy
TIRF	total internal reflection fluorescence
WF	width factor for counting noise
YFP	yellow fluorescent protein
RT	room temperature

List of Symbols

$\langle\ \rangle$	ensemble average
$\mathbf{A}$	image matrix without noise
$\mathbf{C}$	image matrix with noise
D	diffusion coefficient
F	imaging frame time
g	autocorrelation function
h	Planck's constant
i	observed intensity; also $\sqrt{-1}$
$I(\mathbf{r})$	3D microscope PSF
$\mathbf{k}$	vector in Fourier space
$\mathrm{k}_x,\mathrm{k}_y$	k-space vector x or y component
N	number of particles in image
q	fluorescence quantum yield
r	correlation function
$\mathbf{r}$	vector in real space
S_0	singlet ground electronic state of a molecule
S_1, S_2	1st and 2nd excited singlet states
T_1	1st excited triplet state of a molecule
t	time variable
$\mathbf{U}$	noise matrix
$\mathbf{v}$	velocity
$w(x,y)$	window function

Å	angstrom (10^{-10} m)
α	photobleaching rate constant
δ	fluctuation
Δt	time between images in a series
λ	wavelength
ν	frequency
π	3.141592...
ρ	microscopic particle number density
σ	standard deviation
τ	time lag variable
τ_D	characteristic diffusion time
$\Theta(t)$	fluorescence emission function
ω_0	e^{-2} laser beam radius in xy plane

1. Introduction

In the quest to understand the complex inner workings of living cells, tools are needed that can probe many aspects of cell function, at different spatial and time scales. Optical microscopy has long been one of the main tools for this purpose because living cells, in cell culture and even in intact animals, can be resolved and observed for extended time periods without apparent damage to the cells. In the past decade in particular, fluorescence imaging and spectroscopy techniques have become ubiquitous tools in cell biology and biophysics, owing to improvements in microscope technology, the development of genetically encoded fluorophores, and detectors that are sensitive enough for imaging single molecules. Despite these advances, optical microscopy in the far field (i.e. more than a few nm from the sample) is limited in resolution by the diffraction of light and cannot resolve objects separated by less than ~200 nm in living cells. Thus, it is challenging to obtain information on the dynamic processes of biomolecules and molecular complexes, which are generally smaller than 10 nm.

This thesis explores the capabilities and limits of a fluorescence fluctuation spectroscopy method called k-space image correlation spectroscopy (kICS), which has significant practical advantages for measuring the diffusion or flow of fluorescently labelled macromolecules in cell membranes. We characterize the accuracy of kICS over a range of imaging conditions, and describe two ways of correcting for a bias that occurs when analyzing small image subregions. We then show novel applications of kICS, including measuring relatively fast diffusion in planar membranes and accurately measuring diffusion despite highly nonuniform initial particle distributions.

In this chapter we provide an introduction to topics needed to understand kICS and the context in which it is applied. We begin with an overview of eukaryotic cell membranes, and the diffusion or directed motion of membrane components that are essential to membrane function. We next describe the phenomenon of fluorescence, the types of fluorophores used in research on living cells, and some common fluorescence microscopy imaging modalities. Finally, we review a variety of image analysis techniques that can access information on molecular diffusion, directed motion, aggregation, immobility, and number density (i.e. concentration) of labelled biomolecules.

1.1 The Cell Membrane

From single-celled bacteria to multi-cellular plants and animals, cells are the fundamental units of all living organisms. Animal cells are separated from the outside environment and from other cells in the organism by a phospholipid bilayer, called the plasma membrane, which acts as a barrier to passage of polar molecules and defines the cell's volume. Inside the cell, a variety of organelles (with their own membranes) carry out the functions necessary for life. The plasma membrane is directly involved in many cellular processes such as cell adhesion and motility, uptake of nutrients and excretion of waste, and cell signalling. These functions are generally carried out by proteins that are embedded in the membrane. The importance of membranes to life is reflected in the human genome, where 20 to 30% of coded information corresponds to membrane proteins [1-2].

In the model of membrane structure proposed by Singer and Nicolson in 1972, membrane proteins are randomly distributed in a homogeneous, viscous fluid that is the lipid bilayer [3]. Since then our understanding of membrane structure and dynamics has changed considerably. Rather than being homogeneous, the numerous types of lipids found in the membrane are laterally organized into domains with different composition. Liquid ordered domains, sometimes called lipid rafts, are enriched in cholesterol and sphingolipids, and coexist with more fluid domains composed primarily of phospholipids with unsaturated hydrocarbon tails [4-5]. Specific proteins partition preferentially into rafts, creating functional domains with roles in membrane signalling and trafficking. Proteins, which may span the entire membrane or may be attached to the membrane by lipid anchors or hydrophobic peptide segments, comprise a significant fraction of the membrane area. A number of studies have found total protein densities in cell membranes of around 30,000 per μm^2 [6]. Membrane-embedded proteins may also have large domains that extend outside the membrane region, and can have interactions with other macromolecules inside the cell that organize them into functional complexes [7]. Fig. 1.2 shows a cartoon depiction of a biological membrane with embedded proteins.

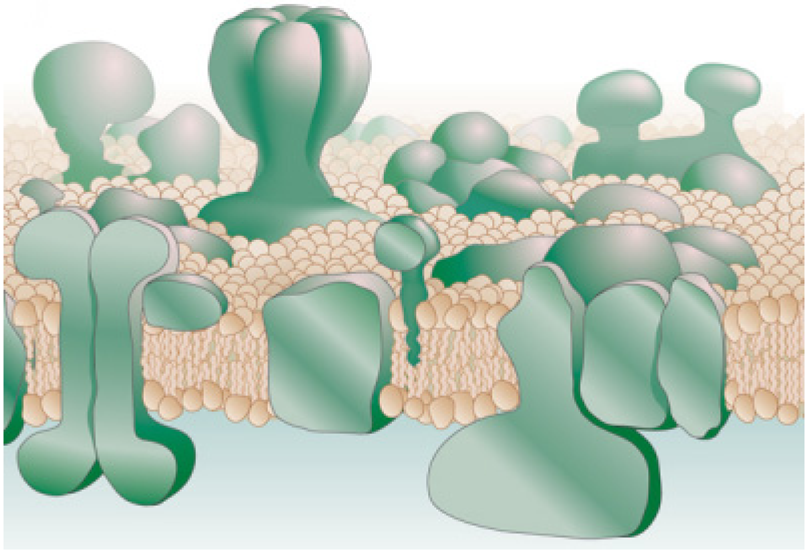

FIGURE 1.2: A modern view of the cell membrane: the membrane is dense with proteins of different types, some of which extend out of the membrane or change the local membrane thickness. Lipids segregate into dynamically changing domains, and some proteins partition preferentially into one type of lipid domain. The lipid bilayer is ~5 nm in thickness. Reprinted by permission from Macmillan Publishers Ltd: Nature, Ref. [7], copyright 2005.

Membranes and other cellular components are not static, as they might appear in drawings, but are in constant motion. Membrane proteins may undergo diffusion, directed transport, or be transiently immobilized, all of which can be important for biological function [8]. Indeed, diffusion is the norm for any molecule that is not either being actively transported or immobilized by attachment to a larger structure. Thus, measurement of lipid and membrane protein diffusion has been one of the means used to investigate membrane heterogeneities [9-10], and to detect molecular interactions that slow a protein's diffusion or immobilize it [11].

Diffusion measurements are commonly done by attaching fluorescent probes to specific membrane proteins or lipids so that they can be imaged with high sensitivity via fluorescence microscopy. In the following sections we introduce the use of fluorescence, as well as optical microscopy and analysis techniques that are used to measure diffusion or transport of molecules in membranes.

1.2 Fundamentals of Fluorescence

Luminescence is the emission of light that occurs when a molecule transitions from an excited electronic state to its ground state. Luminescence is termed either fluorescence or phosphorescence, depending on the nature of the excited state prior to emission. Fluorescence occurs when a molecule transitions from an excited singlet electronic state to the singlet ground state ($S_1 \rightarrow S_0$). When the transition is from an excited triplet electronic state to the singlet ground state ($T_1 \rightarrow S_0$), a quantum mechanically "forbidden" transition, the resulting photon emission is called phosphorescence. Because the transition is forbidden, phosphorescence occurs at much lower rates than fluorescence, and is thus not useful in imaging.

The processes involved in molecular excitation and fluorescence emission can be summarized in a simplified Jablonski diagram (Fig. 1.3). The ground, first, and second singlet electronic states are referred to as S_0, S_1, and S_2 respectively, and vibrational states are labeled 0, 1, and 2, though higher states also exist. A molecule begins in the singlet ground electronic state (S_0) and the lowest vibrational state because at physiological temperatures there is not enough thermal energy for excited states to be significantly populated. The molecule absorbs a photon of light ($h\nu_A$), which promotes an electron to an excited singlet electronic state (S_1, S_2, …) and generally to a vibrationally excited state as well. Absorption of the photon occurs almost instantaneously (~10^{-15} s), after which the molecule relaxes to the lowest vibrational level of S_1. This vibrational relaxation is called internal conversion, and occurs within about 10^{-12} s. Fluorescence emission occurs after a time that typically ranges from 10^{-9} to 10^{-8} s, which is called the fluorescence lifetime. The energy of the fluorescence photon emitted ($h\nu_F$) is thus the energy difference between the lowest vibrational state of S_1 and one of the vibrational states of S_0 which the molecule enters upon fluorescence emission (this could be an excited vibrational state).

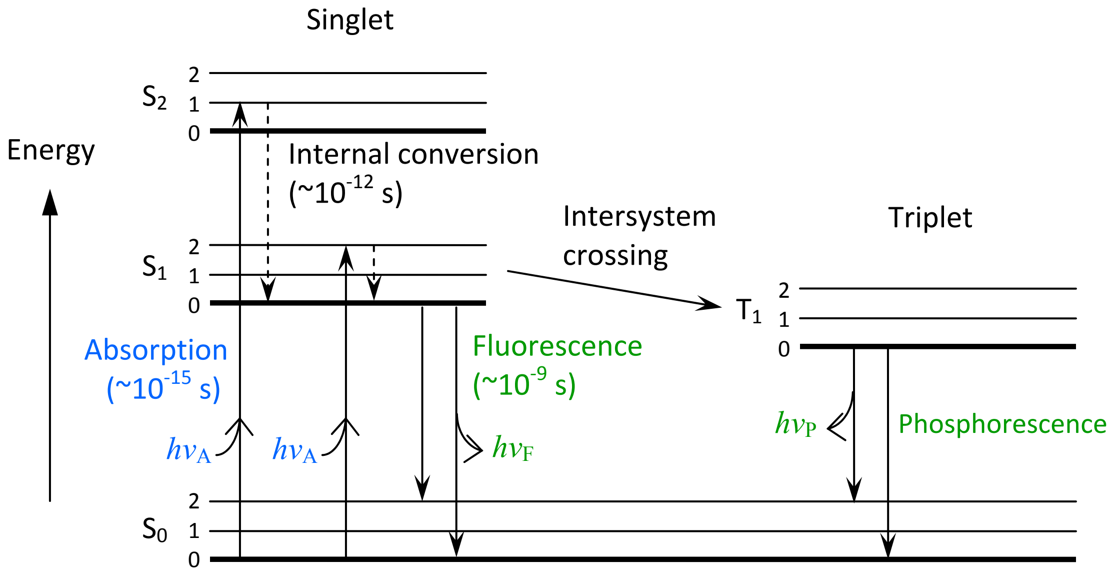

FIGURE 1.3: A Jablonski diagram, showing the processes that lead to fluorescence and phosphorescence.

Note that the energy of the fluorescence photon emitted, represented by the length of the vertical arrow, is less than the energy of the absorbed photon. This is true of all fluorescent molecules, and results in the emission spectrum being shifted to longer wavelengths than the absorption spectrum, as in Fig 1.4. This red shift in fluorescence emission wavelength, called the Stokes shift, occurs because non-radiative decay processes such as internal conversion and solvent relaxation release some of the energy initially absorbed. The Stokes shift is one of the factors that enables the tremendous sensitivity of fluorescence detection, since filters can be used to block wavelengths of the exciting light while passing the emitted fluorescent light of longer wavelength.

When a molecule is in the excited state, pathways other than fluorescence can also occur. Most prevalent is internal conversion from S_1 to S_0, whereby the excited state energy is released as heat. A molecule in the S_1 state can also undergo spin conversion to the first triplet state, T_1, a process called intersystem crossing. The lifetime of the excited triplet state typically ranges from 10^{-3} to 1 s, and emission from this state is called phosphorescence. Importantly, molecules in excited states are much more prone to chemical reactions, particularly redox reactions such as oxidation by molecular oxygen. Due to its longer lifetime, T_1 is considered to be the most photochemically active state. In

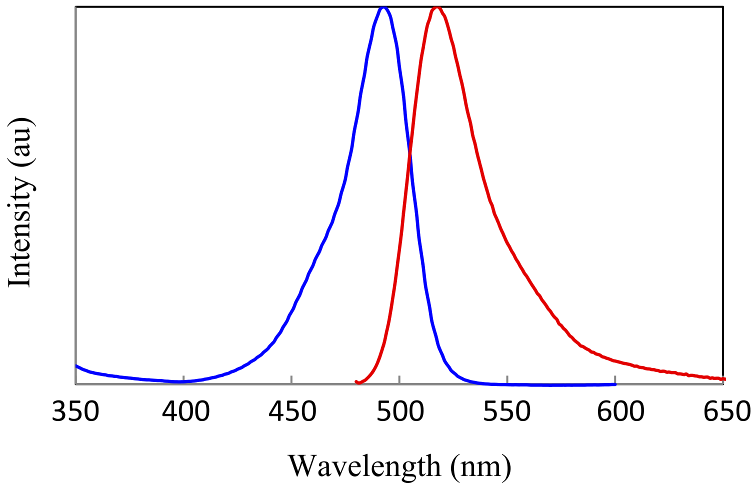

FIGURE 1.4: Normalized absorption (blue) and fluorescence emission (red) spectra of AlexaFluor 488 hydrazide in water. Figure created using raw data on product spectra available from www.invitrogen.com.

the case of excited fluorescent molecules, chemical reaction usually renders them nonfluorescent. This is called photobleaching, and will be revisited later in this thesis as it is a problem frequently encountered in fluorescence microscopy. Certain reagents can be used to minimize photobleaching, such as an enzymatic oxygen-scavenging system [12] or a reducing and oxidizing system [13], but these are often not compatible with living cells. Thus, the intrinsic brightness and photostability of the fluorophore used is important for live cell imaging.

Some additional mechanisms not shown in Fig. 1.3, such as energy transfer and quenching, can also lead to de-excitation of the molecule without emission of a photon. Because of these non-radiative decay processes, the number of fluorescence photons emitted is lower than the number of photons absorbed. The quantum yield, q, of a fluorophore is the ratio of the number of photons emitted to the number of photons absorbed, and is an important parameter that characterizes the brightness of a fluorescent molecule.

1.3 Fluorophores

1.3.1 Organic Dyes

In 1845 Sir John Herschel observed that a solution of quinine, although appearing transparent and colourless under most conditions, would exhibit a “beautiful celestial blue colour” under certain incidences of sunlight [14]. Indeed, modern tonic water glows blue under an ultraviolet lamp (black light) because of the fluorescence of quinine; despite its bitter taste, the practice of adding quinine to tonic water began because it also has antimalarial properties. Like most organic fluorescent dyes discovered since then, quinine is a small molecule with conjugated aromatic rings. The small size of organic dyes means that when they are used to label a desired molecule, they are less likely than larger probes to perturb the labelled molecule’s natural function. When monitoring active transport the size of the label may not be very important, but for diffusing molecules a large tag is likely to alter the diffusion by changing the effective Stokes-Einstein radius of the complex [15].

Organic dyes are available in a wide variety of colours, which makes it possible to select a dye that is most suitable based on the laser wavelengths and emission filters available in the lab. They have also been industrially optimized for increased brightness, improved photostability, and reduced self-quenching, and modern dyes are greatly improved over those used in the past. Because of this long history of optimization, it is believed that further improvements in organic dye properties are likely to be small [15]. Yet, as researchers push the limits of spatial and temporal resolution in cellular imaging, it is still a challenge to obtain a sufficiently bright and photostable fluorescence signal from small numbers of labelled molecules. Thus, to maximize the fluorescence signal a high excitation intensity is often used, which results in photobleaching a significant fraction of the dye over a series of images. At best, photobleaching simply causes a reduction in signal over time; at worst, certain methods of analyzing a fluorescent signal will return incorrect measurements, and the by-products of photobleaching are often toxic to cells.

The most common method of labelling samples with organic dyes is immunofluorescent staining, in which fluorophore-decorated antibodies (Fig. 1.5 (A)) are used that bind specifically to the target molecules. This can produce brilliant still images, as in Fig. 1.5 (B), but it is not often applied to live cells; cells are normally chemically fixed, as the pair of antigen binding sites on each antibody would induce protein cross-linking. Newer and more advanced techniques exist for attaching organic dyes to proteins in living cells, but for many applications organic dyes have been superseded by genetically encoded fluorescent proteins.

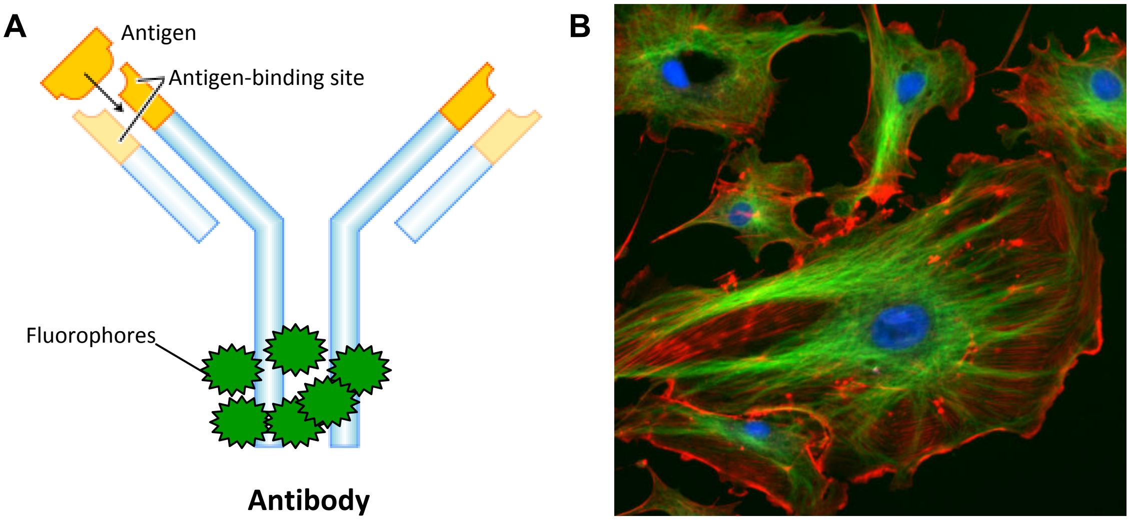

FIGURE 1.5: (A) General structure of a fluorescently-labelled antibody, with two binding sites that can bind to antigens. (B) Immunofluorescence image of endothelial cells. Microtubules are labelled by an antibody tagged with a green fluorophore; actin filaments are labelled red using phalloidin and nuclei are stained blue with DAPI. Images for (A) and (B) are in the public domain and were copied from the Wikipedia article on antibodies.

1.3.2 Fluorescent Proteins

Background fluorescence and imperfect specificity of labelling are common problems with chemical labelling strategies such as immunofluorescent staining. Ideally, every copy of the target protein in a cell would be fluorescently labelled with a probe of the same brightness. Fluorescent proteins can be used to achieve this level of control. Although many proteins in cells have a natural weak fluorescence due to the amino acid tryptophan, this is not useful for observing specific proteins in cells, and thus it mainly contributes to an undesired background autofluorescence. The key advance came with the discovery of the green fluorescent protein (GFP), isolated from the jellyfish *Aequoria victoria*. The fluorophore in GFP is formed from an autocatalytic cyclization reaction of three amino acid residues, which are located at the center of the 11-stranded β-barrel structure of the protein (Fig. 1.6) [16]. Thus, when GFP is synthesized inside a cell, it is not immediately fluorescent, but becomes fluorescent after maturing into the correct folded structure and forming the chromophore. The DNA sequence for GFP can be fused with the DNA sequence of another protein at either the C- or N-terminus, and then transfected into cells. Because the two will be translated as a single unit in the cell, every copy of the target protein will be labelled with a covalently-attached fluorescent GFP.

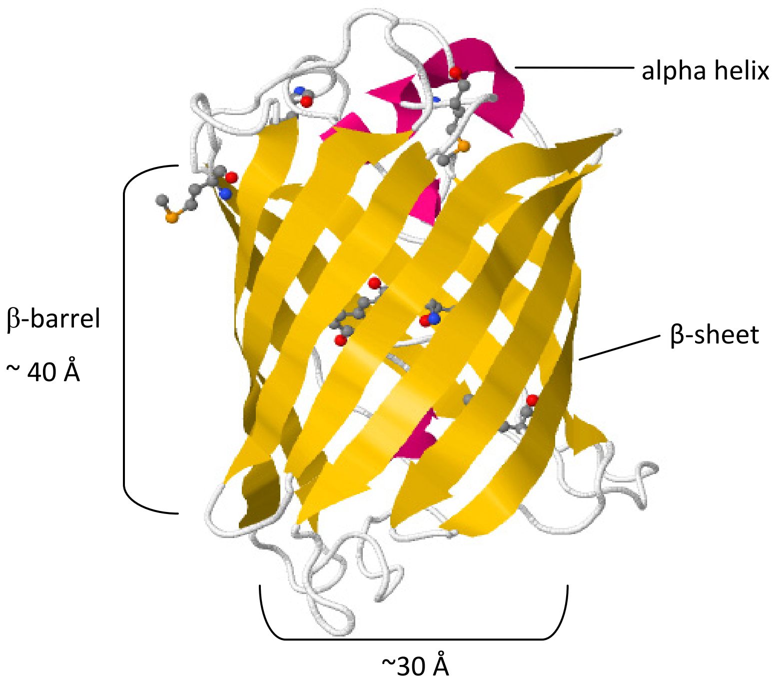

FIGURE 1.6: X-ray crystal structure of the green fluorescent protein shown in ribbon representation. Figure created from protein data bank structure 1EMA [16] using Jmol.

A number of research groups have found mutations in the amino acid sequence of GFP to create improved versions. Dr. Roger Tsien shared the 2008 Nobel Prize in chemistry for his work that led to an enhanced GFP (EGFP) with improved brightness and more rapid folding [17]. Other mutations have created fluorescent proteins with emission peaks that range from blue to yellow [16, 18], and the discovery and optimization of fluorescent proteins from coral has filled the gap at the red end of the visible spectrum [19]. The photostability and brightness of GFP are comparable to that of many organic dyes, although some of the variants with different colours exhibit reduced brightness or photostability [20]. A drawback of fluorescent proteins is their moderately large size (27 kDa, about 3 x 4 nm) in comparison with organic dyes, which is larger than some cellular proteins that could be tagged. Compared with newer fluorescent "quantum dot" probes, fluorescent proteins have fairly broad emission spectra, which can cause bleed-through between detection channels and complicate multicolour experiments where two or more proteins are fluorescently labelled. Additionally, when cells are transfected with a GFP-target protein fusion construct, the level of expression will vary between cells, and the protein concentration may not reflect endogenous levels. Overexpression has been shown to alter dynamics of cell surface receptors [21], and presumably has effects when other protein types are labelled as well.

In the past few years a new class of fluorescent proteins has been developed whose emission can be switched "off" and "on" in response to light [22]. This switching capability has enabled new experiments and types of microscopy. Because a subset of labelled proteins can be activated at one time, the diffraction patterns from individual fluorescent molecules can be resolved sequentially despite a high overall density. Thus, by fitting the centroids of the imaged fluorescence diffraction spots from single molecules, one can obtain "super-resolution" microscopy images with three-dimensional position resolution (10 – 50 nm) far better than standard diffraction-limited optics [23]. Due to the necessity of sequentially activating and deactivating subsets of labelled molecules, these techniques have poorer time resolution than conventional microscopy, and thus are currently less useful for measuring dynamics of molecular diffusion and transport.

1.3.3 Quantum Dots

Quantum dots (QDs) are single semiconductor nanocrystals a few nanometres (2 – 5 nm) in diameter whose absorption and fluorescence emission wavelengths depend on their size. QDs have become widely used labels for single-biomolecule detection because of a number of advantages they have over organic dyes and fluorescent proteins. Foremost is their fluorescence brightness, which is up to an order of magnitude greater than most organic fluorophores. This results from high extinction coefficients (100,000 to 1,000,000 $M^{-1}cm^{-1}$), and similar quantum yields and emission saturation levels [24]. QDs are also nearly 100 times more photostable than conventional fluorescent probes, and single particles have been observed and tracked for hours without permanent photobleaching [24-25]. However, QDs also intermittently enter non-emissive states, and this “blinking” fluorescence can make single particle tracking difficult, and can also complicate correlation spectroscopy methods which measure fluorescence fluctuations [26]. By tuning core size and composition, QDs with emission wavelengths ranging from 400 nm to 2 μm are available. Other spectral properties also make QDs especially suitable for multicolour imaging. Their broad excitation spectra, which increase towards the UV, enable different colours of QDs to be excited with a single laser source. QDs also have very narrow emission spectra (full width at half maximum about one third that of conventional fluorophores [25]), which enables efficient separation of colour channels with minimal bleed-through. A new synthesis method has been found that completely eliminates QD blinking, but these modified QDs also have multiple emission wavelengths, which prevents their use in multicolour labelling [27].

Like organic dyes, to be used as labels QDs must first be attached to the desired target. Thus, layers are added to the QD core first for solubilisation and then for bioconjugation, yielding a structure like that shown in Fig. 1.7. When bioconjugation is done *in vitro*, target proteins can be conjugated directly to a simple organic solubilisation/adaptor layer exposing carboxylic acid groups. For *in vivo* conjugation, larger adaptor molecules such as streptavidin are more often conjugated to the QD first, so that it can be more easily attached to a target protein displaying the complementary group. The final size of the QD including its shell and surface biomolecules tends to be 10 to 20 nm [24]. Thus, even more so than with fluorescent proteins, one must keep in mind that QDs may affect the diffusion and interactions of labelled molecules due to their size and possible steric effects. The size of QDs also poses difficulties in introducing them inside cells. QDs are therefore most often used to label cell surface proteins [28]. Finally, when QDs are surface functionalized with multiple biomolecules, it is possible for QDs to induce clustering by conjugating to multiple targets simultaneously [29].

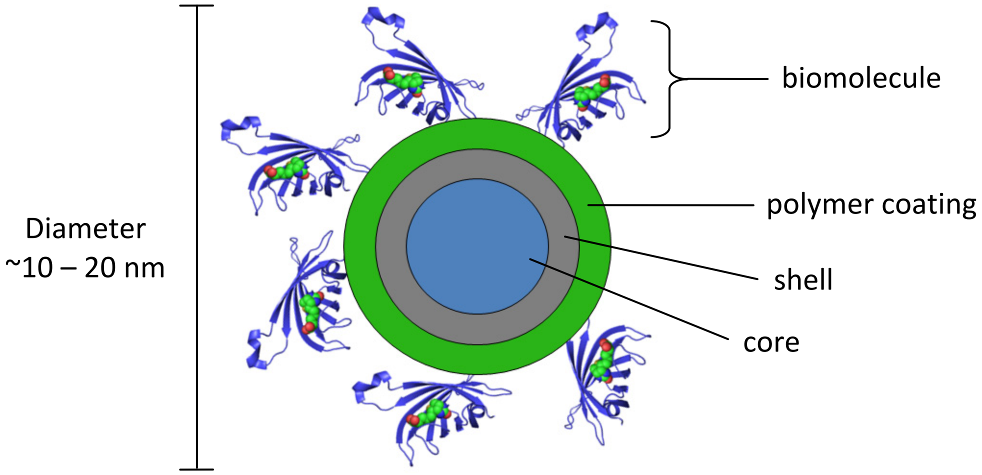

FIGURE 1.7: Diagram of a typical QD nanocrystal structure. The core, typically made of CdSe and 2 – 5 nm in diameter, is surrounded by a thin shell of ZnS which improves quantum yield and photostability. A polymer coating is added to solubilise the QD and provide a surface for conjugating biomolecules. Target biomolecules for labelling may be coupled in vitro, or functionalized for easy conjugation in vivo such as by attaching monomeric streptavidin.

1.4 Fluorescence Microscopy

Fluorescence microscopes are now common in cell biology laboratories, but come in a variety of configurations that have different benefits and costs. Fundamental to all far-field optical microscopy techniques is the point spread function (PSF), which maps the 3D spread of photons collected by a microscope objective lens from a point object. At high magnification, light from the point object is diffracted by the lens aperture and the image appears as a blurred ellipsoid. The shape of a diffraction-limited PSF is often modeled as a Gaussian function in three dimensions, with its radius in the vertical axis (z-axis) being two to three times its radius in the image plane. The size of the PSF is dependent on both the wavelength of emission (λ_{em}) and the numerical aperture (NA) of the objective lens. Using the Rayleigh spatial resolution criterion, the distance at which two objects must be spaced to be separately resolved is approximately:

$$r = \frac{0.61\lambda_{em}}{\mathrm{NA}}$$

Thus, for the fluorescence emission of EGFP ($\lambda_{em} \sim 525$ nm) collected with an objective of NA 1.4, two fluorescent particles must be separated by about 230 nm to be resolved.

This resolution limit is approximate, but in practice resolution is often slightly worse than this due to factors such as optical aberrations, imperfect beam alignment, and detector noise.

1.4.1 Wide-field Microscopy

Wide-field fluorescence microscopy is a simple and widely used technique for observing fluorescent samples [30]. Light from a laser or a mercury lamp is focused onto the sample through an objective lens so that the desired field of view is uniformly illuminated (see Fig. 1.8). Fluorescence is emitted by the sample in all directions; a fraction of the fluorescence emission is collected through the same objective, and due to its longer wavelength (a result of the Stokes shift) is separated from the exciting light by a dichroic mirror. Additional emission filters can select specific wavelength ranges for detection and also remove residual excitation light that was not reflected by the dichroic mirror. The fluorescence can either be directly viewed through an eyepiece or can be recorded as an image by a detector such as a charge-coupled device (CCD) camera. The entire field of view is recorded on a CCD camera simultaneously, and thus the speed at which successive image frames can be recorded is limited mainly by the speed of the camera.

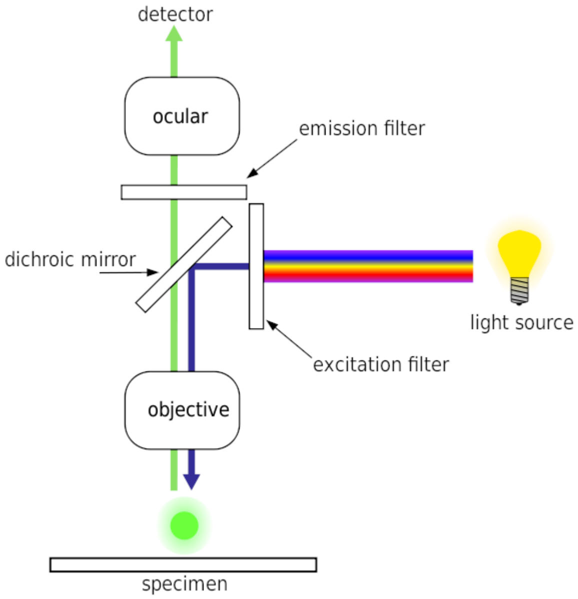

FIGURE 1.8: Schematic of a fluorescence microscope; see text for description. Image reproduced from the Wikipedia article on epifluorescence microscopy under the Creative Commons Attribution-Share Alike license.

In any wide-field microscopy setup, out-of-focus light from above and below the focal plane is collected by the microscope, and leads to blurring of the image. To a certain extent the image can be improved by deconvolution algorithms that attempt to “restore” out-of-focus blur to its in-focus position [30]. While useful for sharpening images, the success of deconvolution is dependent on the signal to noise ratio in the original image. When one desires to image a single plane of a specimen, confocal microscopy generally provides superior resolution, though the imaging frame rate is slower. Wide field fluorescence microscopy is thus especially useful in cases where the fluorescence of the sample is two dimensional itself. This technique was used with the quantum dot labelling of cell membranes described in Sec. 4.2 of this thesis.

1.4.2 Confocal Laser Scanning Microscopy (CLSM)

In confocal laser scanning microscopy (CLSM), rather than illuminating the entire field of view of the sample, the laser illumination source is focused to a diffraction-limited spot on the sample. This laser spot is scanned rapidly across the sample, sequentially exciting fluorescence at each position and ultimately recording fluorescence intensity in discrete pixels in an image. Because light from a single spot is collected at one time, photomultiplier tubes (PMTs) are commonly used to detect fluorescence, but more sensitive and expensive avalanche photodiodes (APDs) can also be used. The key improvement in confocal microscopy is the placement of a pinhole in the confocal image plane, which rejects light coming from planes above and below the focal plane of interest (see Fig. 1.9). This both improves the contrast of the focal plane, and makes it possible to image multiple thin slices of a 3D biological specimen with axial resolution of ~1 μm (this is called optical sectioning).

Though confocal microscopy is frequently used to image 3D samples, it can also be used to study cell membranes by placing the axial focus position in the plane of the membrane. In Sec. 4.1 we use a confocal microscope to image microspheres diffusing in solution.

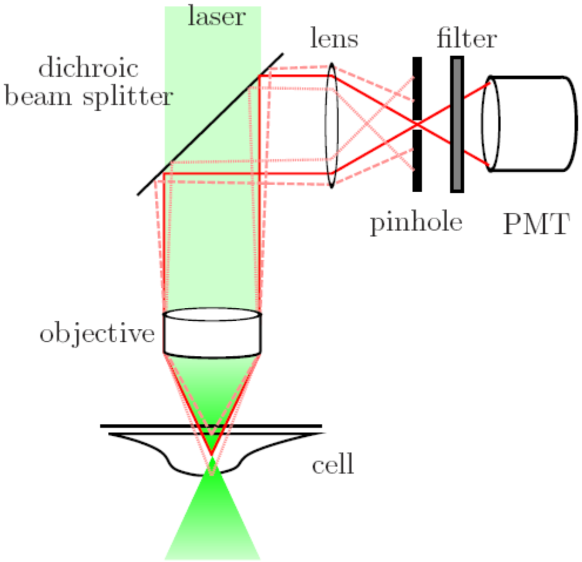

FIGURE 1.9: Schematic showing rejection of out-of-focus light by the pinhole in a confocal microscope. Light from the focal plane (solid red line) is focused through the pinhole and is collected; light from planes above and below this plane (pink line and dashed line) is not focused through the pinhole, so is not recorded by the PMT. Adapted with kind permission from Ref. [31].

1.4.3 Super-Resolution Microscopy Methods

In the past decade, a number of innovative techniques have been devised that “break the diffraction limit”, enabling resolution of structures in cells that could not be resolved with standard optical microscopy methods. Techniques such as stimulated emission depletion (STED) microscopy sharpen the PSF by suppressing fluorescence emission from fluorophores located off the center of the excitation [32]. This suppression is achieved by stimulated emission: when an excited state molecule encounters a photon with the same energy as the difference between the excited and ground electronic states, it may be stimulated to emit a second photon of the same direction and energy, thereby going back to the ground state before spontaneous fluorescence emission occurs. Thus, a second laser of the appropriate (longer) wavelength is adjusted to have near-zero intensity at the center of the focus but nonzero intensity at the periphery (Fig. 1.10). The nonlinear dependence of stimulated emission on the depletion beam means that essentially all fluorophores are depleted except for a very narrow PSF at the focus. STED has been used to investigate the structure of lipid raft nanodomains [10], which are smaller than the resolution limit of standard optical microscopy.

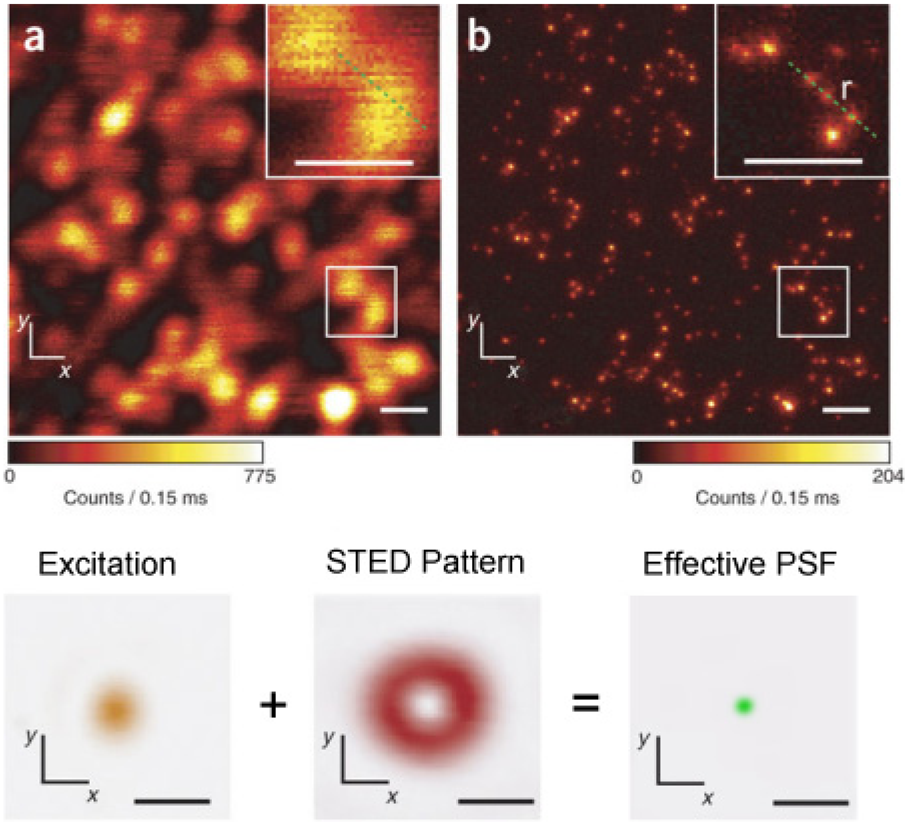

FIGURE 1.10: Example images acquired with (a) confocal and (b) STED microscopy. (*Bottom row*) How STED microscopy works: fluorophores are excited by one laser beam (yellow), but a second laser (red 'STED pattern') is tuned to a wavelength to cause stimulated emission of the excited fluorophores. The effective PSF of the excitation laser is greatly reduced in size. Adapted by permission from Macmillan Publishers Ltd: Nature Methods, Ref. [33], copyright 2007.

Super-resolution imaging can also be achieved whenever individual molecules can be distinguished, because one can fit the pattern of photons collected (the PSF) to more precisely determine the center of fluorescence emission for the molecule. This depends on having a high signal-to-noise ratio and on molecules being spaced far enough apart to be separately resolved. New techniques such as photoactivated localization microscopy (PALM) [34] and stochastic optical reconstruction microscopy (STORM) [35] can be done with dense samples, and have achieved an order of magnitude improvement in resolution in all three dimensions over conventional light microscopy. PALM has been used to observe single molecule trajectories at high densities in living cells [36].

As super-resolution techniques develop they will impact the use of fluorescence correlation methods discussed in the next section, because they change the time and spatial scales accessible. For example, STED can be used to improve the lateral resolution (reduce the focal volume) of FCS down to a beam radius of 30 nm [10], but PALM could only be applied in an imaging context. We discuss in later sections how super-resolution microscopy will affect kICS.

1.5 Measuring Protein Diffusion and Transport

At a general level of analysis, directed transport within cells is a simple process. Cargo, whether individual proteins or vesicles, is attached to a motor protein and transported with a specific average velocity along a microtubule or actin filament of the cell's cytoskeleton. Nowhere is this more essential than in neurons, where cargo from the cell body must be transported the length of the axon, a distance that can reach up to a metre in humans [37]. Directed transport always requires energy input, usually via ATP hydrolysis to drive motor proteins.

At length scales ranging from nanometres to micrometres, diffusion can be a more efficient means of transporting molecules because no external energy input is required. In any fluid at a temperature above absolute zero, the thermal motion of individual molecules or particles appears as a random walk due to collisions with other molecules. A random walk is a path characterized by a certain step size (which could be a fixed or a variable length), a time between steps, and a random direction taken at each step. An example is shown in Fig. 1.11. The mean expected displacement that a particle has traveled in two dimensions after a time t is $\sqrt{4Dt}$, where D is the diffusion coefficient. D is dependent on the step size and time between steps, and it represents the overall rate of diffusion. It is straightforward to simulate particle diffusion on a computer as a random walk, as will be described in Chapter 3.

A wide variety of methods exist for measuring the diffusion or directed transport of proteins and lipids in cells and cell membranes, with differing advantages and applications. Fluorescence correlation spectroscopy (FCS) is a well-established technique for measuring diffusion, flow, and binding dynamics, and forms the basis for more recently developed image correlation spectroscopy (ICS) methods, including the main technique investigated in this thesis, k-space ICS. We briefly introduce these techniques, as well as the complementary techniques of single particle tracking (SPT) and fluorescence recovery after photobleaching (FRAP), which can be used to measure the same underlying processes.

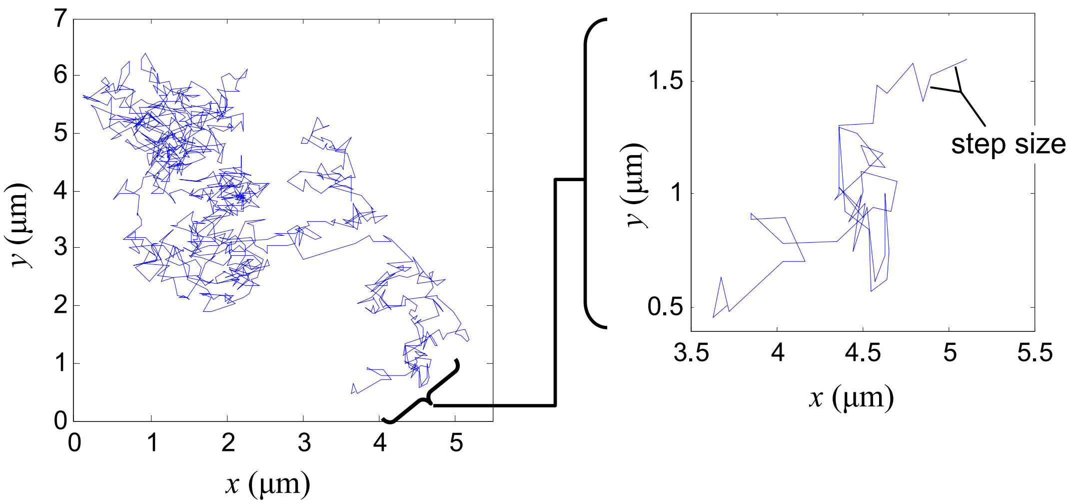

FIGURE 1.11: A random walk in two dimensions. The inset shows a magnified segment of the start of the track. Note that in a random walk, transport may appear directed for a short time, but over long times the path often crosses back over itself.

1.5.1 Fluorescence Correlation Spectroscopy (FCS)

FCS is a fluorescence fluctuation technique that was introduced in the 1970's to measure the speed and mode of molecular transport, and the binding kinetics of small molecules to macromolecules, with minimal perturbation of the system studied [38-39]. Molecules in solution and in cell membranes are in constant motion. When a laser beam is focused to a small open subvolume (femtolitres) in a solution, any process that changes the number or brightness of fluorophores in the detection volume, such as diffusion or transport of molecules, or photochemical/photophysical changes, will cause fluctuations in the recorded fluorescence intensity (see Fig. 1.12). In FCS, the fluorescence intensity is sampled rapidly enough (microseconds) so that the fluctuations reflect the average residency time of fluorescent molecules within the focal volume. A time series of the fluctuations is recorded, and a time autocorrelation function calculated from the data and fit with appropriate decay models based on the molecular dynamics giving rise to the fluctuations. It has thus been possible to measure translational diffusion, chemical reactions, conformational changes, and fluorophore concentrations. A drawback of traditional FCS is that results depend heavily on the size and shape of the focal volume, which must be carefully calibrated before each measurement using a fluorophore solution of known diffusion coefficient. Newer variants of FCS, such as two-focus FCS [40] and z-scan FCS [41] can be used without the need for calibration. FCS is also limited in that the measurement is made from only one spot within the sample.

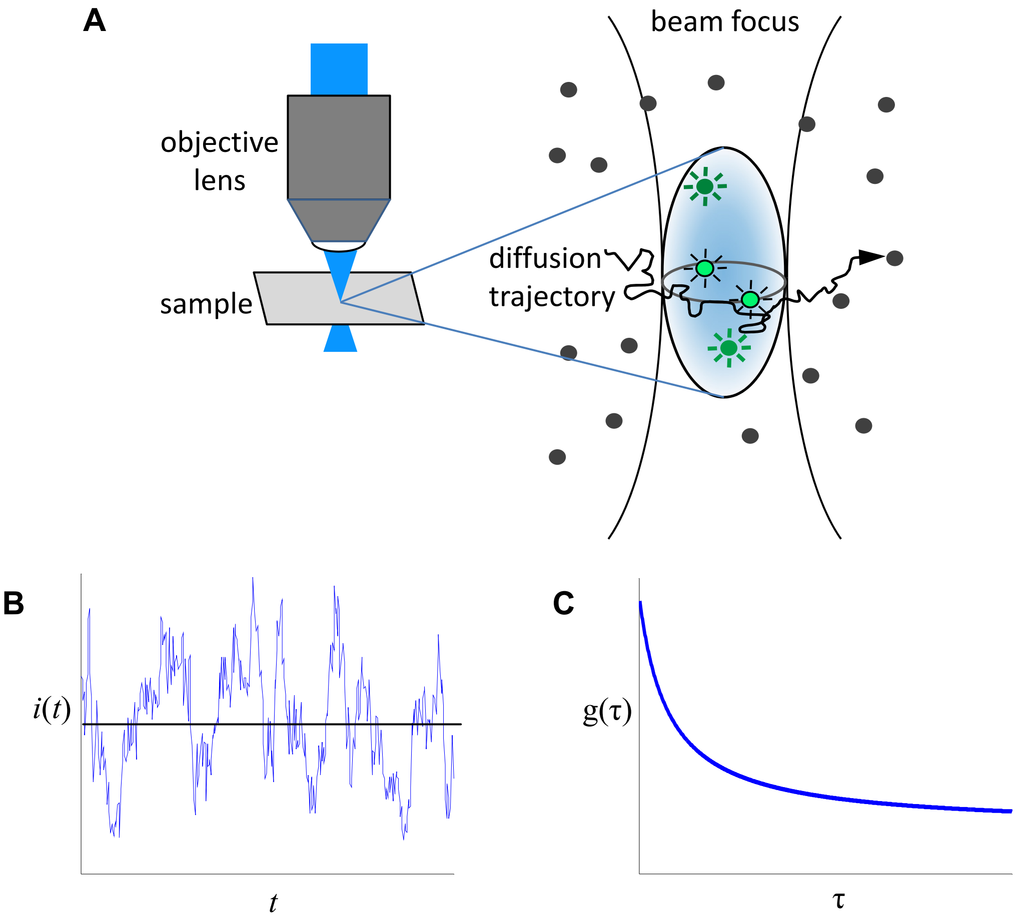

FIGURE 1.12: (A) As particles enter and exit the focal volume this causes fluctuations in fluorescence intensity about the mean. (B) Fluorescence intensity is recorded over time. The average duration of fluorescence fluctuations is determined by the time it takes a particle to traverse the focus of the laser, which in turn depends on the particle's diffusion or transport speed. (C) An autocorrelation function calculated from the intensity trace in (A) can be fit to a model to determine transport dynamics.

Molecules in solution or the cell cytoplasm move rapidly enough through the stationary focal volume that many independent fluctuations are sampled within a few seconds and statistically precise measurements can be obtained. Since cell membranes are much more viscous, motion in membranes is slower and single-spot FCS would require extremely long measurement times to sample enough fluctuations of labelled proteins moving in the membrane. Alternatives were developed for measuring dynamics in cell membranes such as scanning FCS [42], where the beam is scanned in a line or circle across the sample to obtain spatial samples in addition to the temporal samples, and various image correlation spectroscopy methods [43-46], where entire image frames are used.

1.5.2 Fluorescence Recovery After Photobleaching (FRAP)

While correlation methods measure systems at equilibrium, the FRAP technique perturbs the system by photobleaching a spot with a pulse of intense laser light so that no fluorescence remains, and then monitors the return to equilibrium. Fluorescence intensity recovers over time due to diffusion of new fluorophores into the bleached region, and this recovery curve can be fit to an analytical model to determine the diffusion coefficient. Comparing the fluorescence intensity before bleaching with the maximum intensity attained after a long recovery period can also be used to infer the immobile fraction of fluorophores. The main disadvantages of FRAP are that the high illumination power used can damage biological samples and may even affect the dynamics of the system, and that fluorophores are destroyed so that the measurement cannot be repeated in the same area [47]. Unlike FCS, FRAP cannot determine the concentrations or aggregation states of labelled molecules.

1.5.3 Single Particle Tracking (SPT)

In SPT, the imaged diffraction patterns of individual particles are tracked over time by video microscopy imaging. To achieve single molecule localization, the density of labelled molecules must be very low, so that the PSFs of separate particles do not overlap. Since the particles are moving, they must generally be spaced much farther apart than the width of the PSF to minimize events of particles “merging” together as they travel near one another. This density is much lower than the concentration of most endogenous proteins in cells, and so SPT cannot generally be done with genetic fusions to fluorescent proteins using standard expression levels. Although single organic fluorophores and fluorescent proteins can be detected with sensitive CCD cameras now available, probes with very high contrast and greater photostability are usually preferred for SPT. Traditionally, colloidal gold beads or latex spheres (~40 nm in size) could be detected because they scatter light [48]. A drawback of these probes is that their large size raises the question of how much they perturb the natural behaviour of the much smaller labelled molecules. More recently, QDs have been used in SPT experiments [25, 49-50] for their bright fluorescence and photostability. In this case, the blinking emission of the QDs complicates tracking the particles, and tracking algorithms have been developed that attempt to account for this [51]. Newer tracking algorithms have also improved the ability to handle slightly more dense samples by efficient merging and splitting of particle tracks [52] and using global optimization to determine the most likely combined set of trajectories [53].

To measure particle diffusion with SPT, one analyzes the trajectories of individual molecules as in Fig. 1.13 (A). A plot of the mean squared displacement (MSD) of the particle versus time (Fig. 1.13 (B)) can be used to determine the rate and mode of transport (free diffusion, confined diffusion, or active transport). One of the great strengths of SPT is that, because the PSF originating from a single particle can be observed, the particle's location can be determined with high precision (usually 5 – 40 nm) by fitting the imaged particle diffraction spot to determine the centroid of its fluorescence emission peak. Thus, SPT has been used to measure cell membrane properties that occur at length scales below the diffraction limit (~200 nm), such as diffusion of molecules transiently confined by the cell's cytoskeleton [48, 54]. SPT is also capable of distinguishing heterogeneity in individual particle movement that is not accessible with ensemble-averaged techniques. In many cases the mobility of identical particles differs, with some appearing confined, whereas others diffuse freely (see results in Sec. 4.2). Individual particles can also change between modes of free diffusion, confined diffusion, and immobility within a single trajectory [11, 55].

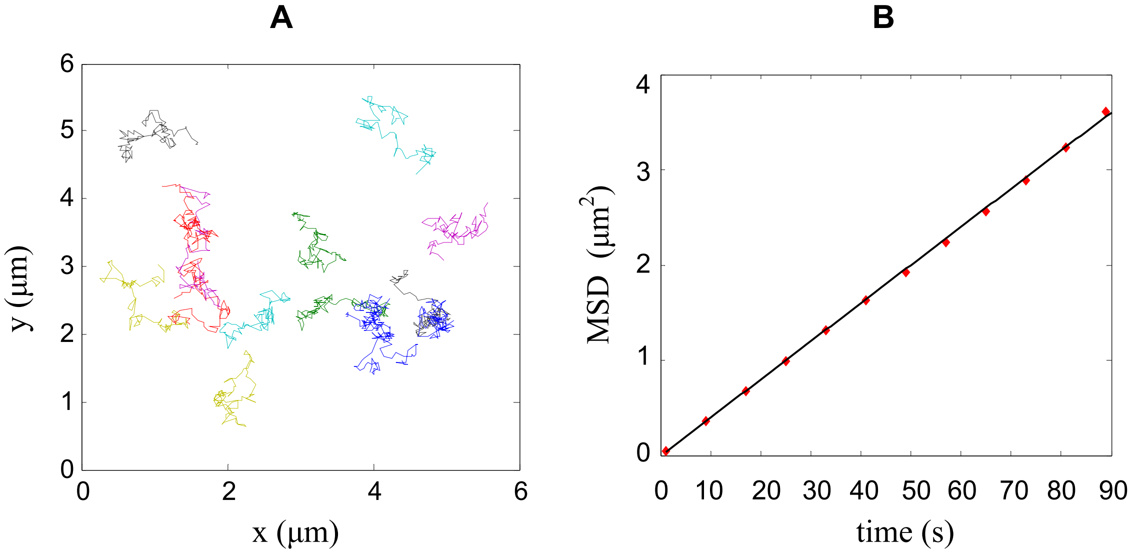

FIGURE 1.13: (A) Simulated single molecule trajectories, as might be acquired in an SPT experiment. Different tracks are represented by different colours. (B) A plot of the mean squared displacement versus time. The MSD from a single trajectory or multiple trajectories is calculated by averaging a particle's displacement between all time points in its trajectory spaced by a given time window. The MSD plot can examined to determine whether diffusion is free or confined, and fit with a model to measure the diffusion speed.

Despite its many advantages, SPT can be difficult to apply: a high signal-to-noise ratio is required, the labelling density must be very low, and tracking can be time consuming and often requires manual linking of trajectory segments. Also, a large number of experiments usually need to be done to have adequate statistical sampling of particle motion.

1.5.4 Temporal Image Correlation Spectroscopy (TICS)

While FCS records fluorescence fluctuations at a single position over time, ICS examines spatial fluctuations that occur in individual fluorescence images. Thus, when particle motion is relatively slow, or even when cells are fixed, one can use ICS to quickly sample a large number of independent fluctuations for accurate determination of membrane protein densities and aggregation states [43, 56]. ICS has also been extended to the time domain by calculating the time autocorrelation decay across multiple images, referred to as temporal image correlation spectroscopy (TICS) [44]. TICS has been applied to measure diffusion of cystic fibrosis transmembrane conductance regulator [57] and the flow speed of cell adhesion proteins [58]. A key consideration when applying TICS is that photophysics of the fluorescent labels strongly affect the correlation decay and can lead to biased results [59]. Bias due to photophysics also affects one- and two-photon FCS [60-61]. When an appropriate model for the photophysics can be determined, the bias can be corrected for.

1.5.5 k-Space Image Correlation Spectroscopy (kICS)

kICS is a correlation technique developed recently in the Wiseman lab which, like TICS, computes correlations between image frames to determine particle motion dynamics. However, in kICS, each individual image is first 2D Fourier transformed to its k-space spatial frequency representation, and the time correlations are then computed from the k-space image stack. The k-space time correlation decay is fit to an analytical model to determine diffusion or flow. In Chapter 2 we present the theory behind kICS and describe with examples how to extract diffusion or flow parameters. kICS has numerous advantages over TICS, such as insensitivity to particle photophysics (blinking or photobleaching), the ability to measure flow direction, increased precision, and improved dynamic range. When analyzing small spatial regions, however, kICS suffers from bias introduced by the discrete nature of the Fourier transform. The advantages of kICS and corrections for the bias are examined in more detail in Chapter 3.

1.5.6 Fourier Image Correlation Spectroscopy (FICS)

Fourier Image Correlation Spectroscopy (FICS) is a technique very similar in principle to kICS, though the data is acquired differently. With FICS, an interference pattern is generated by two overlapping laser beams to excite a single spatial frequency in the sample [62]. The total sample fluorescence is collected over time and is autocorrelated. Information about different spatial frequencies can be collected in sequential measurements, and typically only a few spatial frequencies are probed, under the assumption that the measured dynamics are isotropic. FICS has a very wide dynamic range, and can theoretically sample fluorescence fluctuations occurring on time scales from 10^{-8} to 10^{2} s, at any single spatial scale above the diffraction limit. FICS has been used to measure motion of the mitochondrial reticulum [63], and the diffusion coefficient of fluorescent proteins in solution [64].

FICS can be much more sensitive than kICS because fluctuations at the chosen spatial frequency are measured by a lock-in detection method, where the phase of the excitation pattern is modulated at high frequency (~50 kHz). This excludes both noise and density fluctuations that occur at other frequencies. FICS also makes more efficient use of the collected photons than imaging methods, which enables longer time series to be collected before photobleaching occurs. However, despite being described a decade ago, FICS has seen only limited use. This could be because of the specialized equipment required: a custom-built apparatus to focus two laser beams to interfere at the sample, a lock-in amplifier for detection, and a translation stage or movable grating to modulate the interference. In contrast, kICS can be used with a standard fluorescence microscope of any type: a wide-field microscope, CLSM, or total internal reflection fluorescence (TIRF) microscope. Also, kICS probes many spatial frequencies in a single, brief (1 – 2 min) measurement. Finally, though photobleaching may be reduced in a FICS measurement, FICS is not completely insensitive to photobleaching, as is the case for kICS.

1.5.7 Other Techniques and Variants

Other correlation techniques exist for measuring particle diffusion, directed transport, and number densities, but will be mentioned here only briefly.

Spatiotemporal image correlation spectroscopy (STICS) is an extension of TICS which computes the full spatiotemporal correlation function from an image series; thus, all spatial correlations are considered as well as temporal correlations. This enables STICS to accurately determine the direction and magnitude of molecular flow within small image regions. STICS has been applied in a number of systems to measure directed motion, including flow of adhesion related proteins in cells [45], movement of myosin II and actin during cytokinesis [65], movement of vesicles in growing pollen tubes [66], and migration of cells during wound healing after injury [67].

Raster image correlation spectroscopy (RICS) is a clever technique that takes advantage of the hidden time structure within individual images collected on a CLSM [68]. In a CLSM image adjacent pixels in the horizontal (scan) direction are acquired microseconds apart in time, while adjacent pixels in the vertical direction are sampled milliseconds apart due to the raster scan of the laser beam. RICS thus has a very high dynamic range and is able to measure diffusion coefficients greater than 100 $\mu m^2/s$, or as low as those measured with TICS via correlation between image frames. RICS analysis software is now included directly with new commercial confocal microscopes from Zeiss. Because it is dependent on time structure within an image, RICS cannot be used with TIRF microscopy or wide-field microscopy.

The pair correlation function (pCF) approach was introduced as a way to measure barriers to diffusion within a cell, though it can also be applied to general diffusion measurements [69]. Like STICS, correlations between pixel intensities are calculated with both spatial and temporal lag variables. When a pCF is computed at a given spatial separation between points, the maximum correlation occurs after a specific time delay that is related to the separation distance and the average diffusion speed. A similar correlation between spatially separated regions is computed in the technique called imaging total internal reflection fluorescence cross-correlation spectroscopy (ITIR-FCCS) [70]. With ITIR-FCCS, the sensitivity of TIRF microscopy and the use of a high-speed electron-multiplied CCD camera made it possible to measure the relatively fast diffusion of lipids in supported lipid bilayers [71] and of a lipid raft marker in cells [70].

In this chapter, we have introduced concepts relating to fluorescence microscopy of living cells, and discussed a number of techniques for measuring the dynamics of fluorescently labeled macromolecules. In the next chapter, we delve into the details of the kICS technique, first deriving the key kICS equations, and then describing data fitting procedures using examples.

2. k-Space Image Correlation Spectroscopy: Theory and Data Analysis

A variety of techniques are available for measuring diffusion and directed transport of fluorescently labelled molecules in living cells, as discussed in the previous chapter. Of these, fluorescence correlation techniques have the advantage of being able to measure samples with a very wide range of concentrations, including the range of natural protein expression levels in cells. The ability to distinguish single molecules is not required, and the available techniques can access a wide range of time scales, from microseconds to minutes. Because a large amount of data is collected in a single experiment, precise statistical determination of average diffusion or flow behaviour is possible. However, a factor that must be considered in all such experiments is how photophysics of the fluorophore labels influences the measurements, since they are based on analysis of fluorescence fluctuations.

Organic fluorophores such as fluorescent proteins can undergo both permanent and reversible photobleaching [72-73]. Quantum dots are less commonly used in fluorescence correlation studies because of their widely known emission blinking, which usually follows power law statistics and has no characteristic time scale [24, 26]. In both FCS and TICS, if intensity fluctuations due to fluorophore photophysics are not corrected for, the experimental data may appear to be well fit by a model that accounts only for molecular transport, but the measured values may be highly erroneous due to hidden systematic error [59-60, 74-75]. Because photobleaching and blinking are time-dependent, any technique that fits a time-dependent correlation decay will be biased unless these fluorophore photophysics are explicitly and correctly accounted for. In contrast, kICS fits a spatial correlation decay in reciprocal space. Under the assumption that the photophysics are not spatially dependent, then in kICS photophysical fluctuations are separated from transport fluctuations, and the transport properties may be measured without this bias, as has been shown in the seminal paper introducing kICS [46].

In this chapter, we introduce the theory behind kICS and the models that can be fit to measure a sample's diffusion or flow. We also describe the data fitting procedures with examples of different scenarios.

2.1 kICS Theory

Here, we derive an equation for the kICS correlation function, and show how it can be used to extract information on the number density and transport dynamics of the fluorescent particles in the sample. This derivation closely follows that in the original kICS publication [46].

To apply kICS one first acquires a time series of fluorescence microscopy images, $i(\mathbf{r},\mathrm{t})$, from the sample. Any standard microscopy method can be used, including epifluorescence, laser scanning microscopy, or TIRF microscopy. One computes the 2D spatial Fourier transform for each image in the series, $\tilde{i}(\mathbf{k},t)$, so that the transformed images are now a function of the reciprocal space variable **k** rather than real space position **r**. One then calculates the k-space time correlation function, $r(\mathbf{k},\tau)$, for a series of time lags τ:

$$r(\mathbf{k},\tau) = \langle \tilde{i}(\mathbf{k},t)\overline{\tilde{i}(\mathbf{k},t+\tau)}\rangle \tag{2.1}$$

Here, $\tilde{i}(\mathbf{k},t)$ is the Fourier transform of the image acquired at time t, $\overline{\tilde{i}(\mathbf{k},t)}$ is its complex conjugate, and the angular brackets denote averaging over time, t, with τ being the time lag variable for the correlation. Thus, $r(\mathbf{k},\tau)$ is simply the average product of the Fourier transformed images separated by a time lag τ. We now consider how to represent the Fourier transform of an image in terms of particle positions and the microscope PSF.

In a physical model of a fluorescence microscopy image, the microscopic density of labeled particles, $\rho(\mathbf{r},t)$, is convolved (*) with the microscope's PSF, $I(\mathbf{r})$, to produce the image, $i(\mathbf{r},t)$:

$$i(\mathbf{r},t) = qI(\mathbf{r}) * \rho(\mathbf{r},t) \tag{2.2}$$

where q is a constant that includes the quantum yield of the fluorophore, the photon collection efficiency, and the detector gain. We will assume here that a 2D sample is being imaged, but note that the kICS correlation can be computed and fit without any modifications if the sample includes 3D movement (see Ref. [46]). The microscopic number density of fluorescing particles at point **r** and time t is given by:

$$\rho(\mathbf{r},t) = \sum_{\mathrm{i}=1}^{\mathrm{N}} \Theta_{\mathrm{i}}(\mathrm{t})\delta(\mathbf{r}-\mathbf{r}_{\mathbf{i}}(\mathrm{t})) \tag{2.3}$$

Here, the sum is over all *N* particles in the system, δ is the Dirac δ-function, and $\mathbf{r}_\mathrm{i}(t)$ is the position of the i^{th} particle at time *t*. This expression for the number density only includes particles that are emitting fluorescence at time *t* due to the factor $\Theta_\mathrm{i}(t)$:

$$\Theta_\mathrm{i}(t) = \begin{cases} 1 & \text{if i is emitting at time } t \\ 0 & \text{otherwise} \end{cases} \quad . \tag{2.4}$$

We assume that $\Theta_\mathrm{i}(t)$ is dependent only on time and not on particle position (which implicitly assumes constant illumination across the field of view). The PSF of the imaging system can be approximated as a 2D Gaussian function characterized by its e^{-2} radius in the lateral direction, ω_0^2:

$$I(\mathbf{r}) = I_0 \exp\left[-2\left(\frac{x^2 + y^2}{\omega_0^2}\right)\right] \tag{2.5}$$

I_0 is the illumination intensity at the center of the focus.

The convolution theorem states that the Fourier transform of a convolution is simply the product of the individual Fourier transforms. In real space the image is a convolution of two functions, $I(\mathbf{r})$ and $\rho(\mathbf{r},t)$; thus, the Fourier transformed image, $\tilde{\imath}(\mathbf{k},t)$, is the product of the spatial Fourier transforms of these functions:

$$\tilde{\imath}(\mathbf{k},t) = q\tilde{I}(\mathbf{k})\tilde{\rho}(\mathbf{k},t) \tag{2.6}$$

where $\tilde{f}(k)$ is the Fourier transform of function $f(x)$ for variable *x*. The 2D spatial Fourier transform of the PSF (Eq. 2.5) is:

$$\tilde{I}(\mathbf{k}) = \frac{I_0\omega_0^2\pi}{2}\exp\left[-\frac{\omega_0^2|\mathbf{k}|^2}{8}\right] \tag{2.7}$$

The 2D spatial Fourier transform of the number density (Eq. 2.3) is:

$$\tilde{\rho}(\mathbf{k},t) = \sum_{p=1}^{N}\Theta_p(t)\exp\left[i\mathbf{k}\cdot\mathbf{r}_{\boldsymbol{p}}(t)\right] \tag{2.8}$$

where subscript $_p$ represents a particle in the count, and $i = \sqrt{-1}$. We can substitute these last two equations into Eq. 2.6 to obtain an expression for the k-space image in terms of particle positions and the PSF:

$$\tilde{\imath}(\mathbf{k},t) = \frac{qI_0\omega_0^2\pi}{2}\sum_{p=1}^{N}\Theta_p(t)\exp\left[\mathbf{k}\cdot\mathbf{r}_{\boldsymbol{p}}(t) - \frac{\omega_0^2|\mathbf{k}|^2}{8}\right] \tag{2.9}$$

Recall that the kICS correlation function, $r(\mathbf{k},\tau)$, is the average product of pairs of k-space images separated by a time lag τ. Substituting Eq. 2.9 into Eq. 2.1 we now have:

$$r(\mathbf{k},\tau) = \frac{q^2 {I_0}^2 \omega_0^4 \pi^2}{4} \langle \sum_{p=1}^{N} \Theta_p(t) e^{\mathbf{k}\cdot\mathbf{r}_p(t) - \frac{\omega_0^2 |\mathbf{k}|^2}{8}} \sum_{q=1}^{N} \Theta_q(t+\tau) e^{-\mathbf{k}\cdot\mathbf{r}_q(t+\tau) - \frac{\omega_0^2 |\mathbf{k}|^2}{8}} \rangle \tag{2.10}$$

If we assume that the fluorescent particles are sufficiently dilute that they are independent, and thus only correlate with themselves, then the cross-product terms from the two sums average to zero (i.e. $\langle e^{\mathbf{k}\cdot\mathbf{r}_p(t)} e^{\mathbf{k}\cdot\mathbf{r}_q(t+\tau)} \rangle = 0$ for $p \neq q$). We can thus drop the *p* and *q* subscripts and only sum once over all particles. Furthermore, if we assume that particles are identical, and given our assumption that the fluorescence emission function, Θ(*t*), depends only on time and not on any other dynamic processes, Eq. 2.10 becomes:

$$r(\mathbf{k},\tau) = N \frac{q^2 {I_0}^2 \omega_0^4 \pi^2}{4} \langle \Theta(t)\Theta(t+\tau) \rangle \langle \exp\left[i\mathbf{k} \cdot \left(\mathbf{r}(t) - \mathbf{r}(t+\tau) \right) - \frac{\omega_0^2 |\mathbf{k}|^2}{4} \right] \rangle \tag{2.11}$$

Following sections 5.4 and 5.8 of Berne and Pecora [76], for a system with one population of particles undergoing diffusion, flow, or both (i.e. diffusive flow), Eq. 2.11 becomes:

$$r(\mathbf{k},\tau) = N \frac{q^2 {I_0}^2 \omega_0^4 \pi^2}{4} \langle \Theta(t)\Theta(t+\tau) \rangle \exp\left[i\mathbf{k} \cdot \mathbf{v}\tau - |\mathbf{k}|^2 \left(D\tau + \frac{\omega_0^2}{4} \right) \right] \tag{2.12}$$

where *D* is the diffusion coefficient, and **v** is the velocity of the flowing particles.

Though Eq. 2.12 appears complex, the parameters of interest, namely *D* and **v**, are linked to decay of the correlation via their dependence on $|\mathbf{k}|^2$ and $i\mathbf{k}$, respectively; the remaining factors are independent of **k**. Rather than fitting directly to Eq. 2.12, we follow the method outlined in Ref. [77] and divide $r(\mathbf{k},\tau)$ at each time lag τ by the zero-time-lag correlation, $r(\mathbf{k},0)$, to obtain a "normalized" correlation function that is independent of the point spread function (PSF) of the microscope. After log transforming, this gives:

$$\ln\left[\frac{r(\mathbf{k},\tau)}{r(\mathbf{k},0)} \right] = \ln[\langle \Theta(t)\Theta(t+\tau) \rangle] + i\mathbf{k} \cdot \mathbf{v}\tau - |\mathbf{k}|^2 D\tau \tag{2.13}$$

With this normalization, all factors that are not time dependent have dropped out of the equation. This includes fluorophore concentration and brightness, illumination intensity, and also the PSF of the microscope. In the next section we show examples of how to extract the flow velocity and diffusion coefficient from the kICS correlation function.

2.2 kICS Data Analysis for Single Population Diffusion

When directed transport can be ignored, we can measure diffusion for a single population by fitting directly to Eq. (2.13) assuming that $\mathbf{v}$ is zero. To do this, we first circularly average the correlation function at identical ($|\mathbf{k}|^2$,τ), where $|\mathbf{k}|^2 = k_x^2 + k_y^2$. We then plot $\ln[r(|\mathbf{k}|^2,\tau) / r(|\mathbf{k}|^2,0)]$ versus $|\mathbf{k}|^2$ to obtain a linear plot, which we term a $|\mathbf{k}|^2$ plot. At a given time lag τ, the initial slope of the correlation function decay in a normalized $|\mathbf{k}|^2$ plot is $-D\tau$. For the specified time lag τ, there will be a maximum $|\mathbf{k}|^2$ value at which correlations are lost and above this value a white noise "floor" is reached. The fitting of the $|\mathbf{k}|^2$ plot takes this into account, as is described below (Fig. 2.1 A). Theoretically we could determine D directly from a single $|\mathbf{k}|^2$ plot, but better results are obtained when multiple time lags are considered. We thus determine the slopes from $|\mathbf{k}|^2$ plots for each temporal lag of the correlation function. Finally, these slopes, $-D\tau$, are plotted as a function of time lag, τ, as in Fig. 2.1 (B). We call this the dynamics plot. A linear regression to this plot has a slope of $-D$.

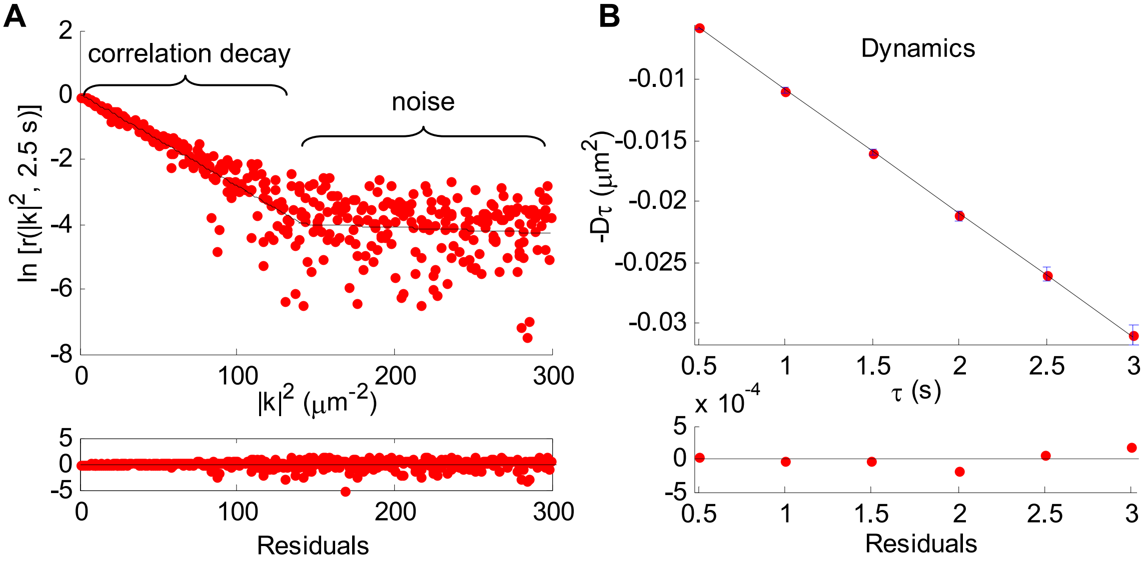

FIGURE 2.1: (A) The normalized $|\mathbf{k}|^2$ plot for time lag 2.5 s from kICS analysis of simulated diffusion, showing a bilinear fit to the circularly averaged $\mathbf{k}$ values. The slope of the first segment is $-D\tau$, and corresponds to the point at 2.5 s in the dynamics plot. (B) The dynamics plot for the same kICS analysis, from which D is determined. The error bars are the standard error from linear regressions in the corresponding $|\mathbf{k}|^2$ plots.

Note that in Fig. 2.1 (A) a bilinear fit to the data (black line) is shown. As $|\mathbf{k}|^2$ and τ increase, correlations due to particle motion become insignificant compared to noise. The first linear segment models correlation decay due to diffusion and is the slope we want to measure, while the second segment is the noise. In a kICS measurement, one must choose cut-off values for $|\mathbf{k}|^2$ and τ to avoid fitting noise and introducing bias in the measurement. In general, one cannot know suitable cut-off values before performing the analysis and having an estimate of the diffusion coefficient; thus, a bilinear fit is an efficient and unbiased way to fit the data without specifying arbitrary cut-off values. Unfortunately, the nonlinear fit that determines the two linear segments is itself sensitive to noise occurring near and after the transition point. At best, the first linear segment includes correlation function values that have already decayed significantly into the noise. At worst, in some cases the assignment of the transition point is clearly wrong and the slope determined is spurious.

A solution to such problems is to do the data fitting in two stages. First, a bilinear fit is done to get an estimate of the diffusion coefficient and to determine visually what cut-off values of $|\mathbf{k}|^2$ and τ enable a linear fit that remains above the noise level for the highest τ used. Second, the data fitting is redone with a linear fit to the data that is within these cut-offs, which gives a more accurate measurement of the diffusion coefficient.

Sometimes it is useful to look at the full two-dimensional correlation function itself; in Sec. 3.2 we will see that the kICS correlation function can be perturbed due to spectral leakage resulting from the finite nature of the spatial Fourier transforms used in kICS. Fig. 2.2 shows an example of the real part of both the raw and normalized correlation functions computed from an image series of simulated particle diffusion. (More details on these and other simulations are given in section 2.3.)

When measuring diffusion, there are a number of advantages to normalizing the correlation function by dividing $r(\mathbf{k},\tau)$ by the zero time lags correlation $r(\mathbf{k},0)$. First, the transition to noise is clearly visible in the normalized correlation function (Fig. 2.2, C and D), with the noise having a slope of zero. In the raw correlation function (Fig. 2.2, A and B) the noise occurs at exactly the same values of $\mathbf{k}$, but this is hidden by the underlying shape of the correlation function; one is thus more likely to choose a $|\mathbf{k}|^2$ cut-off that includes noise when fitting the data if normalization is not used. Another practical benefit of normalization is that the value now represents the fraction of the original correlation that remains at any given value of $|\mathbf{k}|^2$ and τ. For example, when the correlation in a normalized $|\mathbf{k}|^2$ plot has decayed to –2 (= $\ln[r(\mathbf{k},\tau) / r(\mathbf{k},0)]$), this indicates that e^{-2} = 13.5% of the original correlation still persists at that $|\mathbf{k}|^2$ and τ. We have found that with both simulated and experimental data, the transition to noise generally occurs when the correlation has decayed to between 2 and 13% of its original value, which occurs between –2 and –4 on a normalized $|\mathbf{k}|^2$ plot. In an experimental measurement the threshold at which the signal is lost in noise will depend on a number of factors, such as the fluorophore brightness, level of background noise, and the amount of spatial and temporal sampling. As a rule of thumb, it is usually safe to choose cut-off values of $|\mathbf{k}|^2$ and τ for which the normalized correlation decay is less than –2.

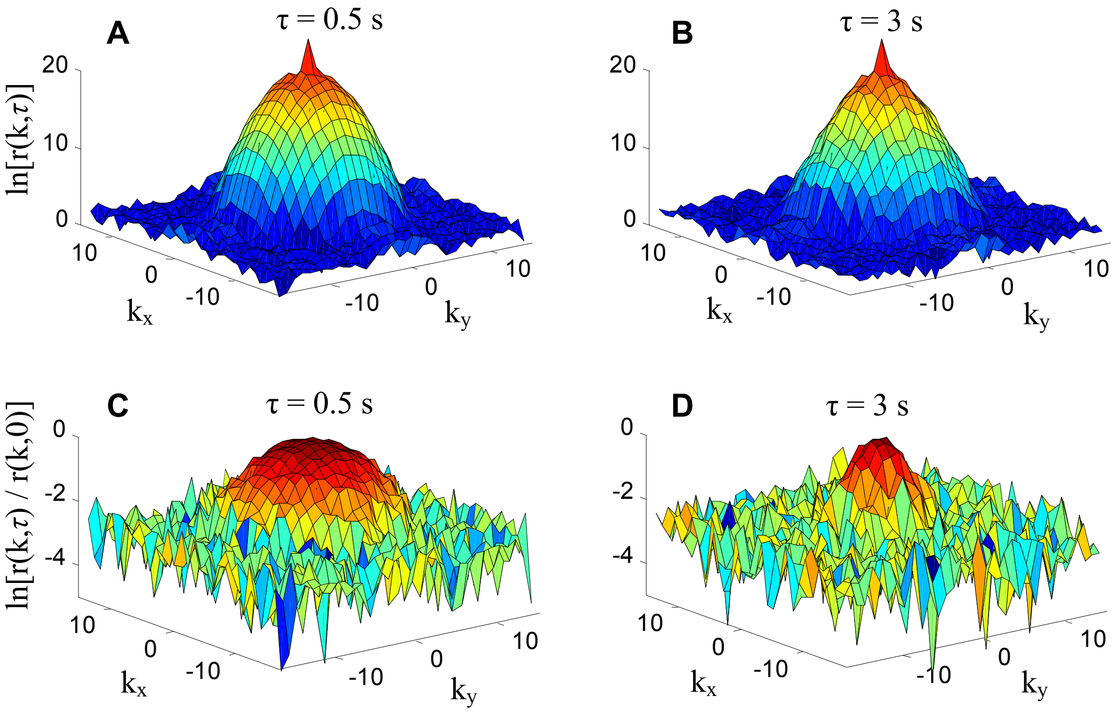

FIGURE 2.2: The real portion of correlation functions from kICS analyses of simulated particle diffusion. A and B show the raw correlation function at time lags of 0.5 s and 3 s, respectively. C and D show the normalized correlation function at the same time lags. Either form of the correlation function can be fit as described in the text to extract the diffusion coefficient of the sample. In the normalized correlation function the transition to noise is more clearly visible. The simulation had 10,000 frames at size 32x32 pixels with an image frame time-step of 0.5 s, had periodic boundaries, and D was set to 0.01 $\mu m^2/s$.

Because the k-space correlation for diffusion decays according to $\exp(-|\mathbf{k}|^2 D\tau)$, one can adjust the $|\mathbf{k}|^2$ fitting cut-off while compensating with an adjustment to the τ cut-off to achieve an equivalent maximum correlation decay. An example of such a change is summarized in Fig. 2.3. This flexibility can be seen as a strength of kICS, since the cut-offs can be adjusted to match the time scale of the actual sample diffusion; this is investigated in more detail in Section 2.5 on measurement of fast diffusion dynamics. It can also be seen as a risk, as it introduces an element of experimenter subjectivity into the measurement. A method for estimating uncertainty in a single measurement is based on the trade-off between $|\mathbf{k}|^2$ and τ cutoffs, and is discussed in Section 3.7.

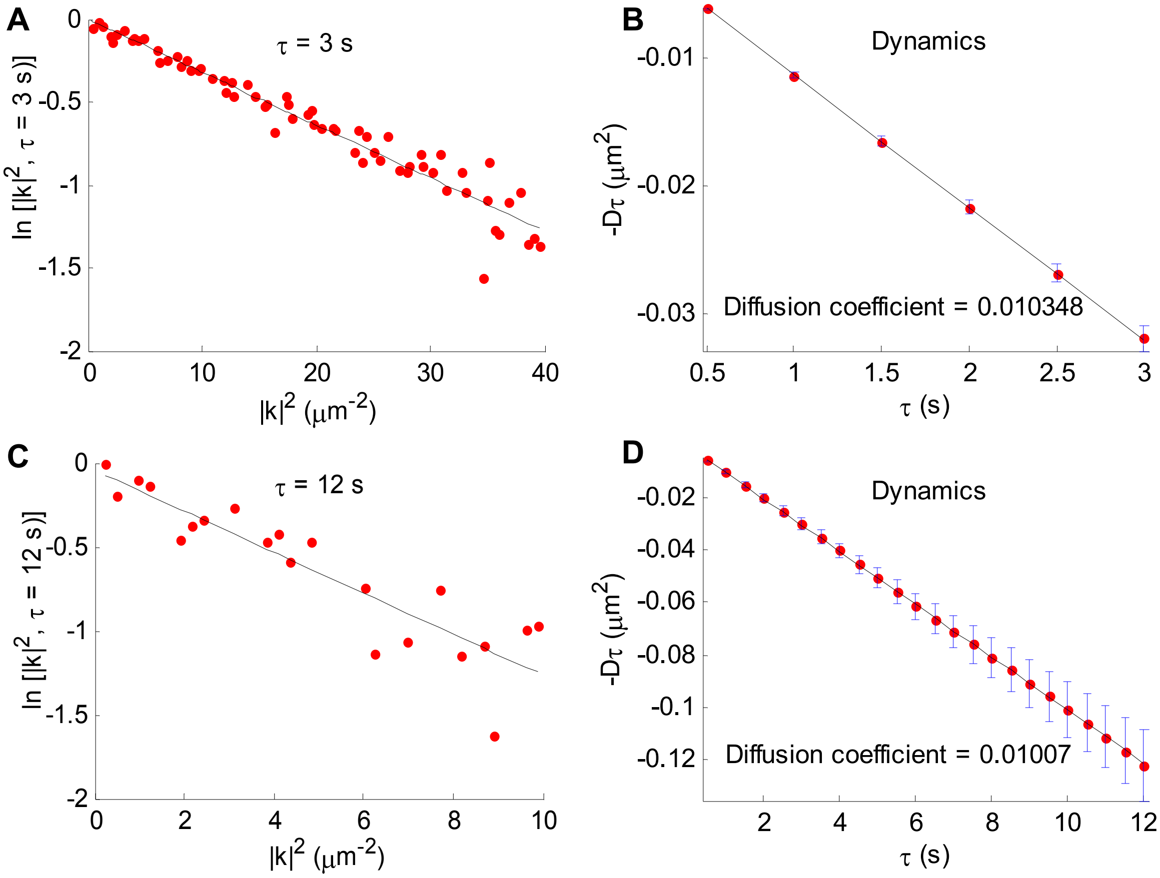

FIGURE 2.3: Two kICS analyses of the same simulated image series data as used in Fig. 2.2 using different $|\mathbf{k}|^2$ and τ cut-offs. *Top row*: analysis using cut-offs $|\mathbf{k}|^2=40$ and $\tau=6$ frames (0.5 s each), where (A) shows the $|\mathbf{k}|^2$ plot at the highest time lag and (B) shows the dynamics plot. *Bottom row*: analysis using cut-offs $|\mathbf{k}|^2=10$ and $\tau=24$ frames, where (C) shows the $|\mathbf{k}|^2$ plot at the highest time lag and (D) shows the dynamics plot. The measured diffusion coefficient is similar in each case, and is close to the set value of $D=0.01\ \mu m^2/s$.

kICS can also be used to measure the direction and speed of a flowing population of fluorescent particles. As with diffusion, flow has been examined in the original kICS publication [46]. Because flow is not investigated further in this thesis, the equations and data fitting methods relating to flow are not described here. Measurements of flow often require less spatial and temporal sampling than measurements of diffusion, because flow is deterministic whereas diffusion is random. For example, with TICS, flow speed can be accurately measured even when the image series spans a single correlation time [59]. In the next chapter, we proceed directly to examine the accuracy of kICS for measurements of diffusion.

3. k-Space Image Correlation Spectroscopy: Accuracy and Precision Explored Via Simulations

Whereas the accuracy and precision of the TICS and FCS methods have been well characterized [59, 78-79], such a study is lacking for the recently developed kICS. Both TICS and FCS can be biased under some measurement conditions, and it is thus important to know what experimental and data fitting parameters influence such measurements. In this chapter, we explore a range of spatial and temporal sampling parameters using computer-simulated image series to determine the limits of spatial and temporal resolution with kICS.

We report three unexpected findings. First, kICS measurements of diffusion are consistently biased low; this effect relates to spectral leakage in the Fourier transforms of the images, and is negligible for large images but becomes significant for image regions smaller than ~100 μm^2 (assuming the optical resolution is diffraction-limited). Second, kICS can accurately measure particle diffusion that is at least ten times faster than could be measured with TICS using the same image frame acquisition rate. We show that at video rate sampling, kICS is capable of measuring 2D diffusion up to 12 $\mu m^2/s$. This finding is particularly interesting because, like TICS or ITIR-FCS, kICS is limited to correlations between successive image frames. Third, by normalizing the kICS correlation function by its zero-time-lags value, kICS accurately measures diffusion even with a highly inhomogeneous initial distribution of particles. Because of this, kICS can be used to measure diffusion in systems that until now required fitting by special-purpose models, such as after localized fluorophore photoconversion [80], or photouncaging [81-82].

3.1 Computer Simulations

3.1.1 Particle Diffusion and Flow

Computer simulated image time series are the primary tool used in this chapter to investigate the accuracy and precision of kICS, and so will be described in some detail. The software routines to make simulated image series are implemented in Matlab (The MathWorks, Natick, MA) and the core routines have been described previously [59]. The simulations are meant to model a series of fluorescence microscopy images acquired over time from a two dimensional sample containing fluorescent point emitters such as a cell membrane. Image dimensions are specified by an integer number of pixels in x and y, and by the width of a square pixel as a floating-point number measured in micrometers. The total number of images and the time between images is also specified. Initial particle positions are assigned by drawing from a uniform probability distribution over the range of coordinates in each dimension, and particle positions are always stored as double precision floating-point numbers. To create an image modeling that acquired on an optical microscope, particle coordinates are rounded and assigned to a position in a matrix, and the matrix is convolved with a 2D Gaussian filter to simulate excitation with a laser beam having a Gaussian intensity profile (or a Gaussian optical PSF). Pixel intensity values are multiplied by a gain factor that represents the number of photons emitted by each fluorescent particle. The values are then rounded to integers in the range 0 to 4095, simulating a 12-bit analog-to-digital conversion as done in a photomultiplier tube (PMT) detector. Fig. 3.1 shows an example image created with this procedure.

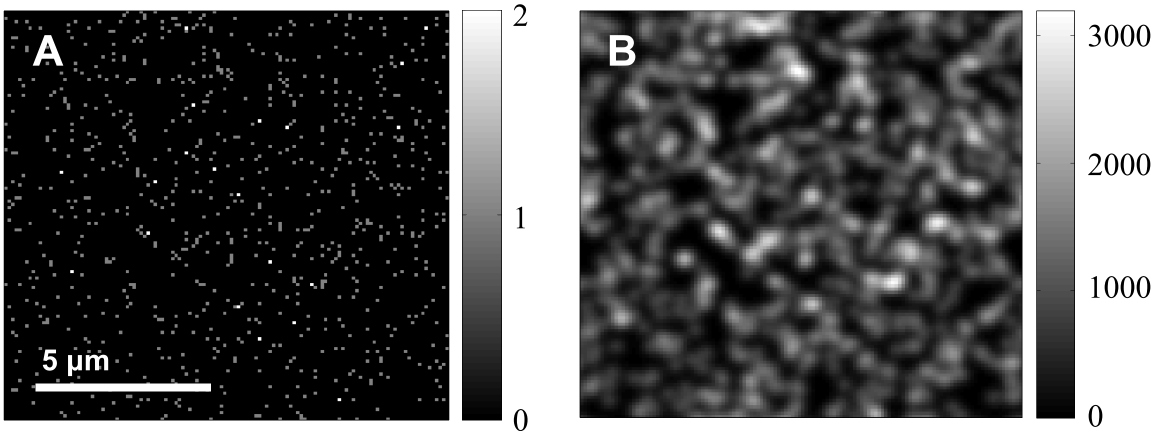

FIGURE 3.1: Example of a computer simulated image. (A) Positions of point source emitters in the image matrix before convolution. The image is 128 x 128 pixels^2 with a pixel size of 0.1 µm and a particle density of 5 particles/µm^2. The scale bar represents the number of particles. (B) The image formed after convolving the matrix in (A) with a Gaussian filter with an e^{-2} radius of 4 pixels. No noise has been added to the image. The scale bar represents integrated intensity.

To simulate diffusion, at each timestep the x- and y- coordinates of each particle are separately changed by adding a pseudorandom number drawn from a normal distribution with a mean of zero, and standard deviation σ:

$$\sigma = \sqrt{2D\Delta t} \tag{3.1}$$

where D is the diffusion coefficient and Δt is the time between successive images in the series. Thus, a particle diffuses as a 2D random walk with uniform time steps and spatial step sizes selected from a Gaussian distribution. Two kinds of boundary conditions can be implemented for particle movement near the edge of an image: circular or open. With a circular boundary condition, particles that exit one side of the image appear on the opposite side of the image. Also, the Gaussian filter is circularly convolved so that the PSF of a particle near the edge of the image wraps around to the other side. Edge boundary conditions have a significant effect when the Fourier transform of an image is considered, as will be discussed later. An open boundary condition can also be implemented. This is done simply by increasing the size of the image in the x and y dimensions by a number of pixels equal to 5 PSF radii. Thus, a particle that exits the image on one side may later re-enter on the same side, or eventually may enter on the opposite side after it has traveled a distance of 5 PSF radii.

Particle flow is simulated by adding a constant floating point value separately to the x and y coordinates of each particle at each time step. Diffusion and flow can simultaneously be present in a simulation, in which case the new particle coordinates are the sum of the separate changes due to diffusion and flow.

These simulations do not account for a number of possible real-world effects that can cause non-ideality in particle diffusion or fluorescence emission. Particles are assumed to be independent at the densities simulated in this work, with no attractive or repulsive interactions, and no excluded volume effects. We also assume that there is no fluorescence resonance energy transfer (FRET) or quenching. All simulations were done within the dynamic range of the 12-bit image representation (i.e. there was no saturation). All particles were assumed to be in focus, which is not always the case in microscopy experiments.

3.1.2 Background and Photon Counting Noise

In any real fluorescence microscopy image there are always noise contributions that get recorded in the image. Noise can be defined as any detectable signal that does not originate from the real object (molecule/fluorophore) of interest. One such undesired component is background signal, which is background intensity that can result from sources such as scattered laser light, cell autofluorescence, nonspecifically bound fluorophore, or weak fluorescence from the sample medium. In an image correlation analysis one should first correct the region analyzed by subtracting the mean intensity of an off-cell region. This correction removes the average background signal itself, but does not remove the positive fluctuations from the background signal, which we call the background noise. To simulate this residual background noise we add a random value to each pixel of the image as follows. A noise matrix, **U**, is created with the same dimensions as the noise-free image matrix, **A**. The values, u_{ij}, of **U** are random numbers from a normal distribution with a mean of zero and standard deviation of 1. To create the noisy image matrix **C**, the absolute values of the elements of **U** are multiplied by a scaling coefficient, σ, that enables one to control the signal to background ratio (S/B), and are then added to **A**:

$$c_{ij} = a_{ij} + \sigma|u_{ij}| \tag{3.2}$$

The S/B of the image series is defined as:

$$S/B = \frac{\text{mean of the peaks in } (\mathbf{A})}{\sigma} \tag{3.3}$$

Photon counting noise occurs due to random fluctuations in the number of detected photons in any photon counting detection scheme. Since fluorescence emission can be modeled as a stochastic process, we also model our underlying detection with Poisson counting statistics. Thus, the number of photons collected will vary according to a Poisson distribution about the mean number, *N*. For large enough *N*, the Poisson distribution approaches a normal distribution with standard deviation $\sqrt{N}$. An analog detector such as a PMT broadens the underlying Poissonian photon counting noise distribution so that the real standard deviation is greater than the $\sqrt{N}$ expected purely from a Poisson process. We thus create a counting noise matrix, **U**, with normally distributed random numbers having mean zero and standard deviation 1, and then scale it according to both the expected $\sqrt{N}$ Poisson noise as well as a width factor, WF, which is the ratio of the real counting noise to the purely Poisson noise expected. This noise matrix is added to the image matrix, A, to give the final image matrix:

$$c_{ij} = a_{ij} + \mathrm{WF}\sqrt{a_{ij}}u_{ij} \tag{3.4}$$

Examples of simulated images with differing amounts of background and counting noise are shown in Fig. 3.2.

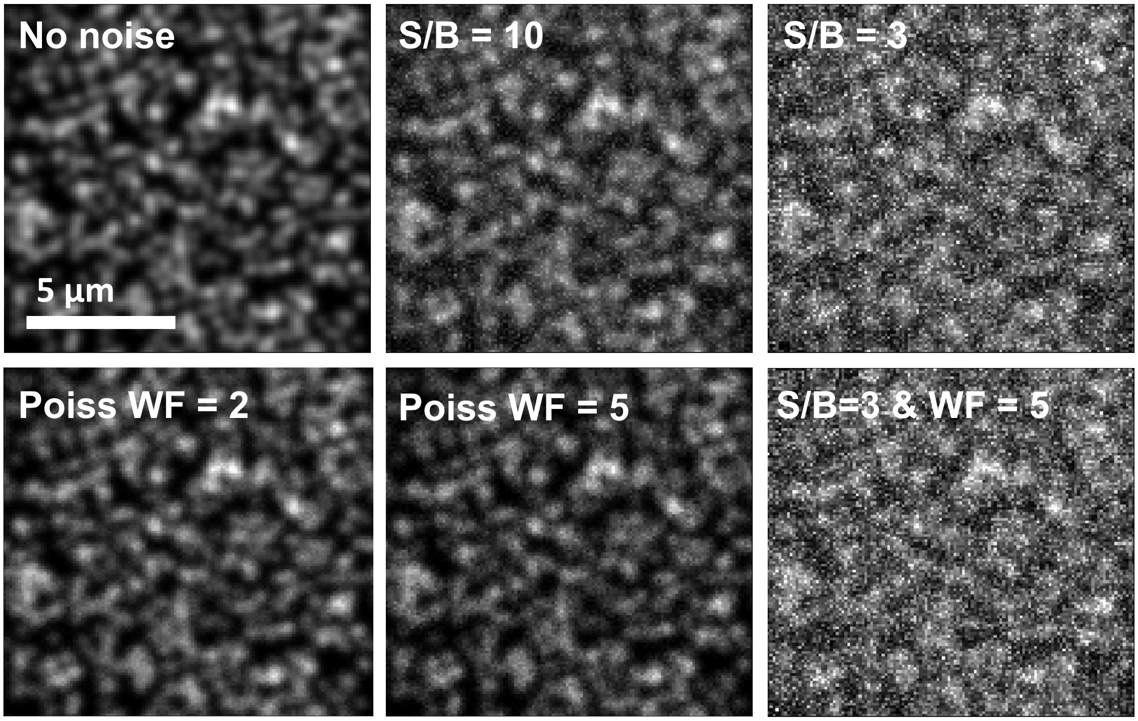

FIGURE 3.2: Matlab simulated images with differing amounts of noise. The top row shows increasing background noise from left to right. The bottom row shows Poisson noise with width factors of 2 and 5 in the first and second images. The maximum intensity is around 3000, so the signal-to-noise ratio in the image with WF=5 is around 11. The bottom right image has both background noise (S/B=3) and counting noise (WF=5); this noise setting was the one used in Sec. 3.4 to test kICS accuracy with different sampling conditions. The scale bar is the same for all images.

The simulated noise attempts to model the main sources of noise encountered in a typical microscopy experiment, but cannot fully represent all real types of noise. The simulated background noise is perfect “white noise” in that it is completely uncorrelated between image frames. In a real experiment, imperfections in laser alignment, scanning, and finite time response of the detectors may mean that some noise sources are not completely uncorrelated between frames. Detector afterpulsing is one example, where a bright pixel’s intensity causes adjacent pixels to have spuriously high readings. In addition, the excitation laser intensity can fluctuate, which adds noise to the image. Finally, cell movements, stage drift or slight changes in focus can occur over time in an image series.

3.1.3 Photobleaching

To model photobleaching in a simulation, the particle bleaching rate constant, α, is specified. This rate corresponds to a mono-exponential decay in the average image intensity as in:

$$\langle i\rangle_t = \langle i\rangle_0 \exp[-\alpha t] \tag{3.5}$$

where $\langle i\rangle_t$ is the average intensity of an image at time *t* after the start of the image series. Individual particles are bleached by setting their quantum yield in the simulation to zero. The number of particles to bleach after frame n, N_{n+1}^{bleach}, is a Poissonian random variable determined using the poissrnd built-in Matlab function as follows:

$$N_{n+1}^{bleach} = poissrnd(N_n - N_n \exp[-\alpha \Delta t]) \tag{3.6}$$

where Δ*t* is the time between image frames and N_n is the number of unbleached particles in frame n. When we want to achieve a specific fraction of bleaching over a simulated image series, we rearrange Eq. 2.8 to determine the appropriate bleaching rate constant:

$$\alpha = -\frac{\ln\left(\frac{\langle i\rangle_t}{\langle i\rangle_0}\right)}{\mathrm{N}\Delta t} \tag{3.7}$$

where N is the number of images in the series and Δ*t* is the time between image frames.

In an experimentally acquired image series, photobleaching may not be uniform over the sample and may not be mono-exponential as in these simulations. For example, exchange of bleached fluorophores may occur near the edges of the imaged region, and some fluorophores may have multi-exponential bleaching curves or reversible bleaching [73]. However, as evidenced in Eq. 2.13, the transport coefficients determined by kICS are completely independent of the fluorophore photophysics even in these cases. Since mono-exponential photobleaching is fairly common, and the other techniques discussed are biased even under this simple scenario, this implementation of stochastic mono-exponential bleaching was used in the tests of kICS accuracy to follow.

3.1.4 Default Simulation Parameters

Most details of specific simulations are given in the individual sections where the results are described. Unless otherwise noted, simulation images were 128 by 128 pixels and had a pixel size of 0.1 μm, a PSF size (Gaussian convolution radius) of 0.4 μm, a density of 10 particles per μm^2, and a *D* of 0.01 μm^2/s (to model slow membrane protein diffusion).

Background noise was added to give a S/B of 10, and counting noise was added with WF=2. By default, no photobleaching was included. For simulations used to test the accuracy of kICS at a variety of image sizes (Sec. 2.6), we used higher levels of noise (S/B=3, WF=5) and included photobleaching of 50% of particles over the image series.

3.2 Bias in kICS Measurements with Low Spatial or Temporal Sampling

We studied the effects of spatial and temporal sampling on kICS measurements using simulated fluorescence microscopy image time series, varying the number of images, time between frames, and image size, but keeping constant the transport, particle density, background noise, and PSF size.

In image correlation studies the unit of sampling is the fluorescence spatial fluctuation, so the most relevant unit in which to represent spatial sampling is the beam area (BA = πr^2, where r is the e^{-2} PSF radius). Because kICS samples fluctuations at multiple spatial scales simultaneously through the k-space representation of an image, there is no single spatial fluctuation sample size; however, the focal spot area still represents the smallest independent fluctuation that can be resolved by the optics and hence defines the largest meaningful k-vector. We represent temporal sampling in units of the characteristic “correlation time”, τ_D or τ_F (for diffusion or flow), which is the expected mean time for a particle to travel a distance equal to the e^{-2} radius of the focus. As with spatial sampling, there is no single correlation time in kICS, but we use this unit for the purpose of comparison with standard time correlation techniques.

We discovered that when analyzing small regions of computer-simulated images of a diffusing population, kICS analysis returned results that were consistently biased lower than the set D. The bias was absent when image series were simulated with a periodic boundary condition, whereby particles that exit one side of the image appear on the opposite side of the image (and moreover, the fluorescence of a particle near an edge boundary wraps around to the opposite side). Since real systems do not have periodic boundaries, any such bias is a significant concern. To fully characterize the bias, we analyzed simulations that lacked periodic boundaries over a variety of image sizes. Here, the image size in pixels was varied from 32x32 to 256x256, but other factors such as the pixel size (0.1 μm) and PSF size (0.4 μm radius) were kept constant. Fig. 3.3 shows the results, indicating that kICS analysis of diffusion is biased low by as much as 60% for very small image regions (~5 beam areas; 2.5 μm^2 in our simulations), but that the bias becomes negligible (less than 5%) for large image regions (≥ 500 beam areas; 250 μm^2 in our simulations). The bias is not affected by increased sampling in time, as we show with additional simulations described below.

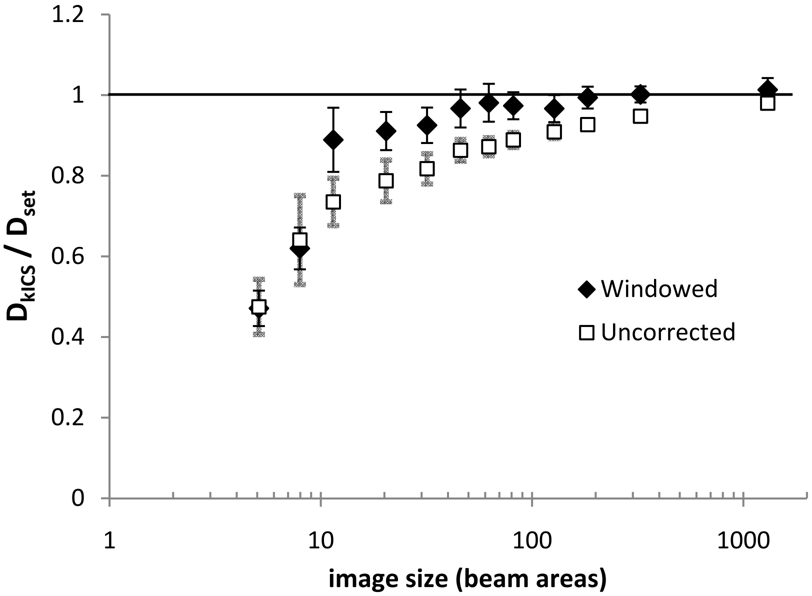

FIGURE 3.3: Mean diffusion coefficients recovered by kICS analyses on 500 "open-area" simulations of 2D particle diffusion at each image size. Values shown are relative to the set value of *D*. Images series were analyzed with no correction (squares, □) or were multiplied by a Welch window function before applying kICS (diamonds, ♦). Each simulated image series had 500 images and a frame rate of 10 frames per τ_D. Error bars are the standard deviation of recovered diffusion coefficients.

There is a clear theoretical reason for bias towards lower measured diffusion with kICS, which relates to spectral leakage in the calculated discrete Fourier transform [83]. Every real image of finite dimensions is effectively windowed by a square window function, *w(x,y)*, which is 1 for locations inside the image boundaries and zero outside the image. The discrete image collected by the microscope, *i(x,y)*, can thus be seen as a product of the "infinite-extent" real image, $i_{\mathrm{inf}}(x,y)$, and the window function, *w(x,y)*:

(3.8)

When a discrete Fourier transform is applied to the image, the product becomes a convolution:

$$\tilde{i}(k_x, k_y) = \tilde{i}_{\text{inf}}(k_x, k_y) * \tilde{w}(k_x, k_y) \tag{3.9}$$

Because the square window function drops so rapidly at the edges, its Fourier transform has considerable high-frequency components. The spacing of discrete pixels in a digital image cannot equal the Nyquist frequency for the square window function, and so spectral power from these high-frequency components is convolved with the true spectrum of the image. This causes leakage between frequency bins in the Fourier transform of the image. For kICS, this is particularly significant because for diffusion measurements we fit a correlation function that decays exponentially with $|\mathbf{k}|^2$. Even a small fractional leakage from one **k** vector to the next will be significant on a logarithmic scale and influence the fit. The effect of spectral leakage cannot readily be detected in the circularly averaged $|\mathbf{k}|^2$ plots, but it can easily be seen when looking at the 2D log-transformed correlation function (Fig. 3.4). Note that the leakage is present at all values of **k**, including the central dome, though it is more visually apparent in the "wings" at high **k**.

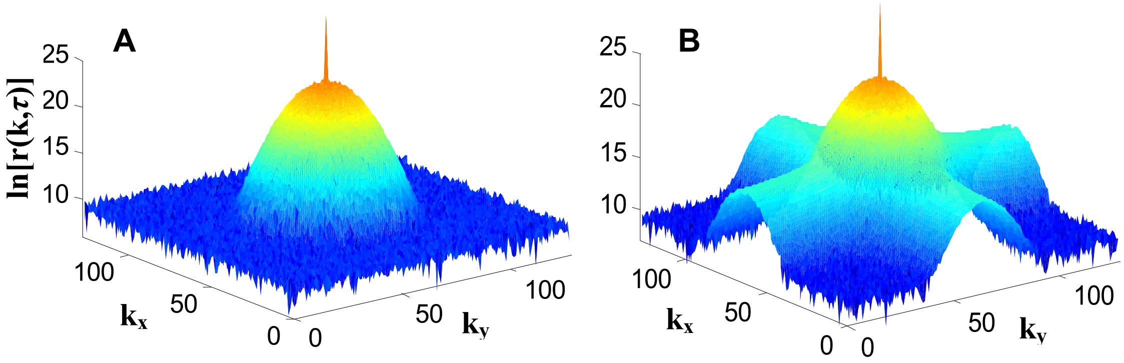

FIGURE 3.4: Change in the normalized kICS correlation function for diffusion due to spectral leakage. (A) When periodic boundaries are present in simulations then the correlation function appears normal; (B) when particles do not wrap around the image edges, as in real systems, the correlation function is perturbed due to spectral leakage.

The standard remedy for the problem of spectral leakage is to multiply the data (each image in this case) by a window function that goes to zero more gradually at the edges [83]. We again analyzed simulated image series over a range of image sizes, this time multiplying each image by a Welch window function before Fourier transforming.

This reduced the bias, but did not remove it completely, as was seen in Fig. 3.3. No matter what window function is used, some spectral leakage will still occur. Moreover, any window function, which is a type of data filter, effectively discards a fraction of the data; Fig. 3.5 shows example data before and after applying a window function. In the case of a two dimensional Welch window, nearly three quarters of the data is discarded. Because of this, data windowing should only be done after first obtaining a diffusion estimate with the unwindowed data, and only if there is sufficient sampling that the correlation decay can still clearly be fit.

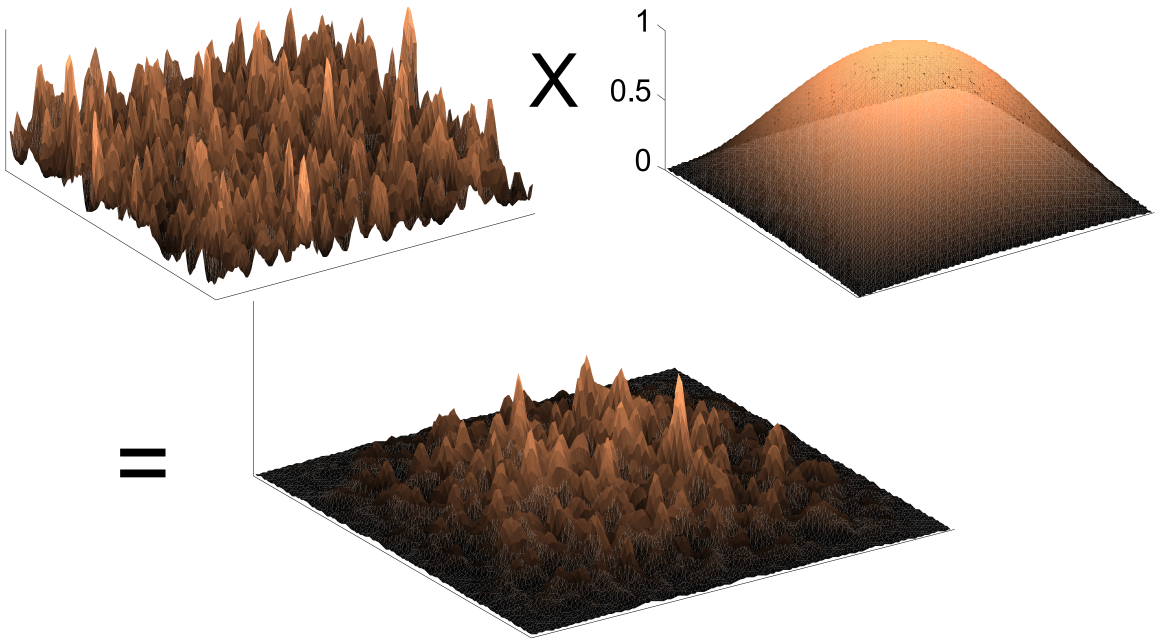

FIGURE 3.5: Image series can be multiplied by a 2D window function to correct for bias in kICS, but this discards a large fraction of the data. A simulated image is shown with intensity on the vertical axis (top left). This is multiplied by a Welch window function in two dimensions (top right), resulting in an image (bottom) that goes smoothly to zero at the edges.

It is important to know whether bias in kICS is purely dependent on the amount of spatial sampling, or whether other factors influence the bias. To determine this, we ran a variety of other simulations and analyses. First, we varied the temporal sampling, measured in number of correlation times, τ_D, by varying the number of images in a series. The simulated image series had open boundaries and the number of beam areas was kept constant. In Fig. 3.6 (A) we see that once a sufficient number of correlation decays are sampled, the bias remains constant as temporal sampling increases; however, it appears as if the bias is reduced when temporal sampling is low. This actually results from a second bias, a result of low temporal sampling, which offsets the bias due to spectral leakage in kICS. This second source of bias is a common phenomenon that affects both TICS [59] and FCS [79]. We confirmed that this bias also occurs in kICS by analyzing simulations with the same parameters as in Fig. 3.6 (A), but which had periodic boundaries and thus were not biased by spectral leakage. These results are shown in Fig. 3.6 (B). Consistent with findings by Kolin et al. for TICS [59], the bias due to finite temporal sampling becomes negligible once the image series is at least 10 τ_D in length.

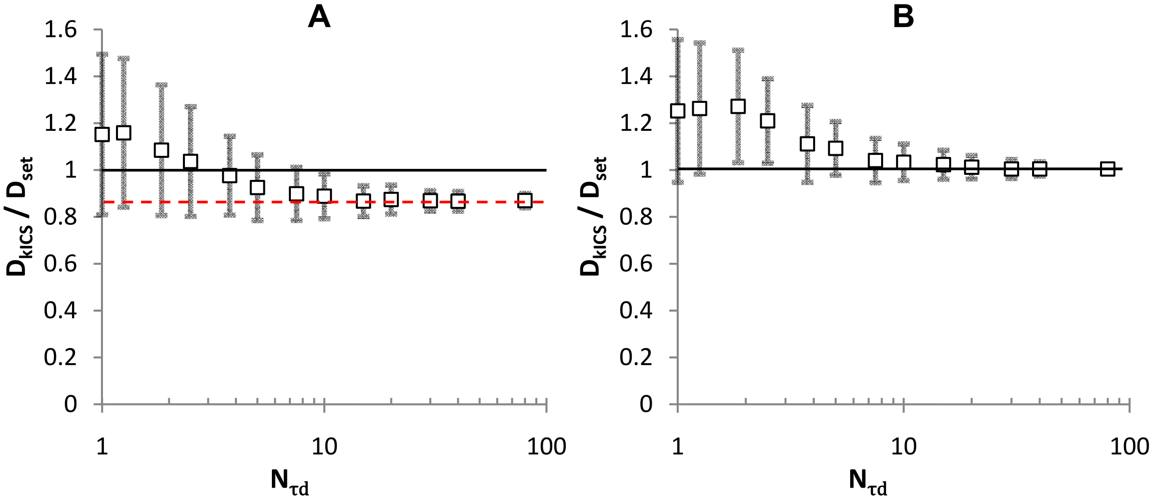

FIGURE 3.6: Spectral leakage bias in kICS is consistent at a given level of spatial sampling (number of beam areas), regardless of the temporal sampling in number of images or actual time. kICS was applied to simulated image series with a number of images that varied from 50 to 1600. Simulations for graph (A) had open boundaries, while simulations for graph (B) had periodic boundaries. When there are open boundaries as in (A) there can be bias due to both low temporal sampling (< ~10 τ_D) and low spatial sampling (limiting value of D recovered was on average 0.85 of the set value, i.e. biased 15% low). When boundaries are periodic, only bias due to low temporal sampling is observed. Other simulation parameters were kept constant: pixel dimensions were 64x64, PSF size 0.4 μm, pixel size 0.1 μm, set D=0.01 $\mu m^2/s$, time between frames 0.2 s; the number of beam areas was thus 81. Values shown are the average D / D_{set} from 200 simulations, and error bars are the $\sigma_D / D_{set.}$

Next, we ran simulations where the size of the PSF was varied but the image size remained fixed; thus, these image series had different numbers of beam areas but the same pixel dimensions. The results are shown in Fig. 3.7 (A), where it is clear that the kICS bias scales with the number of beam areas in a way similar to when the image size was varied (cf. Fig. 3.3). We also varied both the PSF and image size together, so that the same number of beam areas were sampled at a variety of image pixel dimensions. These results are shown in Fig. 3.7 (B), and in this case the bias remains approximately constant despite a changing image size, since the number of beam areas was fixed. Note that when the size of the PSF is varied, it is necessary to also vary the imaging frame rate and the $|\mathbf{k}|^2$ analysis cut-off accordingly. A larger PSF means that spatial resolution is reduced, and the $|\mathbf{k}|^2$ value at which the signal is lost in noise is also reduced. Also, with a larger PSF, fluctuations can only be sampled over larger spatial scales; since the mean diffusion distance scales with the square root of time, the simulated frame time must be increased as the square of the PSF size in order for particles to on average travel the same distance relative to the PSF size.

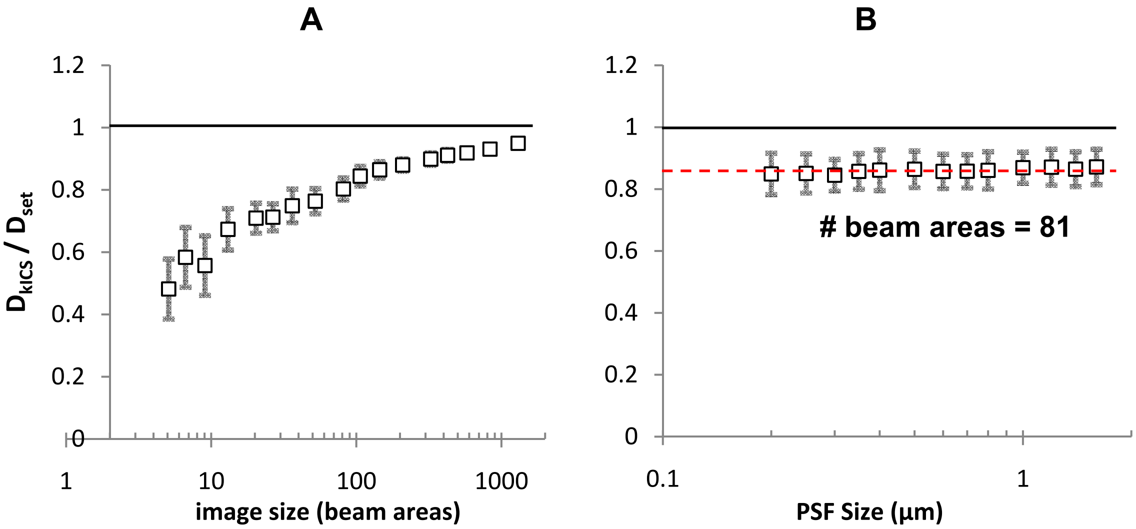

FIGURE 3.7: (A) Bias in kICS scales with the number of beam areas when the radius of the PSF is changed (from 0.2 to 3.2 μm) but image dimensions are kept constant (64x64 pixels). Values shown are the mean D / D_{set} recovered from kICS analysis of 200 simulations of particle diffusion, while error bars are σ_D / D_{set}. Image series had 400 images, and set D=0.01 μm^2/s; the image frame time was 0.4 s when the PSF was 0.4 μm, and varied as (PSF size / 0.4 μm)^2. (B) Bias in kICS is constant (~15% low) when the image size is scaled with changes in the PSF size so that the number of beam areas sampled remains constant. Values are the mean D / D_{set} from kICS analysis of 200 simulations of particle diffusion. Image series had 200 images, and the simulation timestep was varied as in (A), while the $|\mathbf{k}|^2$ cut-off varied inversely with the square of the PSF size.

Finally, we analyzed simulations using a range of data fitting parameters. As detailed in Sec. 2.2.1, in a kICS analysis different cut-off values for $|\mathbf{k}|^2$ and τ are possible. Using a set diffusion coefficient of D=0.01 μm^2/s we chose three pairs of $|\mathbf{k}|^2$ and τ cut-offs so that in each case the maximum expected correlation decay in a $|\mathbf{k}|^2$ plot would be $\ln[r(\mathbf{k},\tau) / r(\mathbf{k},0)] = -1.6$. As shown in Fig. 3.8 and in Table 3.1, the extent of the measurement bias differs slightly between the three cases. For the smaller image sizes in our simulations, from 32x32 to 48x48 pixels, it would not be possible to restrict the $|\mathbf{k}|^2$ cut-off further (below 20) while increasing the τ cut-off, as there would be fewer than four points to fit in the $|\mathbf{k}|^2$ plot. It also would not be appropriate to fit to higher $|\mathbf{k}|^2$ values while decreasing the τ cut-off, since the range of time lags covered would then be less than half of one correlation decay – i.e. on average a particle would move less than half of one beam radius (0.4 μm) at the maximum time lag. Thus, the range of cut-offs used in these simulations covers most of the reasonable range that could be used.

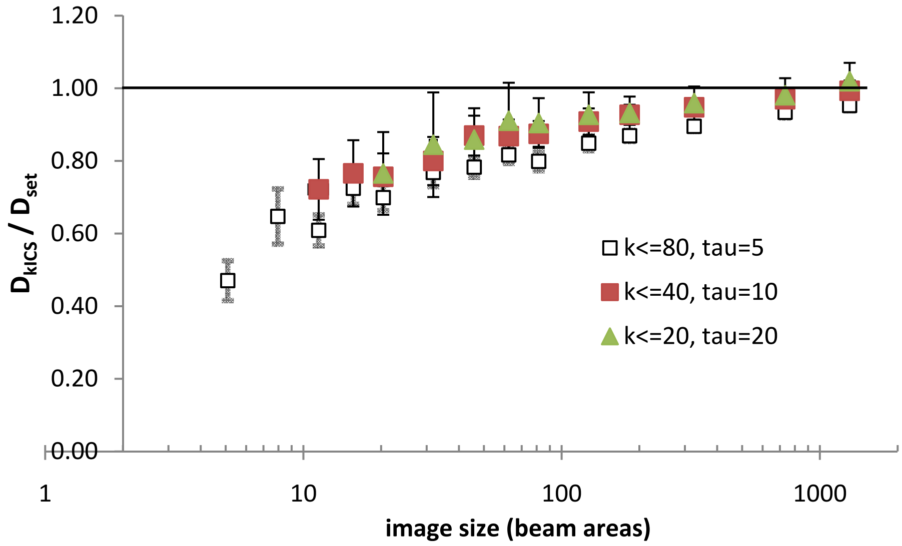

FIGURE 3.8: kICS bias differs only slightly when different data fitting settings are used. Values shown are the mean recovered D / D_{set} from 100 simulations, each of which had 500 images. The bias is slightly reduced when restricting the fit to lower $|\mathbf{k}|^2$ values (and thus fitting higher τ). However the uncertainty in the measurement increases, as seen in an increase in the size of the error bars. The smallest image sizes cannot be fit with a $|\mathbf{k}|^2$ cut-off lower than 80 since there would be too few points to fit in the $|\mathbf{k}|^2$ plot.

Although the bias in kICS due to spectral leakage is not completely independent of fitting parameters, the difference (~5%) is in all cases less than typical measurement uncertainty due to other factors (e.g. real differences due to the stochastic nature of diffusion, and differences between cells or regions sampled). Thus, a reasonable estimate of bias based on spatial sampling can still be made. Some kICS users may prefer a simple post-analysis correction over applying a window function that is, as we have shown, not completely effective. Table 3.1 shows the bias from the kICS results of Fig. 3.8 averaged over the different fitting parameters used. An unbiased estimate of the diffusion coefficient from a kICS analysis can be obtained by multiplying the kICS result by the inverse of this average bias; this correction factor is the last column in Table 3.1.

Image Size (beam areas)	Mean Relative D Recovered (for given cut-offs)				Mean D (for all cut-offs)	Correction factor
	k^2=80, τ=5	k^2=57, τ=7	k^2=40, τ=10	k^2=20, τ=20		
5	0.47				0.470	2.13
8	0.65	0.63			0.636	1.57
11	0.61	0.72	0.72		0.685	1.46
16	0.72	0.71	0.77		0.734	1.36
20	0.70	0.80	0.76	0.77	0.755	1.32
32	0.77	0.82	0.80	0.84	0.781	1.28
46	0.78	0.85	0.87	0.86	0.839	1.19
62	0.82	0.85	0.87	0.91	0.854	1.17
81	0.80	0.87	0.87	0.90	0.861	1.16
127	0.85	0.89	0.91	0.93	0.893	1.12
183	0.87	0.91	0.93	0.93	0.910	1.10
326	0.90	0.93	0.95	0.96	0.933	1.07
733	0.93	0.96	0.97	0.98	0.960	1.04
1304	0.95	0.98	0.99	1.02	0.986	1.01

TABLE 3.1: Correction factors for kICS diffusion measurements for image sizes of 1300 beam areas or smaller. Column 5 (“Mean D”) is the mean of columns 2 to 4, and so represents the relative bias expected for average fitting parameters at a given image size. A kICS diffusion measurement should be multiplied by the value in the last column, based on the spatial sampling in beam areas, to obtain an unbiased estimate of the diffusion coefficient.

The number of beam areas in an image can be determined easily, and requires no extra measurements. One first determines the PSF radius, ω_0, using ICS or a calibration measurement [43-44], and calculates the size of a beam area: BA = $\pi\omega_0^2$. The number of beam areas is the total image area divided by the beam area. This procedure is applied in Sec. 4.1 to correct bias in an experimental measurement of diffusing microspheres.

3.3 Recovery of Fast Diffusion Dynamics via kICS

A previous study found that the TICS analysis technique (introduced in Sec. 1.5.5) requires that at least two image frames are acquired per correlation time for results to be accurate [59]. In contrast, we found that kICS can recover accurate diffusion coefficients with image frame sampling at least ten times slower than this. To characterize this capability, we analyzed simulated image series of diffusing particles over a range of imaging frame rates using both kICS and TICS. These results are shown in Fig. 3.9. Simulated image series were 128x128 pixels with 100 total images, and the frame time was varied from 4 frames per τ_D to 0.05 frames per τ_D. A high level of noise was added to the image series: background white noise was added to give a signal:background of 3:1, and counting noise was added with WF=5. Rather than adjusting D to examine the effects of temporal sampling, we adjusted the imaging frame rate, which is equivalent for our simulated data. Note that while kICS results decrease in precision with fewer observations per correlation time, they remain centered around the set D value (i.e. accurate) over a wide range of frame rates, in contrast with TICS. Also, the precision from kICS analysis was better than for TICS in all cases. No photobleaching was

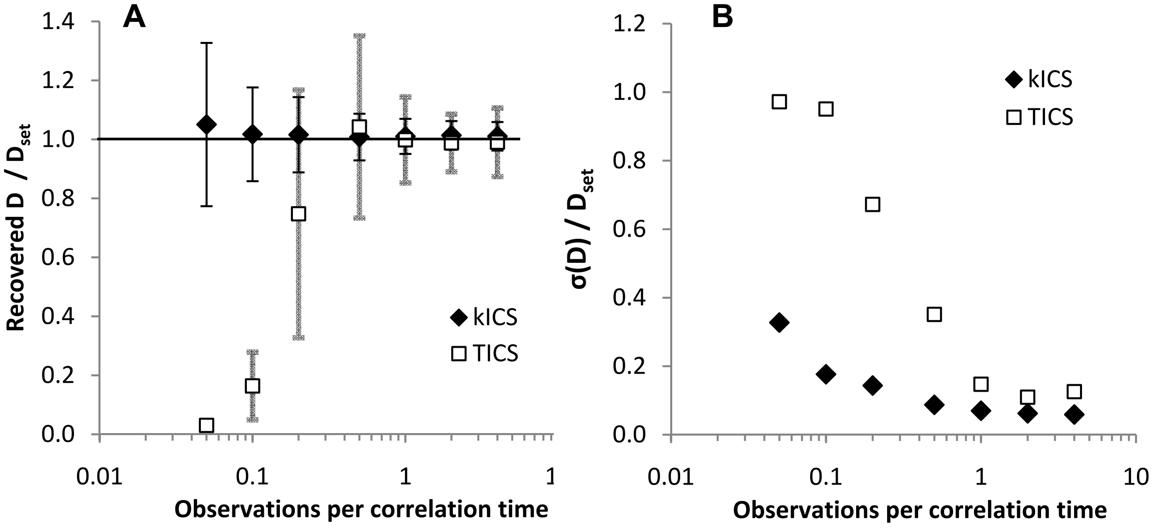

FIGURE 3.9: Error in kICS and TICS measurements of diffusion as a function of the sampling frequency. (A) Mean diffusion coefficients, relative to the set value, recovered by kICS and TICS analyses of 500 simulations of particle diffusion. Error bars are σ_D / D_{set}. (B) Root mean square deviation of the recovered diffusion coefficient from the set value, divided by the set value. kICS error is lower that TICS in all cases.

included in the simulations so that all factors apart from the frame rate would be optimal for TICS analysis. When photobleaching was included (50% of particles bleached over the 100 images of a series), kICS results were unaffected, whereas TICS results were biased, as previously reported [59], for all frame rates (data not shown).

Video rate imaging (30 Hz) is easily achieved with modern CCD cameras at an image size of 128x128 pixels (or larger). As shown in Fig. 3.9 (B), the relative standard deviation of kICS measurements is within 20% of the set value when the frame time is 10 τ_D or less. With an imaging frame time F = $10\tau_D$, the maximum 2D diffusion coefficient that can be accurately measured with video rate imaging can be calculated as follows:

$$D = \frac{\omega_0^2}{4\tau_D} = \frac{\omega_0^2}{4\left({}^{F}/_{10}\right)} \tag{3.10}$$

For the parameters used in our simulations (ω_0=0.4 μm), and with F = 33 ms (video rate), the maximum diffusion speed that can be accurately measured with kICS is ~12 $\mu m^2/s$. This is important since it encompasses the range of diffusion for membrane lipids (~1-10 $\mu m^2/s$) which diffuse more quickly than the larger embedded proteins.

Since the simulated image frame rate is slow relative to the diffusion of the point particles, we determined how kICS was able to measure the particle transport while TICS failed. Fig. 3.10 presents an intuitive explanation. The key is that in reciprocal space (k-space), small values of k correspond to large spatial scales in real space. Based on Eq. 2.13, decay of the correlation due to diffusion depends on the product of $|\mathbf{k}|^2$ and τ, and this decay can be fit to determine *D* so long as it remains above the noise level. We are free to choose the tradeoff between what values of $|\mathbf{k}|^2$ and τ to fit. By restricting the fit to low $|\mathbf{k}|^2$, we remain above the noise level and probe only correlation decay due to particle motion over relatively larger spatial scales. The conceptual equivalent in r-space would be to compute a pair correlation function for each possible pixel separation vector, which corresponds to the **k** vector in k-space.

The ability of kICS to measure relatively faster diffusion gives it a greater dynamic range than TICS. In addition, if an experimenter unknowingly chooses an imaging rate that is “too slow” based on the actual diffusion, kICS results will remain unbiased, providing the decay can be fit at all. This is also of interest as it relates to new super-resolution microscopy techniques. If TICS is used, then as the effective PSF of a point object becomes smaller, the correlation time decreases, and the imaging speed must be increased accordingly for results to remain accurate. With kICS, no such adjustments need to be made, and super-resolution further increases the dynamic range accessible with kICS analysis.

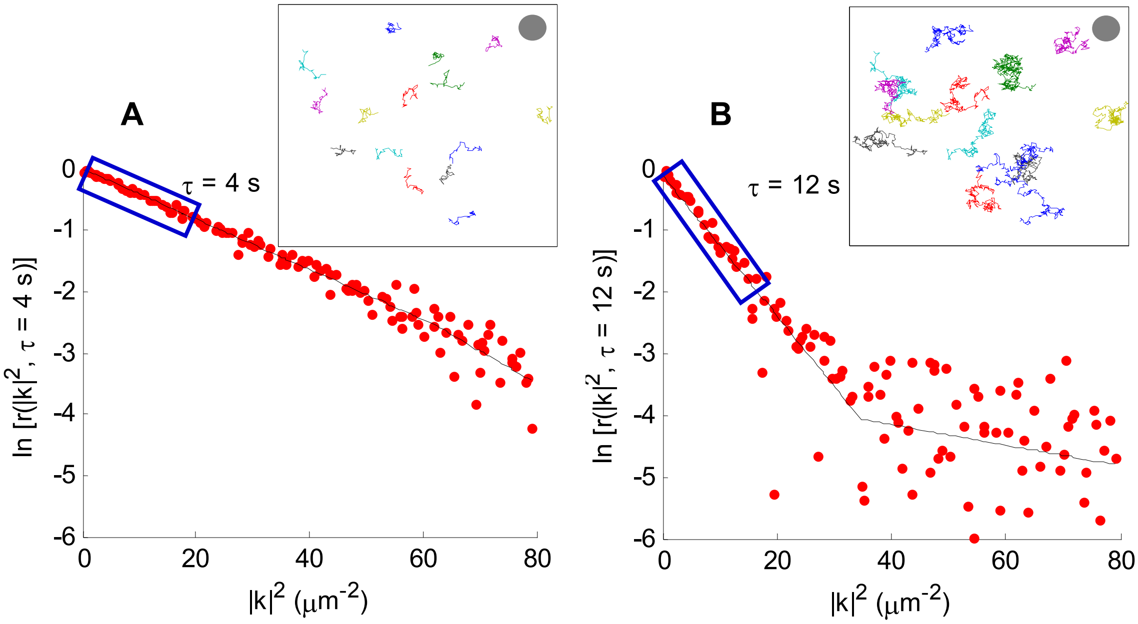

FIGURE 3.10: Restricting a kICS diffusion fit to low **k** values probes relatively longer distance correlations in real space. (A) When the imaging frame time is short relative to the diffusion speed, particles have moved a short distance between frames (inset, single particle tracks) and most (k_x,k_y) values remain above the noise in the |**k**|^2 plot. (B) When the frame time is long relative to the diffusion speed, particles have moved out of the beam area (size of grey circle) where they were found in the previous frame (inset), precluding use of TICS due to loss of correlation. However, low **k** values can still be fit in the |**k**|^2 plot, as shown by the regions boxed in blue.

Other techniques, such as FCS, FRAP, and RICS, can measure faster diffusion than kICS, which has an upper limit that depends on the imaging rate. FCS measures a single diffraction-limited spot in a cell or solution at μs binning rates, so it can be applied to very fast-diffusing particles such as cytosolic proteins. However, a specialized optical setup with an attached hardware autocorrelator is generally required, and no spatial information is acquired at the same time [84]. Unlike FCS, RICS is an image-based technique and thus gives spatial information, yet can still measure diffusion coefficients greater than 100 μm^2/s. However, RICS images must be acquired on a scanning laser microscope. Like other techniques based on correlation between image frames, kICS measurements are limited by the frame rate of the microscope. But unlike RICS, kICS can be applied to any microscope image series, including those acquired by epifluorescence, total internal reflection fluorescence (TIRF), wide-field structured illumination, or CLSM.

The Wohland group has recently proposed a new technique, imaging total internal reflection FCS (ITIR-FCS), as a highly parallel alternative to single-spot FCS, whereby a high-speed EMCCD camera collects images from a TIRF microscope to enable multiplexed FCS measurements [71]. This technique was initially used to compute time correlations within single pixels, as in TICS, but was later extended to perform cross-correlations in time between different regions of the image [70]. Because ITIR-FCS fits a time-dependent decay, it is subject to bias resulting from photobleaching, as was noted [70]. kICS can be applied to the same high-speed EMCCD-based image series to obtain diffusion coefficients or flow velocities but with no bias due to bleaching or blinking of particles.

3.4 Accuracy and Precision of kICS Measurements

Two key experimental parameters that determine whether kICS can reliably measure transport coefficients are the number of images in the series and the size of each image. The practical benefit to analyzing small image subregions of interest and shorter durations is that one could obtain a map of diffusion or flow that is spatially and temporally resolved in a cell. We wanted to determine the limits at which kICS would no longer be accurate as we reduced the size of the images and the number of frames sampled. We therefore simulated image series with a range of sizes and numbers of frames and analyzed them with kICS. We used challenging simulated imaging conditions: in all cases background noise was added to effect an average S/B of 3, counting noise was added with WF=5, and mono-exponential photobleaching was included so that half of the particles were bleached over the image series (regardless of how many images were in the series). At this high level of noise and high particle density, correlations in image structure are difficult to discern visually (see Fig. 3.11 (B)).

Fig. 3.11 shows the relative standard deviation of 200 simulations and kICS analyses at each combination of image size and number of τ_D sampled. Rather than plotting the number of image frames on the *x* axis, we plot the number of τ_D sampled, as this is a better measure of the amount of temporal sampling (assuming that the frame rate chosen is reasonable). All simulations were "open volume" so that particles could exit from the edges of the image, and a post-analysis correction was applied based on the number of beam areas as described earlier. Corrected measurements using kICS remained accurate within error regardless of the spatial and temporal sampling, and thus the results in Fig. 3.11 indicate the relative precision of the measurements.

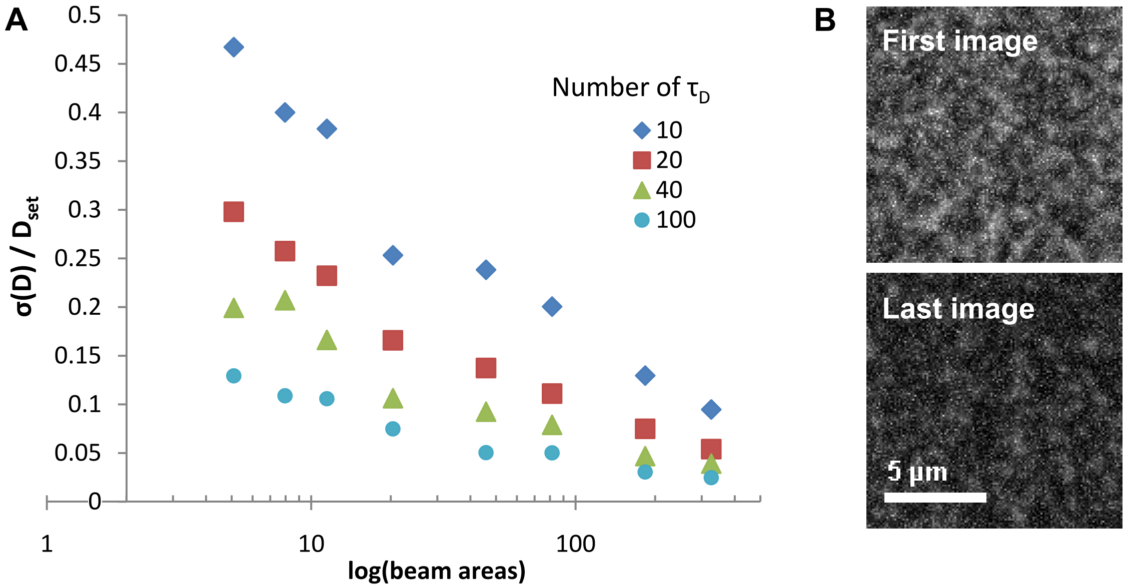

FIGURE 3.11: (A) Relative standard deviations of diffusion coefficients recovered by kICS over a range of simulated image sizes and number of τ_D sampled. Simulations for images larger than 30 beam areas had a frame rate of 4 frames per τ_D (total number of images was thus 40, 80, 160, and 400). So that there were enough points to fit in the $|\mathbf{k}|^2$ plots, simulated images smaller than 30 beam areas had a frame rate of 8 frames per τ_D (total number of images was thus 80, 160, 320, and 800). (B) Example of first and last images from one of the simulated image series.

Measurements had a standard deviation of about 20% from the set value for images with 20 beam areas and which sampled 20 τ_D, or for images of just 5 beam areas which sampled 100 τ_D. With image correlation techniques it is often possible to trade off temporal sampling with spatial sampling to achieve results with equivalent precision. This is largely true in kICS, although we find that increasing temporal sampling has a stronger effect than spatial sampling. For example, analyzing image series of 5 beam areas and 100 τ_D gave more precise results than image series sixteen times larger (80 beam areas) but with ten times less temporal sampling (10 τ_D). Knowing the measurement precision is important if one wishes to compare different measurements, such as from different cell regions, or before and after a treatment; when individual measurements are not sufficiently precise, differences cannot be distinguished. Fig. 3.11 can be used to determine the minimum sampling needed for a desired level of measurement precision. In general, of course, one will not know the diffusion coefficient before the measurement. In this case, one can only guess a reasonable value or range for the diffusion coefficient and choose an imaging frame rate that gives sufficient temporal sampling. Once a first measurement is obtained, it is then possible to determine the approximate number of τ_D that would be sampled when a given number of images are collected, and estimate what measurement precision should be achievable.

3.5 Nonuniform Particle Distributions

One of the strengths of FCS, and by extension most image correlation techniques, is that they are applied to systems at equilibrium or steady state and no external perturbation is needed to measure the quantity of interest. However, in some cases one desires to introduce a local perturbation, such as by photouncaging an effector molecule at a specific location [85], and it is now possible to trigger fluorescence simultaneously with photouncaging [80-82]. The assumption of a random, Poisson distribution of particles in space underlies the theory of FCS and TICS, and measurements are biased when this assumption breaks down. We found that kICS, however, can accurately measure particle diffusion even with highly localized initial particle distributions if the correlation function is normalized. We simulated three kinds of image series: 1) all particles initially located at the center of the image, and 2) all particles initially located in a vertical strip 1 μm wide, and 3) clusters of particles (20 particles per cluster) that would appear at random times and places. This last scenario could model vesicle fusion with a membrane and fluorescent protein or lipid release into the membrane. In each case, particles diffused randomly from their initial positions in the image series over a time span of 30 τ_D. As can be seen in Fig. 3.12, the particle distributions remained nonuniform throughout the image series. With kICS, the set diffusion coefficient was recovered within error in all cases; in contrast, TICS measurements were systematically biased (Fig. 3.13).

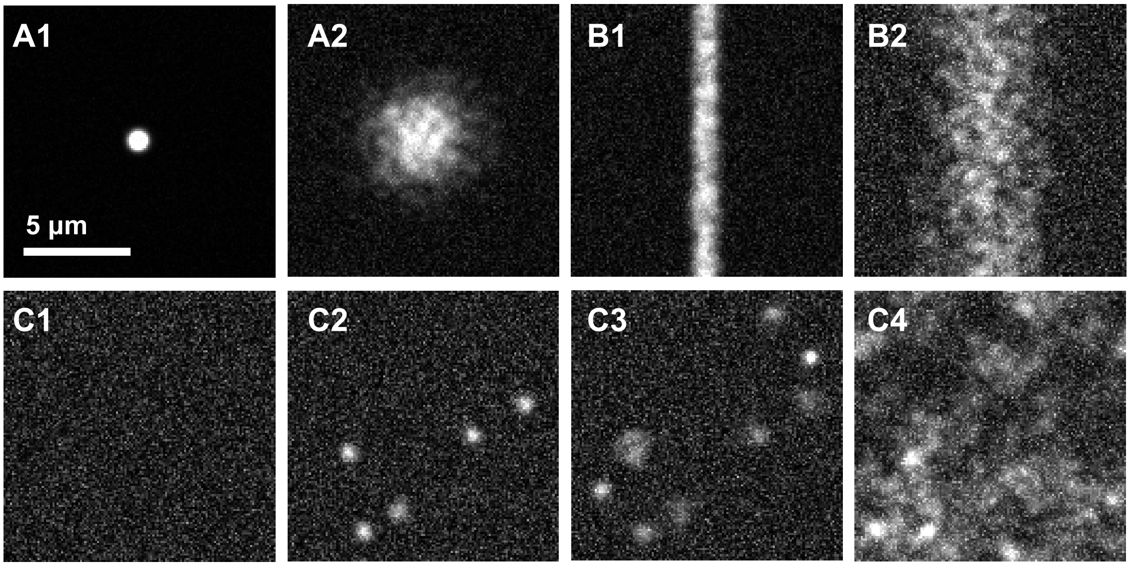

FIGURE 3.12: Example images from simulations with nonuniform initial particle distributions. (A1, A2) First and last images from series with all particles initially located at the image center. (B1, B2) First and last images from series with particles initially located in a vertical strip 1 µm wide. (C1 – C4) Images 1, 10, 25, and last image from series with particle clusters that would appear at a random point and then diffuse in 2D. All image series were 20 τ_D in length, 128x128 pixels, and had other parameters (including noise) at default levels described earlier.

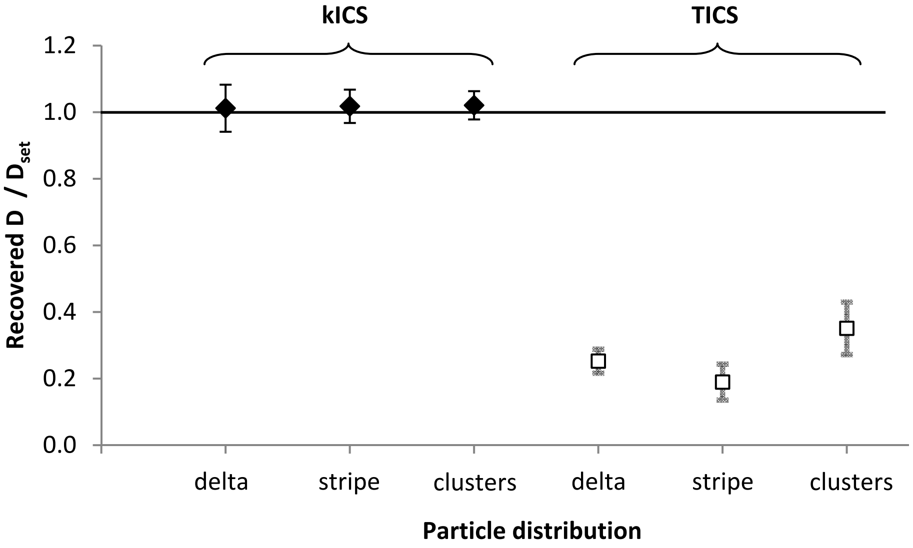

FIGURE 3.13: Mean diffusion coefficients, relative to the set value, recovered by kICS and TICS analyses of simulated diffusion with nonuniform initial particle distributions. Error bars are the standard deviation from 500 simulations and analyses. kICS results remained accurate, whereas TICS results were strongly biased.

Some caveats should be noted to ensure that kICS can be effectively applied in these scenarios. Although the initial distribution of particles was nonuniform, it is important that they subsequently diffused freely. Also, to obtain accurate diffusion measurements with kICS under these conditions, one must normalize the kICS correlation function by its value at zero time lags, as in Eq. 2.13. Frames in which a significant number of pixels are saturated should be excluded from the diffusion analysis. Finally, the time series must still sample a sufficient number of correlation times to place it in a non-biased regime (i.e. at least 10 τ_D).

3.6 Estimating kICS Measurement Uncertainty

The uncertainty (or conversely, the precision) associated with an experimental measurement informs us of the confidence we can have that the measured value is close to the true value, assuming there is no systematic bias (i.e. measurements are accurate). The best way to determine measurement uncertainty is to repeat the measurement a number of times. The standard error of these independent measurements can be reported, or can be used to determine specific confidence bounds. In some cases, however, it is not possible to repeat a measurement multiple times. Alternatively, it may be desirable to estimate the measurement uncertainty associated solely with our method of analysis.

In this section, we propose a simple method to estimate the uncertainty associated with a single kICS diffusion measurement. When applying kICS there is some subjectivity in deciding what $|\mathbf{k}|^2$ and τ cut-offs are optimal, such that kICS analyses performed on the same image series by different experimenters will return different results. Thus, the uncertainty associated with a kICS analysis itself can be estimated by running the analysis multiple times, and using different $|\mathbf{k}|^2$ and τ cut-offs each time. We illustrate this approach by estimating the uncertainty from three kICS analyses of a single image series using different $|\mathbf{k}|^2$ and τ cut-offs. These analyses are summarized in Fig. 3.14. In each case the cut-offs are adjusted so that the maximum expected correlation decay is the same. If possible, one should do analyses with more than three sets of different fitting parameters, using maximum τ cut-offs both above and below the analysis that best fits the data. The standard deviation of diffusion coefficients recovered from

Analysis 1: max $|k|^2$ = 100, max τ = 4 frames (1.6 s)

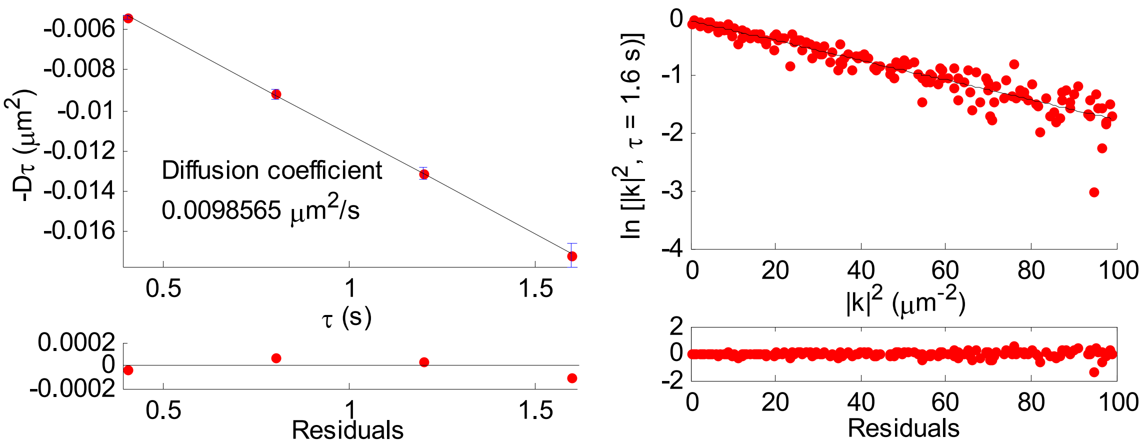

Analysis 2: max $|k|^2$ = 50, max τ = 8 frames (3.2 s)

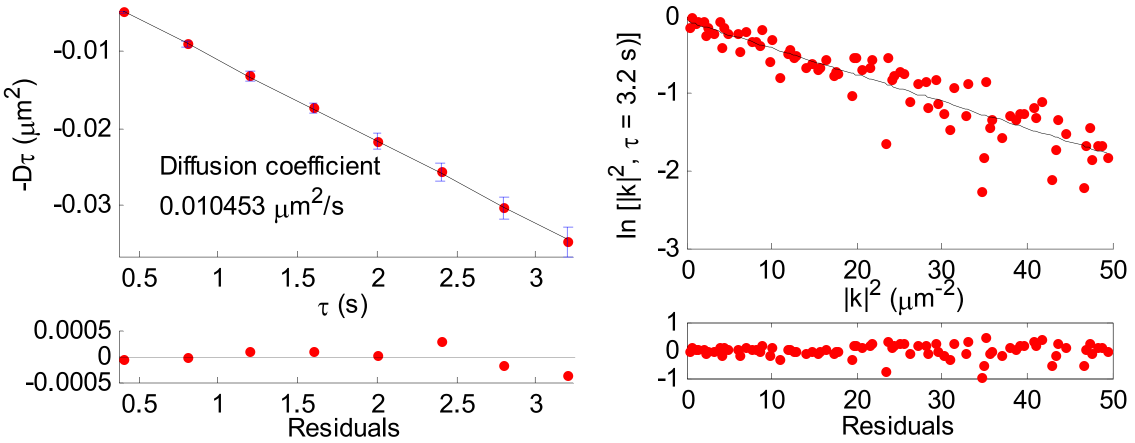

Analysis 3: max $|k|^2$ = 20, max τ = 20 frames (8 s)

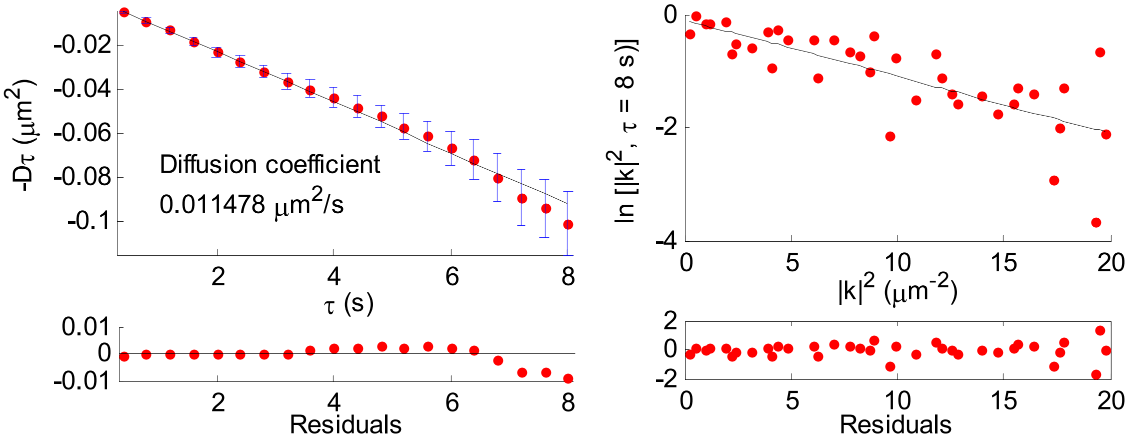

FIGURE 3.14: Three kICS analyses, using different $|\mathbf{k}|^2$ and τ cut-offs, of the same image series of simulated particle diffusion with set D=0.01 μm^2/s. The standard deviation of diffusion coefficients recovered from these analyses is an estimate of uncertainty in the kICS diffusion measurement.

these analyses is an estimate of the measurement uncertainty. For the example of Fig. 3.14, the reported diffusion coefficient measurement would be the central analysis value, 0.0105 $\mu m^2/s$ (vs. set value of 0.0100 $\mu m^2/s$), and the uncertainty would be 0.0008 $\mu m^2/s$ (the standard deviation of the three values in Fig. 3.14). This method of uncertainty estimation is applied in Sec. 4.2 when measuring the diffusion coefficient of QD-labeled membrane molecules from single image time series.

In computer simulations, a number of assumptions are made that may not hold true in actual experiments. Other sources of uncertainty will contribute to the variability in repeated independent measurements, such as variability in the underlying biological dynamics, deviations from ideal behaviour (i.e. particle interactions), or the presence of multiple populations with different diffusion dynamics. Some of these sources of variability will widen the variability of kICS results when fitting with different $|\mathbf{k}|^2$ and τ cut-offs. For example, the presence of multiple populations with different diffusion coefficients will cause curvature in $|\mathbf{k}|^2$ plots, and thus the measurement can differ depending on what $|\mathbf{k}|^2$ cut-off is used. With kICS it is possible to fit the correlation decay with a two-population model to determine the fraction of each population and their diffusion coefficients. However, this can no longer be done with a linear fit of the log-transformed correlation in a $|\mathbf{k}|^2$ plot; instead, a non-linear fit to the untransformed correlation must be done. Such a non-linear fit is more sensitive to noise, and is unreliable when one population is a small fraction of the other. Moreover, the experimenter may not be aware that multiple populations exist. Regardless, the smaller population will modify the $|\mathbf{k}|^2$ plots at least slightly, and this will increase the dependence of the measurement on the cut-offs used.

Fig. 3.15 shows an example of both the untransformed correlation and the log-transformed correlation ($|\mathbf{k}|^2$ plot) for a kICS analysis of simulated diffusion where there are actually two diffusing populations with fractions of 20% and 80%. The smaller population diffuses ten times faster than the larger one. Fig. 3.16 shows kICS analyses of the same simulation fit to a single population model. When the cut-offs are $|\mathbf{k}|^2=50$ and $\tau=8$, the diffusion coefficient reported is 0.0092 $\mu m^2/s$, lower than that of either population. When a lower $|\mathbf{k}|^2$ cut-off is used, a considerably higher diffusion coefficient measurement of 0.0122 $\mu m^2/s$ is obtained. Thus, the variability in kICS analyses using

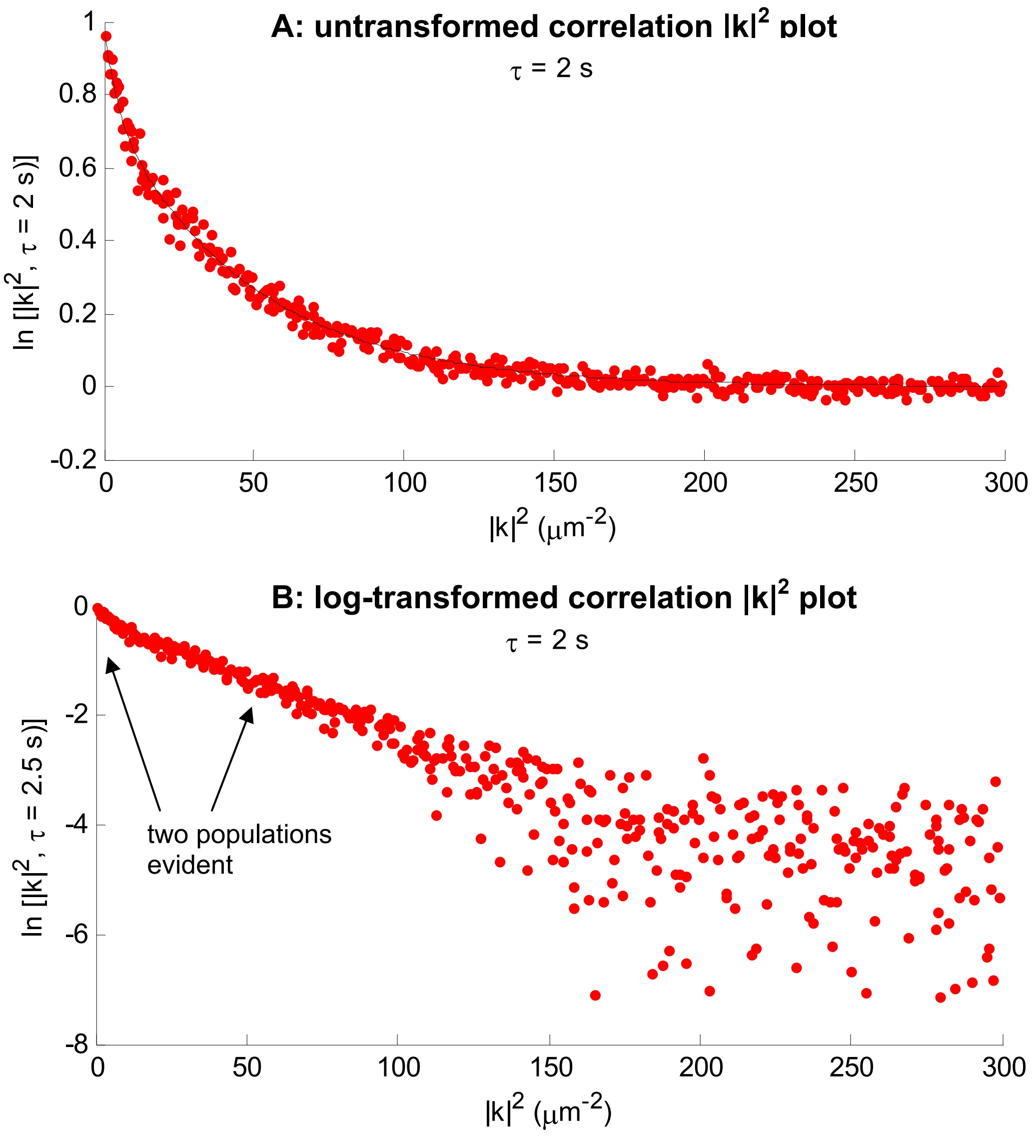

FIGURE 3.15: kICS analysis of simulated particle diffusion where there are two populations in a ratio of 8:2. (A) The untransformed correlation function $|\mathbf{k}|^2$ plot. (B) The log-transformed correlation function $|\mathbf{k}|^2$ plot. The larger population had set D=0.01 μm^2/s, and the smaller population had D=0.1 μm^2/s. Plot (A) has a bi-exponential decay that can be fit to extract two diffusion coefficients. Plot (B) is what one would see in a normal (log-transformed) $|\mathbf{k}|^2$ plot. The slope at low $|\mathbf{k}|^2$ is somewhat greater than the slope at higher $|\mathbf{k}|^2$.

different cut-offs can reveal not only uncertainty arising from the analysis itself, but also variability in the measured dynamics, such as the presence of multiple populations of diffusing species.

Analysis 1: max $|k|^2$ = 50, max τ = 8 frames (3.2 s)

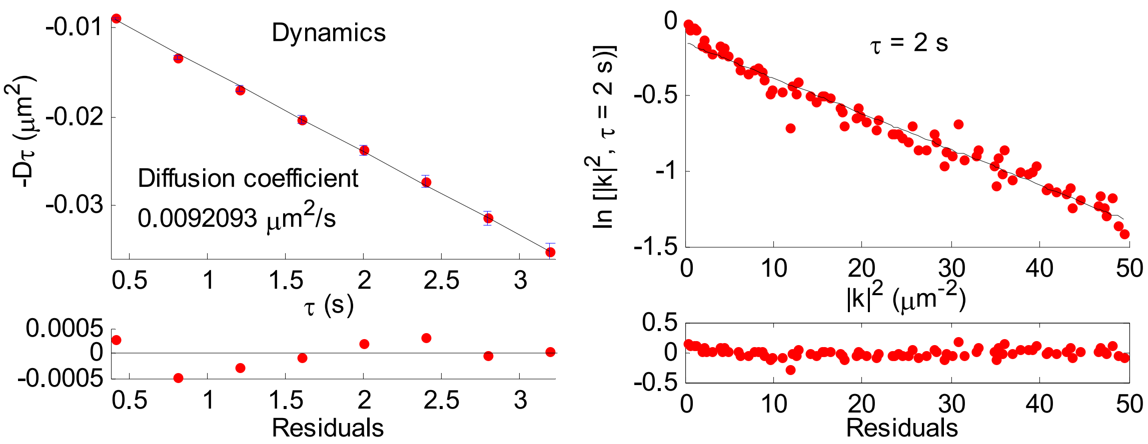

Analysis 2: max $|k|^2$ = 10, max τ = 20 frames (8 s)

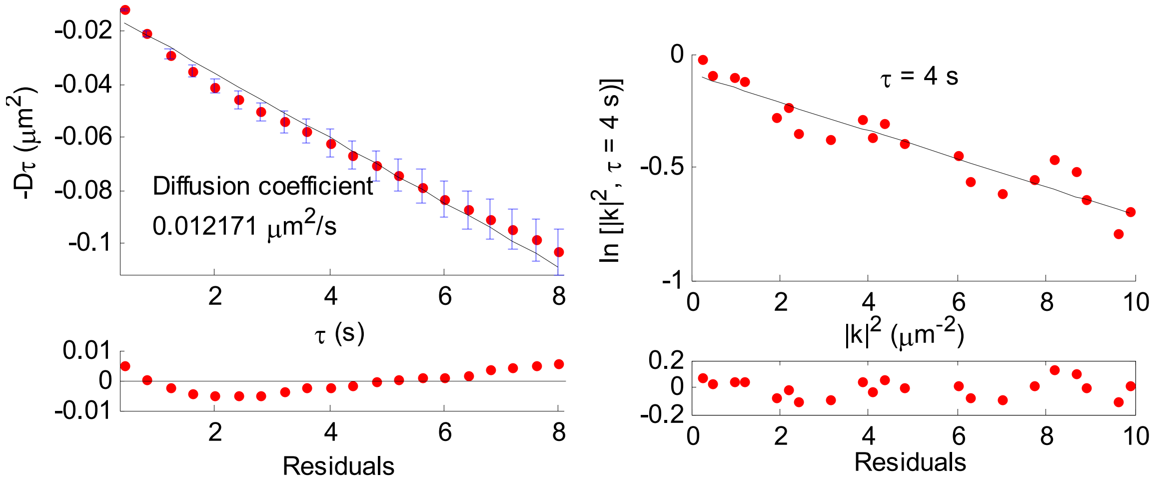

FIGURE 3.16: Two kICS analyses, using different $|\mathbf{k}|^2$ and τ cut-offs, of simulated particle diffusion where there are two populations in a ratio of 8:2. The larger population had set D=0.01 μm²/s, and the smaller population had D=0.1 μm²/s. When a lower $|\mathbf{k}|^2$ cut-off is used (bottom row) the diffusion measurement is considerably higher than with a higher cut-off. In analysis 1 (top row) it can be seen that the $|\mathbf{k}|^2$ plot is slightly curved. In analysis 2, the dynamics plot is curved. In this case, no single set of fitting parameters will result in perfect residuals of the linear regressions.

In this chapter we investigated the accuracy and precision of kICS under a variety of scenarios using computer simulations. In the next chapter we apply kICS to experimental data to verify that the discoveries made via simulations are relevant to real situations.

4. k-Space Image Correlation Spectroscopy Applied to Microspheres and Live Cells

In Chapter 3, we applied kICS to computer-simulated image series, and through these investigations we discovered both the capabilities and limitations in applying kICS. However, real systems rarely behave as ideally as the equations we use to model them. Particles can have attractive or repulsive interactions that modify their diffusive behaviour; detectors can exhibit nonlinear response or introduce undesired correlations; noise may not be ideal and could be correlated between image frames. Moreover, cells are living systems that are far from chemical equilibrium, and their responses to imaging conditions or experimental treatments can change during the course of a measurement.

In this chapter we apply kICS to experimental data to verify that the discoveries made via simulations *in silico* are valid.

4.1 Measuring Diffusing Microspheres

When image boundaries are open, kICS measurements of diffusion have a bias that depends on the size of the region analyzed. In Sec. 3.2 we used simulations to determine correction factors that can be applied to obtain unbiased measurements for any image size. To confirm that bias in kICS diffusion measurements can be corrected in real experiments, we imaged 0.105 μm fluorescent microspheres diffusing in a sucrose solution of known concentration on a CLSM. We then determined how the kICS measurement of D differed depending on the size of the subregions analyzed.

4.1.1 Microsphere Sample Preparation and Confocal Imaging

An aqueous solution of 800 g/L sucrose (Sigma-Aldrich, Oakville, Ontario, Canada) was prepared in milliQ distilled water. A stock solution of microspheres (carboxylate coated, radius 0.105 ± 0.005 μm, excitation/emission maxima of 505/515 nm, obtained from Invitrogen, Burlington, ON) was sonicated for 15 min before use, and then 2 μL of this stock solution was added to 198 μL sucrose solution. The diluted microspheres were sonicated for an additional 15 min, and then pipetted into the cavity of a glass-bottomed Petri dish (No. 1.5; MatTek, Ashland, MA) for imaging. The cavity was sealed with a coverslip.

Samples were imaged in a temperature-controlled chamber at 21°C with an Olympus FV300 IX71 CLSM (Olympus, Melville, NY), using the 488 nm laser line of an Ar^+ laser for excitation. Fluorescence was collected by a 60X PlanApo oil immersion objective (NA 1.4) using a 488 nm bandpass dichroic in combination with a BA510IF long-pass filter (Chroma, Rockingham, VT). The PMT was adjusted such that no pixels were saturated, and no thresholding was applied. Two imaging settings were used: (A) 128x128 pixels with a frame time of 0.247 s and a pixel size of 0.09207 µm, and (B) 320x240 pixels with a frame time of 0.457 s and a pixel size of 0.2778 µm, referred to hereafter as image series A and B. We collected 2000 images so that the kICS analysis would not be limited by temporal sampling, and to ensure that sufficient signal would exist even when small image regions (e.g. 16x16 pixels) were analyzed. Fig. 4.1 presents example images from these series.

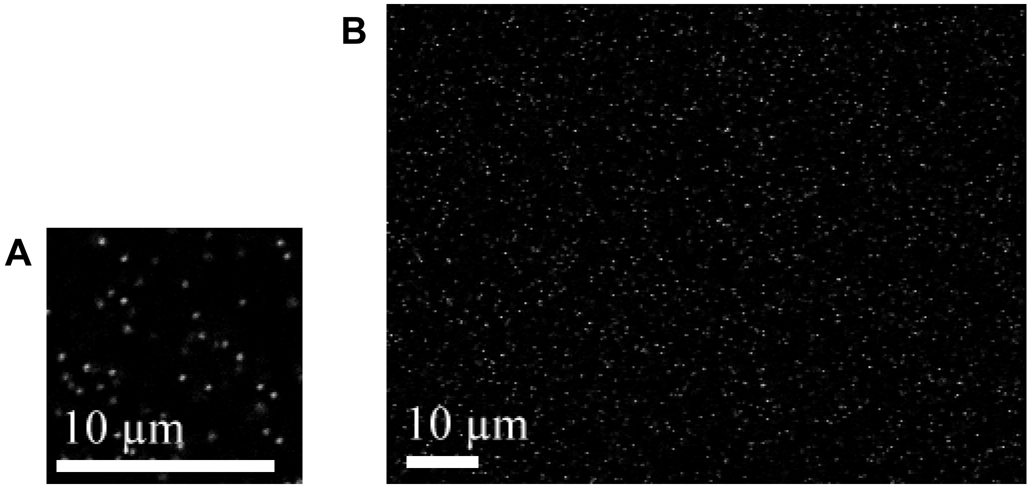

FIGURE 4.1: CLSM images of fluorescent microspheres diffusing in sucrose solution. (A) A 128x128 pixel image with pixel size 0.09207 µm. (B) A 320x240 image with pixel size 0.2778 µm.

4.1.2 kICS Analysis

We used spatial ICS [44] to determine the e^{-2} radius of the PSF for image series A with pixel size of 0.09207 μm, which was $\omega_0 = 0.223 \pm 0.013$ μm. This enabled us to calculate the number of beam areas for any subregion of the image. We assumed the same PSF radius for image series B since ICS cannot reliably be applied when the pixel size (0.2778 μm) is larger than the PSF size, and the same CLSM optics were used for both series. There were two reasons for using a larger pixel size for image series B. First, since the image is larger it takes longer to scan, and the maximum frame rate is slower. With a larger pixel size, the particle residency time within a pixel is longer, and this enabled accurate kICS measurements with small subregion sizes. Second, using a different pixel size provides another test of the effectiveness of the correction we apply based on the size of a subregion in number of beam areas.

We next applied kICS to the full data set of each image series to determine reference measurements for the diffusion coefficients of the samples. Image series B covered an area of over 37,000 beam areas, and so the measured value D=0.0618 $\mu m^2/s$ did not have to be corrected for low spatial sampling bias. Image series A covered an area of only 889 beam areas, and so the diffusion measurement from the full image was itself corrected (upwards by ~3%) according to the correction factors in Table 3.1 to obtain a reference value D=0.0590 $\mu m^2/s$. This agrees well with the measurement from image series B, which is expected since the same sample was imaged. Temperature fluctuations will lead to changes in the viscosity of the solution and can be expected to cause minor variations in experimentally measured diffusion.

We next split the image series into square subregions of different sizes, which ranged from ~14 to 7000 beam areas, and reanalyzed the subregions. Fig. 4.2 shows the mean diffusion coefficients recovered for these subregions, where it is clear that uncorrected kICS measurements are biased low for small image regions.

We then applied a bias correction based on Table 3.1; since the number of beam areas was generally in between those in the table listings, we linearly interpolated a correction value between the nearest two rows. With this correction, the results from the subregions agree well with the reference measurements made using the full-size image series. These results are summarized in more detail in Table 4.1.

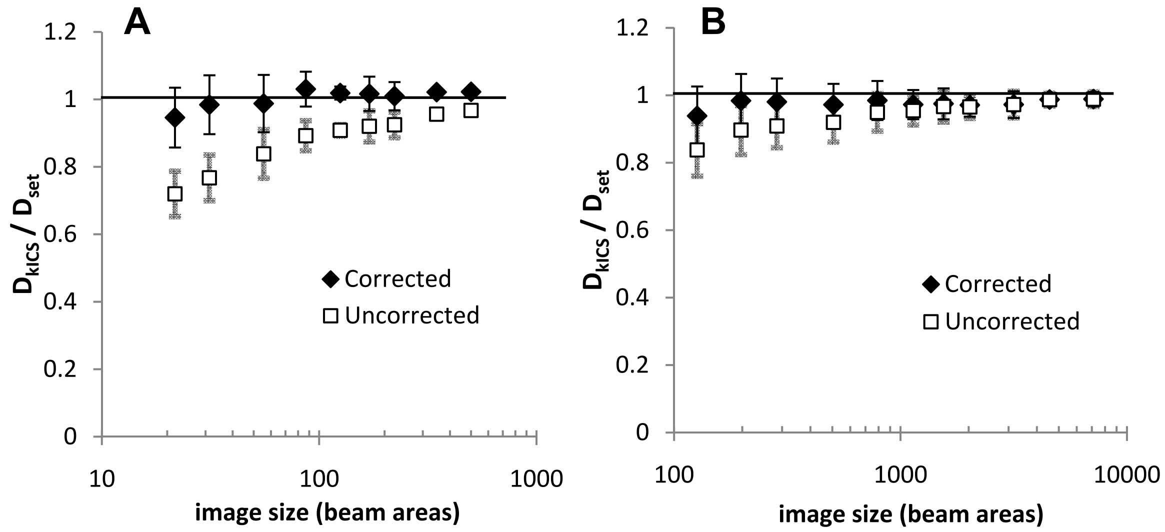

FIGURE 4.2: Post-analysis correction of kICS bias for differently sized regions in samples of diffusing fluorescent microspheres. Samples A and B are shown, as described in the text. As in simulations, uncorrected values (squares, □) are biased low for small image sizes. Applying the correction factors from Table 1 gives values (diamonds, ♦) that agree well with the reference diffusion measurement for the entire sample.

	Image Series A				**Image Series B**			
Region size (px)	**# Beam Areas**	**Mean D/D_{ref}**	**Corr factor**	**Corrected D/D_{ref}**	**# Beam Areas**	**Mean D/D_{ref}**	**Corr factor**	**Corrected D/D_{ref}**
16	-	-	-	-	126	0.838	1.120	0.939
20	21.7	0.720	1.314	0.946	198	0.897	1.097	0.984
24	31.3	0.767	1.282	0.984	284	0.909	1.079	0.981
32	55.6	0.838	1.178	0.988	506	0.920	1.057	0.972
40	86.8	0.892	1.155	1.031	790	0.950	1.037	0.985
48	125	0.908	1.122	1.019	1138	0.955	1.019	0.972
56	170	0.920	1.105	1.017	1549	0.967	1.009	0.975
64	222	0.925	1.092	1.010	2023	0.965	1.006	0.971
80	347	0.956	1.068	1.022	3161	0.973	1	0.973
96	500	0.967	1.057	1.022	4552	0.987	1	0.987
120	781	0.962	1.037	0.998	7112	0.989	1	0.989
128	889	0.969	1.032	1.000	-	-	-	-

TABLE 4.1: Mean corrected and uncorrected diffusion coefficients measured for differently sized subregions of image series A and B, shown as values relative to the reference diffusion coefficients for the samples.

We also determined the effectiveness of applying a Welch window function to the subregions of image series A and B before kICS analysis. In this case, no correction factor is applied to the recovered diffusion coefficient. As seen in Fig. 4.3, this method of correction was fairly effective for image series B, but less so for series A, which had fewer beam areas. We speculate that this could occur because two dimensional data windowing discards around three quarters of the data; for small images this may mean that some of the $|\mathbf{k}|^2$ values fit have very little sampling despite the length of the image series.

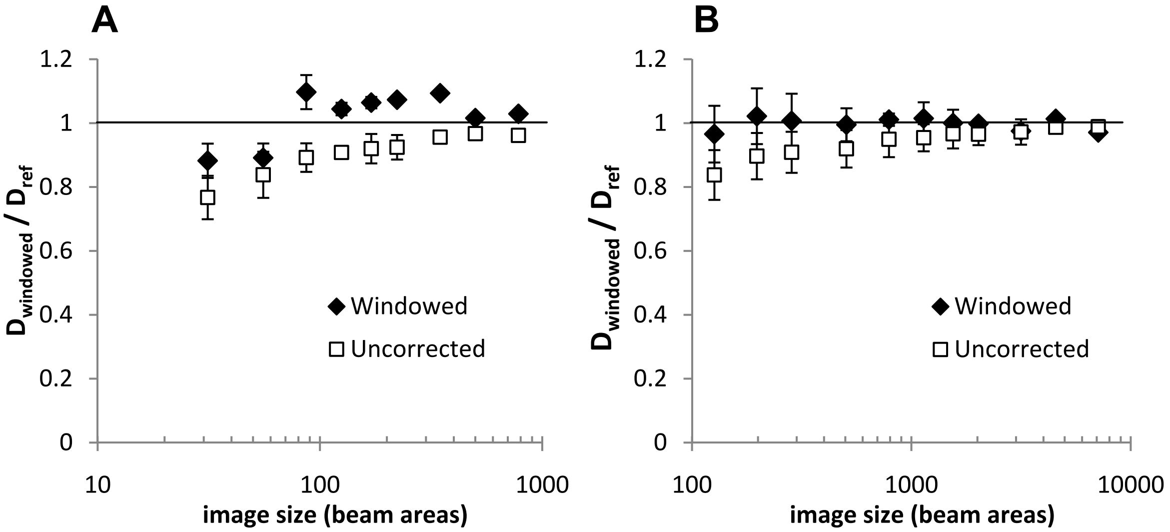

FIGURE 4.3: Correction of kICS bias by data windowing for differently sized regions in samples of diffusing fluorescent microspheres. Samples A and B are shown, as described in the text.

Although bias in diffusion measurements can be seen as a drawback of using kICS, in practice even relatively small image regions suffer from only minor bias, which can be easily corrected. As a typical example, an image of 40 by 40 pixels with a pixel size of 0.1 μm and a PSF radius of 0.25 μm contains 80 beam areas and is biased by around 15%. If super-resolution imaging methods such as stimulated emission depletion microscopy (STED) [32] or structured illumination microscopy [86] are used, the number of effective beam areas increases and the bias in measuring small image regions decreases.

4.2 Measuring Diffusion in Live Cells with Quantum Dot Labels

One of the primary advantages of kICS over other fluorescence correlation techniques is that kICS is unbiased by blinking or bleaching of the fluorophore labels. This presents a unique opportunity to use kICS in conjunction with QDs, whose fluorescence is very bright but whose emission is also intermittent. QDs are also especially suitable for multicolour labeling because their emission spectra are narrow, which enables splitting the signals from different colours of QDs in a single sample based on their emission wavelengths. As described in Sec. 1.5.3, QDs are thus often used as labels for single particle tracking of membrane proteins. However, even when the requirements of an SPT experiment are met, i.e. a high signal-to-noise ratio and low labeling density are achieved, SPT analysis can be time-consuming. This is due to the fact that SPT is computationally intensive, requiring nonlinear curve fitting to locate the center of fluorescence emission for each particle in each image frame, followed by linking of particle positions into trajectories. Statistical criteria typically need to be used to discriminate true particles from accidental detections and to link trajectories accurately [87]. These multiple steps often require manual checking of the trajectories mapped. It would thus be useful to have a complementary technique that is faster to perform, but that gives comparable and accurate measurements of the ensemble dynamics for comparison with the single molecule results.

In this section, we compare the use of kICS and SPT to analyze diffusion in the cell membrane. Specifically, we labeled three different membrane species with QDs of different colours and imaged them simultaneously in live cells. The membrane species were the sphingolipid GM1 labeled with 705 nm-emission QDs, a lipid-anchored acyl carrier protein, ACP-GPI, labeled with 655 nm-emission QDs, and a biotin ligase acceptor peptide fusion with the epidermal growth factor receptor protein (BLAP-EGFR) labeled with 605 nm-emission QDs. All cell culture, labeling, imaging and SPT work was done by collaborators Eva Arnspang Christensen and Mathias Clausen in the lab of Prof. Christoffer Lagerholm at the MEMPHYS Center for Biomembrane Physics, University of Southern Denmark, Odense, Denmark. These results are thus presented in sufficient detail to ensure the SPT data is clear. I performed all kICS analyses described below.

4.2.1 Methods

Cell Culture, Transfection and Labeling

Mouse embryonic fibroblasts (MEFs) were grown in a humidified atmosphere at 37 °C, using Dulbecco's modified eagle's medium (DMEM) with standard concentrations of glutamate (Gibco), penicillin-streptomycin (Sigma) and 10% fetal bovine serum (Sigma). For transfection and imaging, cells were seeded on No. 1.5 glass coverslips in 6-well plates at a density of 25,000 cells per well and were transfected at 24 h and imaged within the next 24-48 hours.

Addition of the proteins epidermal growth factor receptor (EGFR) tagged with biotin ligase acceptor peptide (BLAP) and acyl carrier protein glucosylphosphatidylinositol (ACP-GPI) fusion protein (Covalys) to MEF cells was done by co-transfection of four DNA plasmids, BirA-KDEL (1 μg), BLAP-EGFR (1 μg), ACP-GPI (1 μg), and a plasma membrane fluorescent protein marker, K-Ras2-YFP (0.25 μg, ATCC plasmid 10089283) per 25,000 cells. Transfections were done using JetPEI (Polyplus transfection) at the recommended 2:1 (v/w) ratio to the DNA. Transfected cells were grown overnight in 10 μM biotin to enable specific biotinylation of BLAP-EGFR by co-expressed BirA-KDEL plasmid as has been described [88].

For orthogonal three QD color labeling, we performed the labeling in two steps. First, we labeled the ACP-GPI fusion protein with custom conjugated coenzyme A (CoA) QDs (peak emission 655 nm). Cells were first washed 3X in Dulbecco's PBS with 0.1 g/L $CaCl_2$ and 0.1 g/L $MgCl_2$ (D-PBS), then were labeled for 15 min at room temperature (RT) in 300 μL of labeling solution with 1 nM of CoA-QDs, 10 mM $MgCl_2$, and 0.4 μM ACP-Synthase in DMEM with 10% FBS. The labeled cells were washed 3X in D-PBS and blocked in D-PBS with 1% BSA for 1-2 min. Cells were then simultaneously labeled with stock solution composed of 200 pM custom-conjugated cholera toxin subunit B QDs (peak emission 705 nm) and 1 nM commercial streptavidin-conjugated QDs (peak emission 605 nm) in D-PBS with 1% BSA for 2 min at RT, and blocked with 100 μL of 1 mM biotin for 2 min at RT. The cells were finally washed 3X in D-PBS and imaged in D-PBS with 1% BSA and 25 μM β-mercaptoethanol (Sigma) to minimize QD blinking.

Imaging

The QD imaging was done with an Olympus IX-81 inverted microscope by use of a 100 W Hg arc lamp for excitation, and a QuadView (MAG Biosystem) image splitter and an EMCCD (Andor, DV887-ECS) for simultaneous excitation and detection of 3 colors of QDs and YFP. A 100X objective lens (NA 1.3) was used and the EMCCD pixel size was 16 µm, so the image pixel size was 0.16 µm. We used a combination of a 470/40 nm excitation bandpass filter, a Q495LP dichroic filter, and a HQ510LP emission filter (Chroma Technology) all placed in a filter cube in the microscope. The emission was subsequently split into four separate color channels in the QuadView image splitter by use of dichroics at 585 nm, 630 nm, and 690 nm, and emission filters at HQ535/30m (for YFP), D605/40m (for 605 nm QDs), D655/20m (for 655 nm QDs) and an empty position for 705 nm QDs. Fluorescence time-lapse image series of labeled cells were acquired at 10 ms integration time for 567 image frames with a size of 256x256 pixels at 25 Hz at RT.

4.2.2 Data Analysis

SPT Analysis

We selected a region of the full image series in which to compare SPT and kICS analyses. The region was chosen because of a suitable labeling density and homogenous background fluorescence. The four channels of the image series, each corresponding to a single QD colour, were analyzed independently using the Particle Tracker plug-in for ImageJ [87]. This analysis determines particle positions in each image frame as well as trajectories describing the motion of individual QDs over time. To minimize inaccurate linking of positions into trajectories we used conservative linking criteria: a maximum link delay of 5 image frames and a maximum allowed particle displacement of one pixel per image frame. Because of QD blinking, many short trajectories were produced. Since the real particle trajectories were much longer, we post-processed the generated data with custom-written Mathematica routines. These routines further linked those trajectories that were longer than a cut-off value of between 10 and 20 frames and that coincided within a space of 8 pixels. Fig. 4.4 shows an example image from each colour channel, and a diagram of the SPT trajectories determined.

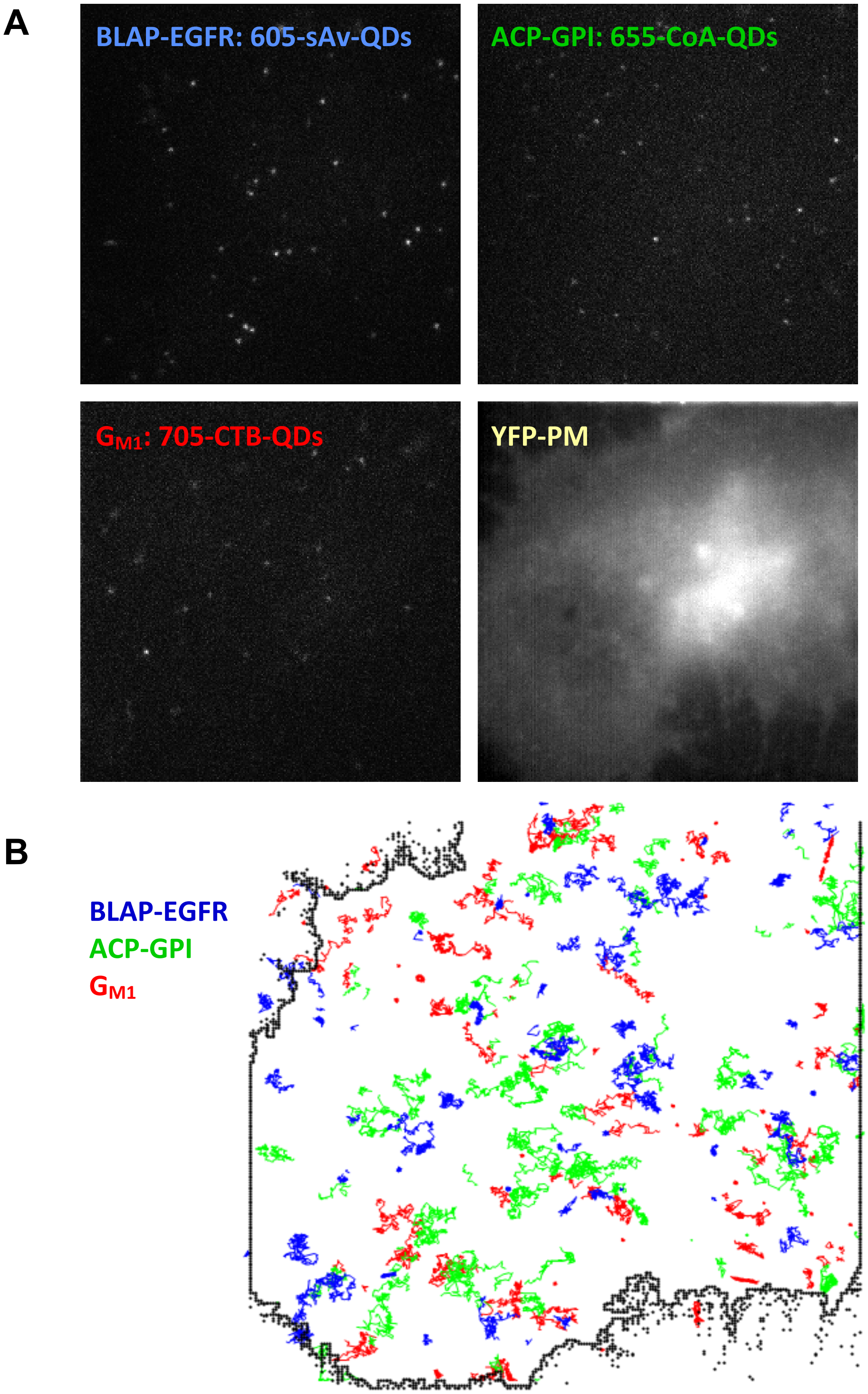

FIGURE 4.4: (A) Example image frames from each colour channel. (*Top left*) 605-sAv-QDs which target biotinylated tyrosine kinase receptor, BLAP-EGFR. (*Top right*) 655-CoA-QDs which target GPI-anchored ACP. (*Lower left*): 705-CTB-QDs which target ganglioside GM1. (*Lower right*) Sum of all frames in the YFP channel.
(B) Overlay of the outline of the cell and the recorded trajectories of the three different kinds of QDs from 567 image frames and a total duration of 22.8 s.

We calculated the mean squared displacements (MSDs) as a function of time for each single trajectory, m, that contained $n > 20$ image frames, and for all possible time intervals, $n\tau$ [89]:

$$MSD_m(n\tau) = \frac{1}{N-n}\sum_{i=1}^{N-n}\left[\left(x_m((i+n)\tau) - x_m(i\tau)\right)^2 + \left(y_m((i+n)\tau) - y_m(i\tau)\right)^2\right] \qquad (4.1)$$

where τ is the frame acquisition time and N is the total number of frames in a trajectory. We determined the average diffusion coefficient in two different ways. First, we calculated the average MSD at each time interval, $n\tau$, as an average of the MSD of all trajectories at that interval:

$$< MSD(n\tau) >= \frac{1}{m}\sum_{m=1}^{M} MSD_m(n\tau) \qquad (4.2)$$

We fit the initial five time points of this single average trajectory to the theoretical expression for free 2D Brownian diffusion plus a constant, c:

$$< MSD(n\tau) >= 4D_{Brownian}\tau + c \qquad (4.3)$$

with fit weights equal to the inverse variance at each point ($1/\sigma^2$), and D_{Brownian} is the diffusion coefficient. We call this the “average trajectory analysis”. The constant c is an offset that relates to the spatial precision by which we can determine the position of a single molecule. We also determined the average diffusion coefficient by separately fitting the MSD of each trajectory that contained $n > 50$ frames to Eq. 4.3 (first five frames fit) to determine a diffusion coefficient for each. We determined the average diffusion coefficient as the mean of these single-trajectory diffusion coefficients. We call this the “separate trajectory analysis”. Fig. 4.5 shows the full set of analyzed trajectory displacements for each QD colour. These plots reveal that there is a high degree of heterogeneity in individual particle diffusive behaviour. The pure blue, green, or red trajectories in the respective figures correspond with the “average trajectory” determined as described above. Although some QDs appear to be immobile in the image series, all observed QDs were included in the SPT analysis.

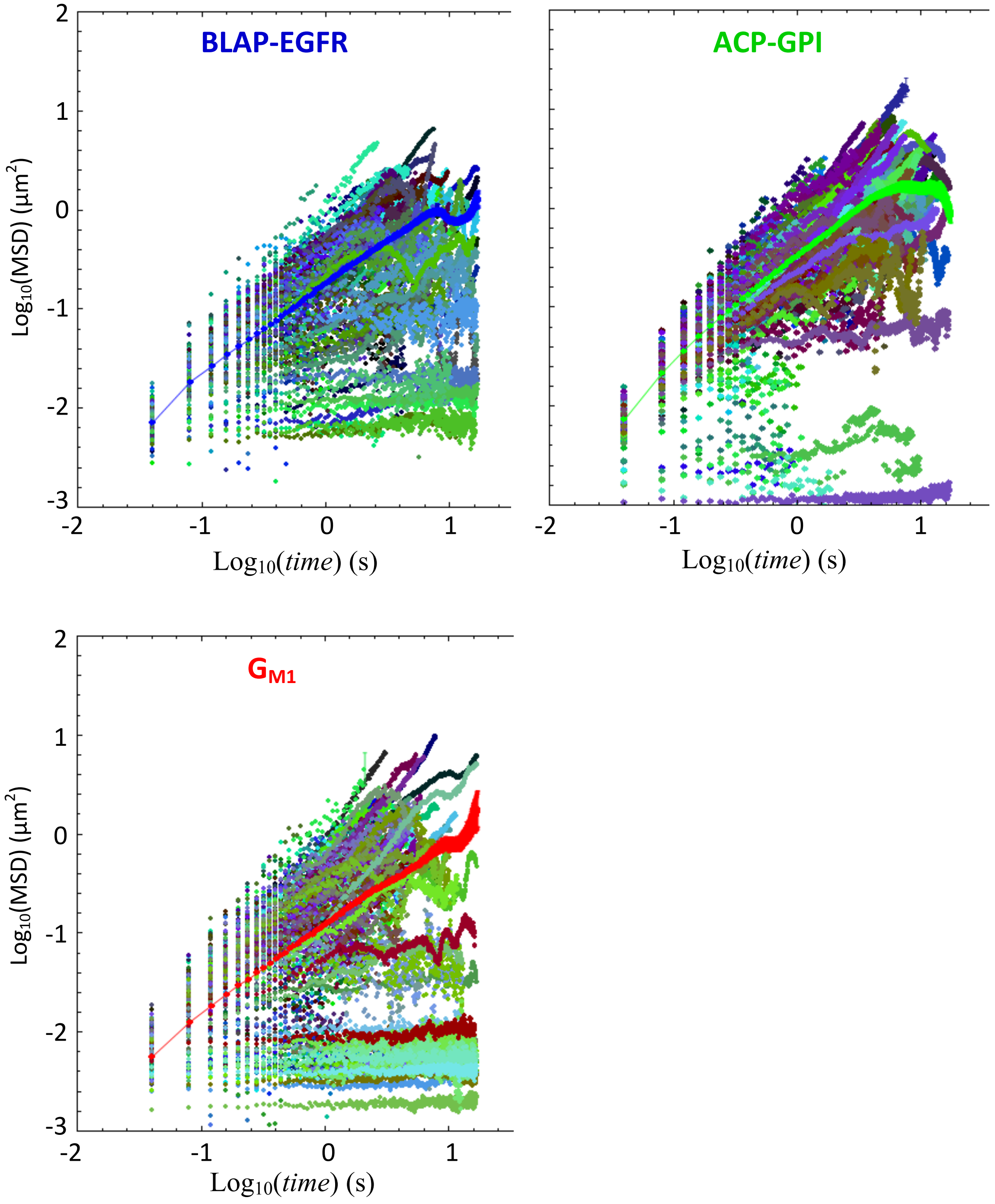

FIGURE 4.5: Log(MSD) vs. log(time) for detected trajectories longer than 10 image frames, shown for each of the three membrane molecules investigated: BLAP-EGFR, ACP-GPI, and G_{M1}. The average trajectory MSD for each of these species is marked by pure blue, green, and red, respectively.

kICS Analysis

An important consideration with kICS is how to handle an image series that has an immobile population of fluorescent molecules. Indeed, this is a ubiquitous concern because even when all fluorophores are mobile, there can be an average background intensity that is not simply white noise, and hence will contribute artificial correlations to the correlation function. Immobile fluorescence intensity will always bias a kICS analysis to lower diffusion measurements. Thus, in any measurement on cells, where autofluorescence or immobile features are frequently present, a method is needed to remove immobile fluorescence. Immobile fluorescence removal has previously been done in correlation spectroscopy experiments with STICS [45] and RICS [68]. Prior to analysis, one subtracts the "mean intensity image" of the entire image series from each image in the series. An efficient way of computing this is to Fourier filter in time each pixel stack in the image separately by setting its DC component to zero [90].

We analyzed the same region of the QD-labeled image series with kICS as was done with SPT. Analyses were done both with and without immobile fluorescence removal by Fourier filtering. In each case we used a $|\mathbf{k}|^2$ cut-off that restricted the normalized kICS correlation decay to less than –2, and used a cut-off of $\tau = 5$ frames (200 ms) to correspond with the 5 frames fit in the SPT diffusion model. Since a single image series was analyzed for each QD colour, we estimated the uncertainty in each kICS measurement by varying the $|\mathbf{k}|^2$ and τ cut-offs to achieve the same theoretical correlation decay, as described in Sec. 3.6. No spatial sampling bias correction was applied to the results, since each image series analyzed contained ~5000 beam areas.

The dynamics plot and the maximum time lag $|\mathbf{k}|^2$ plot from kICS analysis of the BLAP-EGFR QD colour channel, after immobile fluorescence removal, are shown in Fig. 4.6. Plots for the ACP-GPI and GM1 colour channels are not shown, but looked similar.

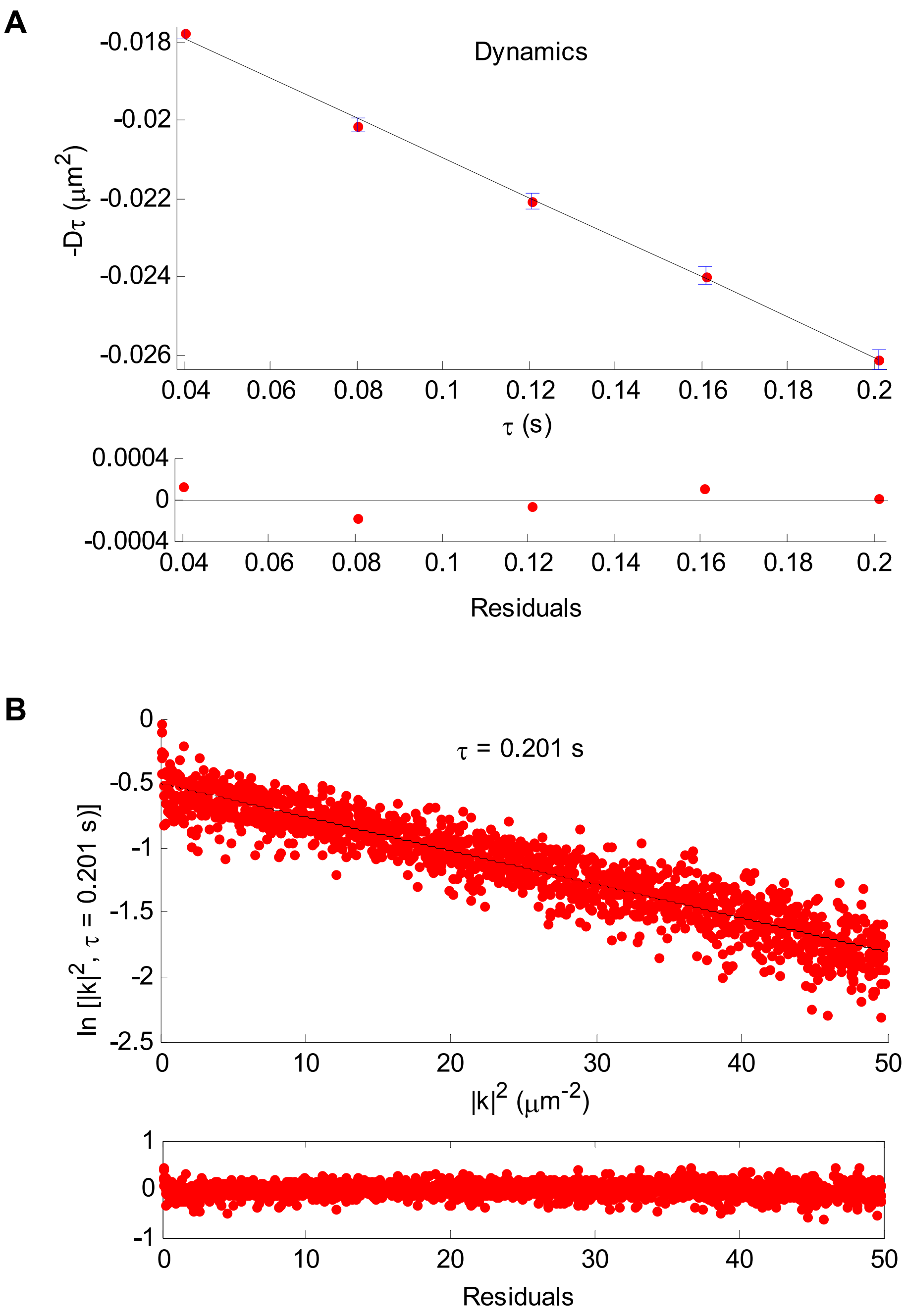

FIGURE 4.6: kICS analyses of QD-labeled membrane molecule diffusion after Fourier immobile removal. Shown are (A) the maximum time lag $|\mathbf{k}|^2$ plot and (B) the dynamics plot for BLAP-EGFR. Plots for the other QD colour channels, corresponding to ACP-GPI and G_{M1}, were similar.

4.2.3 Results

Diffusion measurements from the kICS and SPT analyses described above are shown in Table 4.2. The results obtained with kICS after immobile fluorescence removal are very close to the SPT results in the cases of ACP-GPI and GM1, but are lower than the SPT results for BLAP-EGFR (0.051 $\mu m^2/s$ with kICS vs. 0.07 $\mu m^2/s$ with SPT). The kICS results without immobile fluorescence removal are considerably lower, indicating that background fluorescence and immobile QDs bias the results. This was especially the case for the G_{M1}-ChtoxB-QDs, where the measured diffusion coefficients before and after immobile removal were 0.027 $\mu m^2/s$ and 0.060 $\mu m^2/s$, respectively.

	kICS (no immobile removal)	**kICS (with immobile removal)**	**SPT Average Trajectory**	**SPT Separate Trajectories**
	D ± Error estimate ($\mu m^2/s$)	*D* ± Error estimate ($\mu m^2/s$)	*D* ± SE ($\mu m^2/s$)	*D* ± SD ($\mu m^2/s$)
BLAP-EGFR/ sAv-QD605	0.038 ± 0.001	0.051 ± 0.001	0.074 ± 0.003 (N=60)	0.070 ± 0.048 (N=60)
ACP-GPI/ CoA-QD655	0.090 ± 0.002	0.106 ± 0.002	0.103 ± 0.002 (N=62)	0.100 ± 0.039 (N=62)
G_{M1}/ ChtoxB-QD705	0.027 ± 0.002	0.060 ± 0.001	0.060 ± 0.003 (N=51)	0.057 ± 0.064 (N=51)

TABLE 4.2: Measured diffusion coefficients, using kICS and SPT, for each of the three labeled membrane molecules over the first five time lags. The error estimate for kICS is the standard deviation from kICS analyses run on the same image series using different $|\mathbf{k}|^2$ and τ cut-offs, where τ ranged from 3 to 10 frames.

We can postulate a reason for the large discrepancy between the kICS results with and without immobile removal for G_{M1}. By examining the G_{M1}-QD colour channel, it is apparent that there are a few very bright particles that are completely immobile. Two example images highlighting this, before and after immobile removal, are shown in Fig. 4.7. A major difference between SPT and fluorescence correlation methods is that SPT is independent of particle brightness, provided that a given particle can be tracked at all. In contrast, with kICS the weight given to a particle depends on the square of its fluorescence intensity, since the correlation is a product of two k-space images. If immobile particles are abnormally bright, as appears to be the case for the G_{M1} image series, they will be disproportionately represented in the ensemble-averaged correlation decay in kICS.

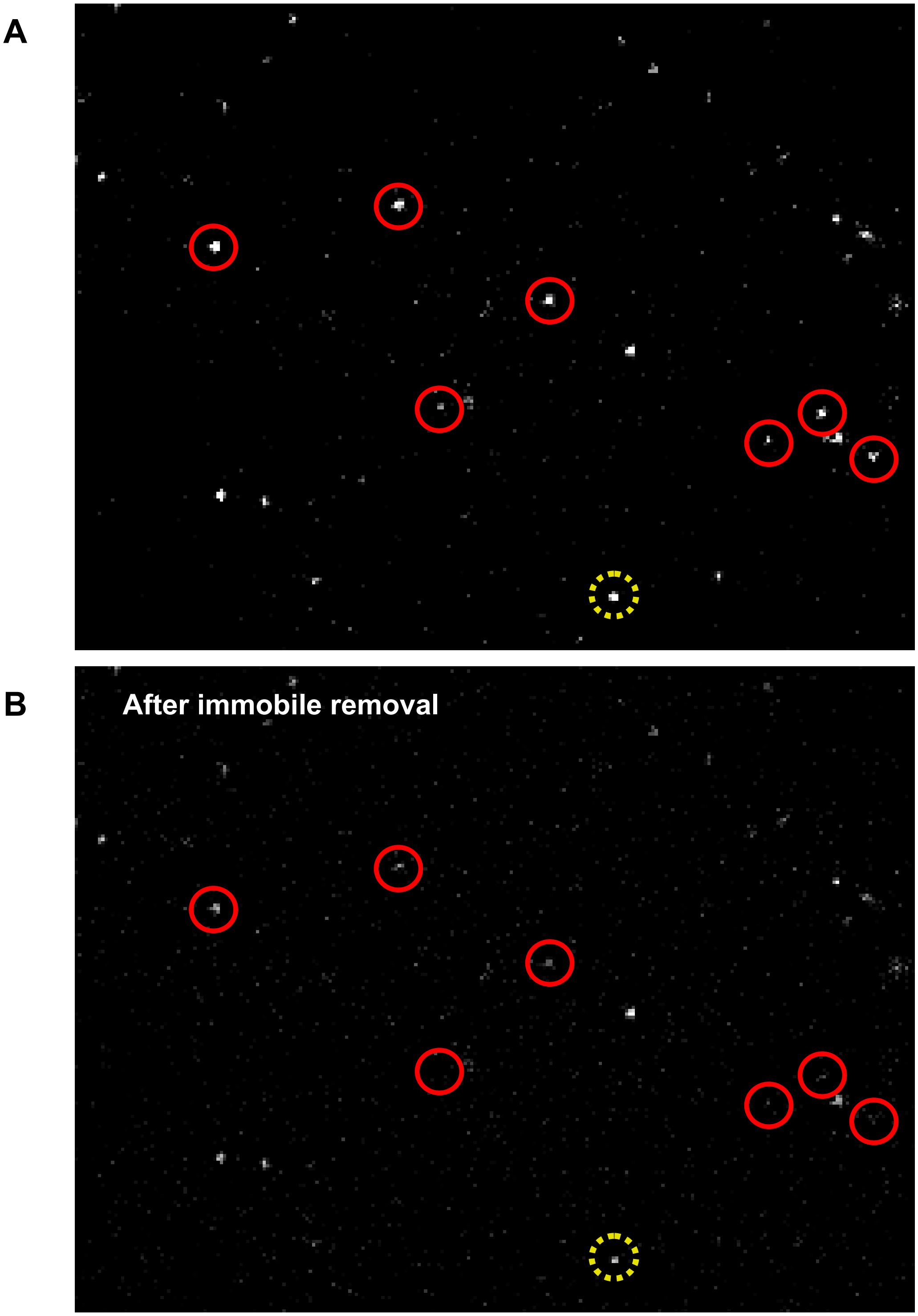

FIGURE 4.7: An image of QD-labeled G_{M1} sphingolipid (A) before immobile fluorescence removal, and (B) after. Circled in red are particles that were completely immobile during the entire image series; the yellow-circled particle was almost completely immobile. Notice that the immobile particles are brighter than most other particles, which explains why they dominate the kICS measurements made without immobile fluorescence removal.

Even when no immobile particles are present, kICS results may differ from SPT results because of differences in particle brightness. For example, some molecules may be doubly labeled, or some QDs could be clustered even before labeling. Larger particles can be expected to diffuse more slowly, and clusters are more apt to be hindered by obstacles in the membrane or on the glass surface. These particles will also be brighter than singly-labeled molecules, and so their lower mobility will be given higher weight in the kICS correlation. With SPT, a cluster of particles with lower mobility will appear as a single bright particle. This could be a factor causing the discrepancy between kICS and SPT in the measured diffusion of BLAP-EGFR, where a few very bright particles appear to have low mobility, but are not immobile.

Overall, diffusion of single particles measured using kICS compares quite well with diffusion measured by more time-consuming SPT analysis. kICS can be applied to image time series of particles that are blinking or bleaching, and subregions of an image can easily be selected for analysis. This makes kICS a useful tool to complement SPT, because kICS analyses can be done quickly, and unlike other fluorescence correlation methods kICS is not biased by fluorophore photophysics.

5. Conclusion

Fluorescence microscopy is a versatile tool for studying the dynamic processes that occur in living cells and cell membranes. In this thesis we have explored a technique, k-space image correlation spectroscopy (kICS), that is particularly well suited to analyze fluorescence microscopy image time series when the fluorophores exhibit photobleaching or blinking emission.

Using computer simulated image series of fluorescent particle diffusion, we examined the effect of spatial sampling on kICS measurements. We found that when small image regions are analyzed with kICS, the reported diffusion coefficient is systematically biased below the true value. This bias results from spectral leakage in the finite Fourier transforms that are computed for the kICS correlation function. We developed two ways in which this bias can be corrected: by multiplying the image data by a suitable window function before applying kICS, or by applying a post-analysis correction to the measured diffusion coefficient. Applying a post-analysis correction has the advantage that no data is discarded, but it is possible that a slight bias remains depending on the particular parameters chosen in the analysis. We confirmed with confocal microscopy image series of diffusing microspheres that bias in kICS depends on the size of the image region analyzed, and that both methods of correction are effective in correcting most of the bias.

Measurement bias is clearly a potential drawback of using kICS. If an experimenter analyzes diffusion in image regions of different sizes, then a direct comparison of the raw measurements will not be valid. It would be highly desirable to find an analytical correction for bias in kICS; however, attempts to find such a correction have so far been unsuccessful. Fortunately, for images of just 40 beam areas (~8 μm^2 on a diffraction-limited sample) the bias is only 20%, and it is less for larger images. Moreover, this is similar to the degree of bias that can occur with other techniques when photobleaching is not properly accounted for [59], and the bias can be easily corrected as described above.

We also examined the accuracy and precision of kICS over a wide range of both spatial and temporal sampling in simulated image series. We found that kICS measurements were more precise than TICS under all conditions examined. In addition, kICS can measure diffusion that is ten time faster than TICS at the same imaging frame rate. This means that one need not be as concerned with selecting the optimal frame rate when applying kICS, whereas TICS could return erroneous results if the frame rate is too low. Although there are techniques that can measure faster diffusion than kICS, such as FCS, FICS, and RICS, these techniques also have drawbacks. FCS and FICS require specialized equipment, and provide information either only at a single point (FCS) or only averaged over an entire field of view (FICS). RICS can only be applied to images acquired with a confocal laser scanning microscope. In contrast, kICS can be used with image series acquired on wide-field, confocal, and TIRF microscopes, kICS can analyze image subregions, and kICS is not affected by fluorophore photobleaching or blinking.

We demonstrated that when normalized by the zero-time-lags correlation, kICS can accurately measure diffusion even when the initial distribution of particles is highly nonuniform, which would be the case after localized photouncaging or photoconversion of biological effector molecules. We also explained how the transition to noise is more clearly visible in normalized kICS $|\mathbf{k}|^2$ plots, and how this helps to compute reasonable cut-offs to use as kICS analysis parameters when the diffusion speed can be estimated. Indeed, the ability to tradeoff between the $|\mathbf{k}|^2$ and τ cutoffs is the basis for a method we proposed to estimate the uncertainty in a single kICS measurement, which is to perform multiple analyses of the same data using different cut-offs. This uncertainty estimate includes a contribution from underlying variability in the biological sample as well as a contribution from the subjective choice of optimal $|\mathbf{k}|^2$ and τ fitting parameters. When it is not possible or convenient to perform multiple measurements, this uncertainty estimate is better than one determined from a single kICS analysis of the data.

In this thesis we have presented a number of findings that will benefit anyone using kICS to measure diffusion of fluorescently labeled macromolecules in living cells. Although outside the scope of this thesis, the methods we developed to examine the accuracy of kICS diffusion measurements could be extended in a straightforward way to kICS measurements of flow.

6. References

1. Wallin, E., and G. von Heijne. 1998. Genome-wide analysis of integral membrane proteins from eubacterial, archaean, and eukaryotic organisms. Protein Sci. 7:1029-1038.

2. Fagerberg, L., K. Jonasson, G. von Heijne, M. Uhlen, and L. Berglund. 2010. Prediction of the human membrane proteome. Proteomics 10:1141-1149.

3. Singer, S. J., and G. L. Nicolson. 1972. Fluid mosaic model of structure of cell membranes. Science 175:720-&.

4. Simons, K., and E. Ikonen. 1997. Functional rafts in cell membranes. Nature 387:569-572.

5. Brown, D. A., and E. London. 2000. Structure and function of sphingolipid- and cholesterol-rich membrane rafts. Journal of Biological Chemistry 275:17221-17224.

6. Jacobson, K., O. G. Mouritsen, and R. G. W. Anderson. 2007. Lipid rafts: at a crossroad between cell biology and physics. Nature Cell Biology 9:7-14.

7. Engelman, D. M. 2005. Membranes are more mosaic than fluid. Nature 438:578-580.

8. Lippincott-Schwartz, J., E. Snapp, and A. Kenworthy. 2001. Studying protein dynamics in living cells. Nature Reviews Molecular Cell Biology 2:444-456.

9. Wenger, J., F. Conchonaud, J. Dintinger, L. Wawrezinieck, T. W. Ebbesen, H. Rigneault, D. Marguet, and P. F. Lenne. 2007. Diffusion analysis within single nanometric apertures reveals the ultrafine cell membrane organization. Biophysical Journal 92:913-919.

10. Eggeling, C., C. Ringemann, R. Medda, G. Schwarzmann, K. Sandhoff, S. Polyakova, V. N. Belov, B. Hein, C. von Middendorff, A. Schonle, and S. W. Hell. 2009. Direct observation of the nanoscale dynamics of membrane lipids in a living cell. Nature 457:1159-U1121.

11. Douglass, A. D., and R. D. Vale. 2005. Single-molecule microscopy reveals plasma membrane microdomains created by protein-protein networks that exclude or trap signaling molecules in T cells. Cell 121:937-950.

12. Harada, Y., K. Sakurada, T. Aoki, D. D. Thomas, and T. Yanagida. 1990. Mechanochemical coupling in actomyosin energy transduction studied by in vitro movement assay. Journal of Molecular Biology 216:49-68.

13. Vogelsang, J., R. Kasper, C. Steinhauer, B. Person, M. Heilemann, M. Sauer, and P. Tinnefeld. 2008. A reducing and oxidizing system minimizes photobleaching

and blinking of fluorescent dyes. Angewandte Chemie-International Edition 47:5465-5469.

14. Herschel, J. F. W. 1845. On a case of superficial colour presented by a homogeneous liquid internally colourless. Phil Trans Roy Soc (London) 135:143-145.

15. Giepmans, B. N. G., S. R. Adams, M. H. Ellisman, and R. Y. Tsien. 2006. Review - The fluorescent toolbox for assessing protein location and function. Science 312:217-224.

16. Ormo, M., A. B. Cubitt, K. Kallio, L. A. Gross, R. Y. Tsien, and S. J. Remington. 1996. Crystal structure of the Aequorea victoria green fluorescent protein. Science 273:1392-1395.

17. Heim, R., A. B. Cubitt, and R. Y. Tsien. 1995. Improved green fluorescence. Nature 373:663-664.

18. Heim, R., D. C. Prasher, and R. Y. Tsien. 1994. Wavelength mutations and posttranslational autoxidation of green fluorescent protein. Proceedings of the National Academy of Sciences of the United States of America 91:12501-12504.

19. Campbell, R. E., O. Tour, A. E. Palmer, P. A. Steinbach, G. S. Baird, D. A. Zacharias, and R. Y. Tsien. 2002. A monomeric red fluorescent protein. Proceedings of the National Academy of Sciences of the United States of America 99:7877-7882.

20. Lippincott-Schwartz, J., and G. H. Patterson. 2003. Development and use of fluorescent protein markers in living cells. Science 300:87-91.

21. Yu, C. X., J. Hale, K. Ritchie, N. K. Prasad, and J. Irudayaraj. 2009. Receptor overexpression or inhibition alters cell surface dynamics of EGF-EGFR interaction: New insights from real-time single molecule analysis. Biochemical and Biophysical Research Communications 378:376-382.

22. Lippincott-Schwartz, J., and G. H. Patterson. 2009. Photoactivatable fluorescent proteins for diffraction-limited and super-resolution imaging. Trends in Cell Biology 19:555-565.

23. Huang, B., W. Q. Wang, M. Bates, and X. W. Zhuang. 2008. Three-dimensional super-resolution imaging by stochastic optical reconstruction microscopy. Science 319:810-813.

24. Michalet, X., F. F. Pinaud, L. A. Bentolila, J. M. Tsay, S. Doose, J. J. Li, G. Sundaresan, A. M. Wu, S. S. Gambhir, and S. Weiss. 2005. Quantum dots for live cells, in vivo imaging, and diagnostics. Science 307:538-544.

25. Chan, W. C. W., and S. M. Nie. 1998. Quantum dot bioconjugates for ultrasensitive nonisotopic detection. Science 281:2016-2018.

26. Bachir, A. I., N. Durisic, B. Hebert, P. Grutter, and P. W. Wiseman. 2006. Characterization of blinking dynamics in quantum dot ensembles using image correlation spectroscopy. Journal of Applied Physics 99.

27. Wang, X. Y., X. F. Ren, K. Kahen, M. A. Hahn, M. Rajeswaran, S. Maccagnano-Zacher, J. Silcox, G. E. Cragg, A. L. Efros, and T. D. Krauss. 2009. Non-blinking semiconductor nanocrystals. Nature 459:686-689.

28. Resch-Genger, U., M. Grabolle, S. Cavaliere-Jaricot, R. Nitschke, and T. Nann. 2008. Quantum dots versus organic dyes as fluorescent labels. Nature Methods 5:763-775.

29. Lagerholm, B. C., G. E. Weinreb, K. Jacobson, and N. L. Thompson. 2005. Detecting microdomains in intact cell membranes. Annual Review of Physical Chemistry 56:309-336.

30. Swedlow, J. R., and M. Platani. 2002. Live cell imaging using wide-field microscopy and deconvolution. Cell Structure and Function 27:335-341.

31. Inoué, S. 2006. Foundations of Confocal Scanned Imaging in Light Microscopy. Springer, New York.

32. Hell, S. W. 2007. Far-field optical nanoscopy. Science 316:1153-1158.

33. Willig, K. I., B. Harke, R. Medda, and S. W. Hell. 2007. STED microscopy with continuous wave beams. Nature Methods 4:915-918.

34. Betzig, E., G. H. Patterson, R. Sougrat, O. W. Lindwasser, S. Olenych, J. S. Bonifacino, M. W. Davidson, J. Lippincott-Schwartz, and H. F. Hess. 2006. Imaging intracellular fluorescent proteins at nanometer resolution. Science 313:1642-1645.

35. Rust, M. J., M. Bates, and X. W. Zhuang. 2006. Sub-diffraction-limit imaging by stochastic optical reconstruction microscopy (STORM). Nature Methods 3:793-795.

36. Manley, S., J. M. Gillette, G. H. Patterson, H. Shroff, H. F. Hess, E. Betzig, and J. Lippincott-Schwartz. 2008. High-density mapping of single-molecule trajectories with photoactivated localization microscopy. Nature Methods 5:155-157.

37. Brown, A. 2003. Axonal transport of membranous. and nonmembranous cargoes: a unified perspective. Journal of Cell Biology 160:817-821.

38. Elson, E. L., and D. Magde. 1974. Fluorescence correlation spectroscopy 1. Conceptual basis and theory. Biopolymers 13:1-27.

39. Magde, D., E. L. Elson, and W. W. Webb. 1974. Fluorescence correlation spectroscopy 2. Experimental realization. Biopolymers 13:29-61.

40. Dertinger, T., V. Pacheco, I. von der Hocht, R. Hartmann, I. Gregor, and J. Enderlein. 2007. Two-focus fluorescence correlation spectroscopy: A new tool for accurate and absolute diffusion measurements. Chemphyschem 8:433-443.

41. Humpolickova, J., E. Gielen, A. Benda, V. Fagulova, J. Vercammen, M. Vandeven, M. Hof, M. Ameloot, and Y. Engelborghs. 2006. Probing diffusion laws within cellular membranes by Z-scan fluorescence correlation spectroscopy. Biophysical Journal 91:L23-L25.

42. Ruan, Q. Q., M. A. Cheng, M. Levi, E. Gratton, and W. W. Mantulin. 2004. Spatial-temporal studies of membrane dynamics: Scanning fluorescence correlation spectroscopy (SFCS). Biophysical Journal 87:1260-1267.

43. Petersen, N. O., P. L. Hoddelius, P. W. Wiseman, O. Seger, and K. E. Magnusson. 1993. Quantitation of membrane receptor distributions by image correlation spectroscopy - concept and application. Biophysical Journal 65:1135-1146.

44. Wiseman, P. W., J. A. Squier, M. H. Ellisman, and K. R. Wilson. 2000. Two-photon image correlation spectroscopy and image cross-correlation spectroscopy. Journal of Microscopy-Oxford 200:14-25.

45. Hebert, B., S. Costantino, and P. W. Wiseman. 2005. Spatiotemporal image correlation Spectroscopy (STICS) theory, verification, and application to protein velocity mapping in living CHO cells. Biophysical Journal 88:3601-3614.

46. Kolin, D. L., D. Ronis, and P. W. Wiseman. 2006. k-Space image correlation spectroscopy: A method for accurate transport measurements independent of fluorophore photophysics. Biophysical Journal 91:3061-3075.

47. Garcia-Saez, A. J., and P. Schwille. 2010. Surface analysis of membrane dynamics. Biochimica Et Biophysica Acta-Biomembranes 1798:766-776.

48. Kusumi, A., Y. Sako, and M. Yamamoto. 1993. Confined lateral diffusion of membrane receptors as studied by single-particle tracking (nanovid microscopy) - effects of calcium-induced differentiation in clutured epithelial cells. Biophysical Journal 65:2021-2040.

49. Lidke, D. S., K. A. Lidke, B. Rieger, T. M. Jovin, and D. J. Arndt-Jovin. 2005. Reaching out for signals: filopodia sense EGF and respond by directed retrograde transport of activated receptors. Journal of Cell Biology 170:619-626.

50. Crane, J. M., and A. S. Verkman. 2008. Long-range nonanomalous diffusion of quantum dot-labeled aquaporin-1 water channels in the cell plasma membrane. Biophysical Journal 94:702-713.

51. Bonneau, S., M. Dahan, and L. D. Cohen. 2005. Single quantum dot tracking based on perceptual grouping using minimal paths in a spatiotemporal volume. Ieee Transactions on Image Processing 14:1384-1395.

52. Serge, A., N. Bertaux, H. Rigneault, and D. Marguet. 2008. Dynamic multiple-target tracing to probe spatiotemporal cartography of cell membranes. Nature Methods 5:687-694.

53. Jaqaman, K., D. Loerke, M. Mettlen, H. Kuwata, S. Grinstein, S. L. Schmid, and G. Danuser. 2008. Robust single-particle tracking in live-cell time-lapse sequences. Nature Methods 5:695-702.

54. Ritchie, K., X. Y. Shan, J. Kondo, K. Iwasawa, T. Fujiwara, and A. Kusumi. 2005. Detection of non-Brownian diffusion in the cell membrane in single molecule tracking. Biophysical Journal 88:2266-2277.

55. Dietrich, C., B. Yang, T. Fujiwara, A. Kusumi, and K. Jacobson. 2002. Relationship of lipid rafts to transient confinement zones detected by single particle tracking. Biophysical Journal 82:274-284.

56. Wiseman, P. W., and N. O. Petersen. 1999. Image correlation spectroscopy. II. Optimization for ultrasensitive detection of preexisting platelet-derived growth factor-beta receptor oligomers on intact cells. Biophysical Journal 76:963-977.

57. Bates, I. R., B. Hebert, Y. S. Luo, J. Liao, A. I. Bachir, D. L. Kolin, P. W. Wiseman, and J. W. Hanrahan. 2006. Membrane lateral diffusion and capture of CFTR within transient confinement zones. Biophysical Journal 91:1046-1058.

58. Wiseman, P. W., C. M. Brown, D. J. Webb, B. Hebert, N. L. Johnson, J. A. Squier, M. H. Ellisman, and A. F. Horwitz. 2004. Spatial mapping of integrin interactions and dynamics during cell migration by Image Correlation Microscopy. Journal of Cell Science 117:5521-5534.

59. Kolin, D. L., S. Costantino, and P. W. Wiseman. 2006. Sampling effects, noise, and photobleaching in temporal image correlation spectroscopy. Biophysical Journal 90:628-639.

60. Dittrich, P. S., and P. Schwille. 2001. Photobleaching and stabilization of fluorophores used for single-molecule analysis with one- and two-photon excitation. Applied Physics B-Lasers and Optics 73:829-837.

61. Mertz, J. 1998. Molecular photodynamics involved in multi-photon excitation fluorescence microscopy. European Physical Journal D 3:53-66.

62. Grassman, T. J., M. K. Knowles, and A. H. Marcus. 2000. Structure and dynamics of fluorescently labeled complex fluids by Fourier imaging correlation spectroscopy. Physical Review E 62:8245-8257.

63. Margineantu, D., R. A. Capaldi, and A. H. Marcus. 2000. Dynamics of the mitochondrial reticulum in live cells using Fourier imaging correlation spectroscopy and digital video microscopy. Biophysical Journal 79:1833-1849.

64. Fink, M. C., K. V. Adair, M. G. Guenza, and A. H. Marcus. 2006. Translational diffusion of fluorescent proteins by molecular Fourier imaging correlation spectroscopy. Biophysical Journal 91:3482-3498.

65. Zhou, M., and Y. L. Wang. 2008. Distinct pathways for the early recruitment of myosin II and actin to the cytokinetic furrow. Mol. Biol. Cell 19:318-326.

66. Bove, J., B. Vaillancourt, J. Kroeger, P. K. Hepler, P. W. Wiseman, and A. Geitmann. 2008. Magnitude and direction of vesicle dynamics in growing pollen tubes using spatiotemporal image correlation spectroscopy and fluorescence recovery after photobleaching. Plant Physiol. 147:1646-1658.

67. Tanner, K., D. R. Ferris, L. Lanzano, B. Mandefro, W. W. Mantulin, D. M. Gardiner, E. L. Rugg, and E. Gratton. 2009. Coherent Movement of Cell Layers during Wound Healing by Image Correlation Spectroscopy. Biophysical Journal 97:2098-2106.

68. Digman, M. A., C. M. Brown, P. Sengupta, P. W. Wiseman, A. R. Horwitz, and E. Gratton. 2005. Measuring fast dynamics in solutions and cells with a laser scanning microscope. Biophysical Journal 89:1317-1327.

69. Digman, M. A., and E. Gratton. 2009. Imaging Barriers to Diffusion by Pair Correlation Functions. Biophysical Journal 97:665-673.

70. Sankaran, J., M. Manna, L. Guo, R. Kraut, and T. Wohland. 2009. Diffusion, Transport, and Cell Membrane Organization Investigated by Imaging Fluorescence Cross-Correlation Spectroscopy. Biophysical Journal 97:2630-2639.

71. Kannan, B., L. Guo, T. Sudhaharan, S. Ahmed, I. Maruyama, and T. Wohland. 2007. Spatially resolved total internal reflection fluorescence correlation microscopy using an electron multiplying charge-coupled device camera. Analytical Chemistry 79:4463-4470.

72. Dickson, R. M., A. B. Cubitt, R. Y. Tsien, and W. E. Moerner. 1997. On/off blinking and switching behaviour of single molecules of green fluorescent protein. Nature 388:355-358.

73. Sinnecker, D., P. Voigt, N. Hellwig, and M. Schaefer. 2005. Reversible photobleaching of enhanced green fluorescent proteins. Biochemistry 44:7085-7094.

74. Petrek, Z., and P. Schwille. 2008. Photobleaching in two-photon scanning fluorescence correlation spectroscopy. Chemphyschem 9:147-158.

75. Doose, S., J. M. Tsay, F. Pinaud, and S. Weiss. 2005. Comparison of photophysical and colloidal properties of biocompatible semiconductor nanocrystals using fluorescence correlation spectroscopy. Analytical Chemistry 77:2235-2242.

76. Berne, B. J., and R. Pecora. 2000. Dynamic Light Scattering. Dover Publications, New York.

77. Durisic, N., A. I. Bachir, D. L. Kolin, B. Hebert, B. C. Lagerholm, P. Grutter, and P. W. Wiseman. 2007. Detection and correction of blinking bias in image

correlation transport measurements of quantum dot tagged macromolecules. Biophysical Journal 93:1338-1346.

78. Koppel, D. E. 1974. Statistical Accuracy in Fluorescence Correlation Spectroscopy. Physical Review A 10:1938-1945.

79. Saffarian, S., and E. L. Elson. 2003. Statistical analysis of fluorescence correlation spectroscopy: The standard deviation and bias. Biophysical Journal 84:2030-2042.

80. Matsuda, T., A. Miyawaki, and T. Nagai. 2008. Direct measurement of protein dynamics inside cells using a rationally designed photoconvertible protein. Nature Methods 5:339-345.

81. Pellois, J. P., M. E. Hahn, and T. W. Muir. 2004. Simultaneous triggering of protein activity, and fluorescence. Journal of the American Chemical Society 126:7170-7171.

82. Lee, H. M., M. A. Priestman, and D. S. Lawrence. 2010. Light-Mediated Spatial Control via Photolabile Fluorescently Quenched Peptide Cassettes. Journal of the American Chemical Society 132:1446-+.

83. Press, W. H., B. P. Flannery, S. A. Teukolsky, and W. T. Vetterling. 1992. Numerical Recipes in C. Cambridge University Press, Cambridge.

84. Garcia-Saez, A. J., and P. Schwille. 2008. Fluorescence correlation spectroscopy for the study of membrane dynamics and protein/lipid interactions. Methods 46:116-122.

85. Specht, A., F. Bolze, Z. Omran, J. F. Nicoud, and M. Goeldner. 2009. Photochemical tools to study dynamic biological processes. Hfsp Journal 3:255-264.

86. Gustafsson, M. G. L. 2000. Surpassing the lateral resolution limit by a factor of two using structured illumination microscopy. Journal of Microscopy-Oxford 198:82-87.

87. Sbalzarini, I. F., and P. Koumoutsakos. 2005. Feature point tracking and trajectory analysis for video imaging in cell biology. J. Struct. Biol. 151:182-195.

88. Howarth, M., and A. Y. Ting. 2008. Imaging proteins in live mammalian cells with biotin ligase and monovalent streptavidin. Nature Protocols 3:534-545.

89. Bannai, H., S. Levi, C. Schweizer, M. Dahan, and A. Triller. 2006. Imaging the lateral diffusion of membrane molecules with quantum dots. Nature Protocols 1:2628-2634.

90. Kolin, D. L., and P. W. Wiseman. 2007. Advances in image correlation spectroscopy: Measuring number densities, aggregation states, and dynamics of fluorescently labeled macromolecules in cells. Cell Biochemistry and Biophysics 49:141-164.